An In-Depth Examination of a Thermodynamic Framework for the Phase-Field Crystal Model

by

Victor W. L. Chan

A dissertation submitted in partial fulfillment
of the requirements for the degree of
Doctor of Philosophy
(Materials Science and Engineering)
in The University of Michigan
2015

Doctoral Committee:

Associate Professor Katsuyo S. Thornton, Chair
Professor Ken R. Elder, Oakland University
Associate Professor Vikram Gavini
Assistant Professor Emmanouil Kioupakis

“Not only so, but we also glory in our sufferings, because we know that suffering
produces perseverance; perseverance, character; and character, hope.”
(Romans 5:3-4)

ACKNOWLEDGEMENTS

I am grateful to my advisor, Professor Katsuyo Thornton, for providing me with the opportunity to pursue my interest in the field of computational materials science. I am fortunate that she took a chance on me, a young man who had no computational background and little appreciation for mathematical rigor, and provided me with the guidance, support, and discipline to grow as a scientist. I am indebted to her for sacrificing nights and weekends in order to bring this dissertation to completion.

I also thank Professor Ken Elder, Professor Vikram Gavini, and Professor Emmanouil Kioupakis, for their comments and suggestions on the dissertation.

The past six and a half years was made considerably more enjoyable with the camaraderie from members of the Thornton research group. I am especially grateful to Nirand and HCY for mentoring me through this time and Chal for sharing this journey with me. I am also indebted to Jason and David for their invaluable suggestions and comments on the work presented in this dissertation.

I would also like to express my gratitude to Elizabeth Hildinger for her friendship and help with editing my manuscripts and dissertation; I could not ask for a more patient and caring writing mentor.

I am grateful to the Courts, Eatons, Gadways, Raymonds, and Richardsons for making Ann Arbor home. I am also indebted to my parents for their love and encouragement to pursue my dreams. Finally, I thank my wife, Wonhyung, for cheering me on every step of the way.

TABLE OF CONTENTS

CHAPTER

LIST OF FIGURES

Figure

LIST OF TABLES

<u>**Table**</u>

LIST OF APPENDICES

Appendix

ABSTRACT

An In-Depth Examination of a Thermodynamic Framework
for the Phase-Field Crystal Model

by

Victor W. L. Chan

Chair: Katsuyo Thornton

In this dissertation, we examine the phase-field crystal (PFC) model, which is a simulation method for modeling atomistic phenomena on diffusive time scales. Once parameterized to equilibrium properties, the PFC model can be employed as a quantitative tool for predicting non-equilibrium atomistic materials phenomena on time scales that are often inaccessible to atomistic simulations. We develop thermodynamic relationships that are used to derive procedures for calculating equilibrium material properties from the PFC model. These relationships are also applied to gain a rigorous understanding of PFC simulation results.

The first set of relationships links the PFC free energy to thermodynamic state variables and are based on the thermodynamic formalism for crystalline systems introduced by Larché and Cahn [Larché and Cahn, Acta Metallurgica, 21 1051 (1973)]. These relationships are employed to examine the thermodynamic processes associated with varying the input parameters of the PFC model. Additionally, the equilibrium conditions between bulk crystalline solid and liquid phases are imposed on the relationships to obtain a procedure for determining solid-liquid phase coexistence. The resulting procedure is found to be in agreement with the common-tangent construction commonly used in the PFC community. We apply the procedure to an eighth-order-fit (EOF) PFC model that has been parameterized to body-centered-cubic (*bcc*) Fe [Jaatinen et al., Physical Review E 80, 031602 (2009)] and demonstrate that the model does not predict stable *bcc* structures with positive vacancy densities.

The second set of relationships is built on the recent work of Pisutha-Arnond et al. [Pisutha-Arnond et al., Physical Review B, 87 014103 (2013)], and is applied to develop a thermodynamically consistent procedure for determining elastic constants from PFC models based on the classical density-functional theory (cDFT) of freezing [Elder et al., Physical Review B, 75 064107 (2007)]. To implement these procedures, we present two alternative deformation methods, one in real space and the other in Fourier space, that are computationally more accurate and efficient than the method conventionally used in the PFC community. The procedure for determining elastic constants is implemented with the Fourier space deformation method to calculate bulk mechanical properties from the EOF-PFC model.

Finally, we present a structural PFC model [Greenwood et al., Physical Review Letters 105, 045702 (2010)] that yields a stable diamond-cubic (*dc*) structure. The stabilization of a *dc* structure is accomplished by constructing a two-body direct correlation function (DCF) approximated by a combination of two Gaussian functions in Fourier space. A phase diagram that contains a *dc*-liquid phase coexistence region was constructed for the model. We examine the energies of the (100), (110), and (111) solid-liquid interfaces. The dependence of interfacial energy on a temperature parameter, which controls the heights of the peaks in the two-body DCF, is described by a Gaussian function. Furthermore, the dependence of interfacial energy on peak widths of the two-body DCF, which controls the excess energy associated with interfaces, defects, and strain, is described by an inverse power law.

CHAPTER I

Introduction

The performance of a material is governed by its underlying atomic- and microscale structures, which contain vacancies, dislocations, impurities, and grain and phase boundaries [1]. These structural elements form and evolve under thermal and mechanical processing, and give rise to different material properties. Thermal processes such as cooling and annealing cause changes in the phase and grain boundaries that affect the mechanical behavior [1, 2]. For example, in an Al-Zn alloy, a solid-state phase transformation from a face-centered-cubic (fcc) to a two-phase mixture of fcc and hexagonal-close-packed (hcp) phases occurs when the alloy is cooled from 300°C to below 275°C. The resulting structure has significantly higher tensile and yield strength than the structure of the initial phase [3]. On the other hand, annealing of a polycrystalline metal causes grain growth and typically lowers the yield strength in those cases when the grains are sufficiently large. Mechanical processes such as cold deformation also alter the underlying structure and affect material properties. For example, cold rolling of a metal increases dislocation density, leading to higher yield strengths [2, 4]. Furthermore, in thin-film growth, lattice mismatch at the substrate and thin-film interface lead to morphological instabilities. These instabilities can be exploited to form periodic structures on a thin film, such as quantum dots, which have optoelectronic applications [5, 6].

As seen in the examples identified above, materials processing is intimately related to the details of the underlying structure and ultimately dictates the properties of the material. Therefore, a better understanding of how processing parameters affect the formation and evolution of defects, grain structures, and phase boundaries is important for designing materials with tailored properties and improved performance.

One of the challenges in understanding these relationships is that they stem from phenomena occurring over multiple length and time scales. This can be illustrated in a typical solidification example. At very small time and length scales, atomic interactions in the liquid phase cause crystallites to nucleate. Once these crystallites have formed, they grow and impinge on one another to form grain boundaries and establish a microstructure over a much longer time scale. Thus, to understand how processing parameters affect the structure of a material, one needs a formalism that captures both atomic and micron length-scales while simultaneously handling the large gap between the time scale of atomic vibrations and the experimentally observable diffusive time scales.

Because materials phenomena often involve multiple time and length scales, both continuum and atomistic models are used to study microstructure formation and phase selection [7]. One common continuum model is the phase-field (PF) model, which has been successfully applied to simulate a wide range of materials phenomena including solidification [8, 9, 10, 11], solid-state phase transformations [12, 13, 14], and coarsening and grain growth [15, 16, 17] (see also Refs. [18, 19] for comprehensive reviews). The PF model uses one or more order parameters to distinguish various phases or grains within a microstructure. A PF order parameter can be considered as a coarse-grained field that averages out individual atomic-scale details but retains the microstructural features. The resulting model describes the evolution of the microstructure over the diffusive time-scale. However, since the formulation of the PF model does not account for atomic-scale details, the description of phenomena that arise from crystallographic symmetries that are inherent in crystalline solids involves auxiliary field variables, which require additional parameterization. At the other end of the spectrum, a common atomistic model is molecular dynamics (MD). MD tracks the positions of individual atoms, which are updated in accordance with Newton's laws of motion and forces that are calculated from atomic potentials [20, 21, 22]. It captures the atomistic details of the system, as well as thermodynamics and kinetics when the results are ensemble averaged. However, MD simulations are limited by the time scale of atomic vibrations, which are orders of magnitude smaller than those associated with many materials phenomena. Recently, the phase-field crystal (PFC) model [23, 24] has been introduced to address these limitations. The PFC model shares a similarity with the PF model because the governing equation is based on dissipative dynamics for order-parameter evolution, but it has some of the advantages of MD in that atomic resolution is retained.

The capability of the PFC model to describe atomistic phenomena at diffusive time scales has enabled researchers to investigate a wide variety of materials phenomena such as defect dynamics [25, 26, 27, 28, 29], crystal nucleation [30, 31] and growth [32, 33, 34, 35], heteroepitaxy to form thin films [36, 37, 38, 39, 40, 41, 42, 43], and glass formation [44]. Furthermore, links between PFC model parameters to measurable quantities in experiments and atomistic simulations were made by Elder et al. [45], who showed that the PFC model can be derived from the classical density-functional theory (cDFT) of freezing [46, 47], which is based on statistical mechanics [48, 49]. In this work, (i) the PFC free energy was identified as the Helmholtz free energy, (ii) the PFC order-parameter was found to be an atomic-probability density, obtained by taking an ensemble average of the microscopic particle density [48], and (iii) the bulk modulus and lattice spacing of a crystal were associated with the height and position, respectively, of the first peak of the two-body direct correlation function (DCF), which could be obtained from experiments or atomistic simulations. Additionally, because of the link established between cDFT and PFC, extensions that exists for cDFT can be readily adapted to the PFC model, including PFC formulations for multi-component systems [45, 50], anisotropic lattices [51], and liquid-crystalline systems [52].

Although the PFC model has been employed to study a wide variety of materials phenomena and its model parameters have been linked to measurable quantities, the procedures for calculating equilibrium material properties from the PFC model are not straightforward [53] because the thermodynamic interpretation of the PFC free energy has not been fully developed. As a result, the PFC model cannot be rigorously parameterized to produce equilibrium properties that match those measured experimentally or calculated from atomistic simulations, preventing the use of the PFC model as a predictive tool for non-equilibrium material processes.

We present thermodynamic relationships between the PFC free energy and thermodynamic state variables to rigorously and quantitatively interpret results calculated from PFC simulations. We also develop thermodynamically consistent procedures for calculating solid-liquid phase coexistence and elastic constants. These procedures are employed to investigate the validity of a PFC parameterization for body-centered-cubic (*bcc*) Fe [54]. Finally, we investigate the phase coexistence and solid-liquid interfacial energy of a PFC model with a stable diamond-cubic, *dc*, structure, which is based on the structural PFC (XPFC) approach [55]. The following four sections serve as an outline and summarizes the contributions made to the field of PFC in this dissertation.

1.1 Thermodynamic Relationships for Bulk Crystalline and Liquid Phases in the PFC Model

We first present thermodynamic relationships between the free energy of the PFC model and thermodynamic state variables for bulk solid and liquid phases under hydrostatic pressure. These relationships are derived based on the thermodynamic formalism for crystalline solids introduced by Larché and Cahn [56] and detailed in Voorhees and Johnson [57]. We apply the relationships to examine the thermodynamic processes associated with varying the input parameters of the PFC model: temperature, θ, lattice spacing (associated with unit-cell volume, $\mathcal{V}_C^c$), and the average value of the PFC order parameter, $\bar{n}$. We show that varying $\bar{n}$ while holding $\mathcal{V}_C^c$ and θ constant in a PFC simulation reflects the thermodynamic process of adding or removing atoms to and from lattice sites while the number of lattice sites is constant. Furthermore, varying $\mathcal{V}_C^c$ while holding $\bar{n}$ and θ constant reflects the thermodynamic process of adding or removing lattice sites while the number of atoms is constant.

The equilibrium conditions between bulk crystalline solid and liquid phases are imposed on the thermodynamic relationships of the PFC model to obtain a procedure for determining solid-liquid phase coexistence. The resulting procedure is found to be in agreement with the method commonly used in the PFC community [24, 54, 58], justifying the use of the common-tangent construction to determine solid-liquid phase coexistence in the PFC model. Finally, we apply the procedure to an eighth-order-fit (EOF) PFC model that has been parameterized to body-centered-cubic (*bcc*) Fe [54] to demonstrate the procedure as well as to develop physical intuition about the PFC input parameters. We demonstrate that the EOF-PFC model parameterization does not predict stable *bcc* structures with positive vacancy densities. This result suggests an alternative parameterization of the PFC model, which requires the primary peak position of the two-body direct correlation function to shift as a function of $\bar{n}$.

1.2 Thermodynamic Relationships for Calculating Elastic Constants in the PFC Model

A major strength of the PFC model is its capability to naturally describe crystal elasticity and plasticity [23, 24]. However, in order for the PFC model to quantitatively predict non-equilibrium mechanical processes, such as plastic deformation [59, 60], the equilibrium mechanical properties of the model must be accurately represented. To this end, a procedure for calculating elastic constants that are consistent with the definitions of thermoelasticity theory for stressed crystals [61] was recently developed by Pisutha-Arnond et al. [53] for the phenomenologically based Swift-Hohenberg (SH) PFC model [23, 24, 62]. Although this procedure provides several important insights about the thermodynamic process of deformation in the PFC model, the equilibrium values calculated from the SH-based PFC model do not directly correspond to material properties measured experimentally or calculated with atomistic simulations. In order to parameterize the PFC model to match its mechanical equilibrium properties to those of experimental measurements or atomistic calculations, a thermodynamically consistent procedure for calculating elastic constants must be developed for the cDFT-based PFC model. Therefore, we build on the work of Pisutha-Arnond et al. [53] to derive such a procedure. We demonstrate that the procedure for calculating elastic constants in the cDFT-based PFC model requires the knowledge of the bulk modulus and pressure of the liquid reference state.

1.3 Numerical Implementation of Deformation in the PFC Model

The relationships for calculating elastic constants in the cDFT-based PFC model requires the numerical evaluation of the free energy of a deformed state. Numerical deformation is conventionally implemented in the PFC model by evaluating the free energy on coordinates that have been mapped to a desired deformed state via a deformation-gradient tensor [53, 55, 62]. Although straightforward, this method, requires interpolation of the order parameter values for shear-type deformations. Therefore, we explore two alternative numerical methods for applying deformation. The first alternative method maps the Laplacian operator in the PFC free energy from deformed to undeformed coordinates, which eliminates the need for interpolation. The second alternative method is formulated in Fourier space and applies deformation via a scaling of the wave vectors, which can be used when the PFC free energy is expressed in Fourier space. Using these methods, we evaluate the PFC free-energy density for an order parameter profile of a *bcc* structure, assuming the one-mode approximation, and compare the accuracy and efficiency of these methods. The Fourier-space method is then used to implement the relationships developed above to calculate the elastic constants and solid bulk modulus for *bcc* structures stabilized by the EOF-PFC model for two different pressure states.

1.4 PFC Model for a Diamond-Cubic Structure

We examine a more recently formulated structural PFC (XPFC) model, which uses a two-body DCF that is phenomenologically constructed from Gaussian functions [55]. Specifically, we focus on the XPFC model's capability to stabilize various crystal structures and investigate the existence of a stable *dc* structure within the PFC model. We demonstrate that a two-peak DCF constructed from Gaussian functions with positions at the first two peaks of the *dc* structure factor will stabilize a *dc* structure. A temperature-density phase diagram containing a *dc*-liquid phase coexistence region is calculated for this model.

We also examine how the solid-liquid interfacial energy of the *dc* structure depends on the shape of the DCF within the *dc*-PFC model. A relationship for solid-liquid interfacial energy as a function of temperature is developed for the *dc* structure by taking the peak heights of the Gaussian functions in the two-body DCF to change with a temperature parameter according to the functional form of the Debye-Waller Factor [55]. Additionally, since the excess energy associated with interfaces, defects, and strain is controlled by the peak width of the Gaussian functions [55], relationships for the dependence of interfacial energies on peak widths are also determined. These relationships can be used to parameterize the *dc*-PFC model to match interfacial energies to those measured experimentally or calculated from atomistic simulations.

CHAPTER II

Overview of The Phase-Field Crystal Model

In this chapter, we present an overview of the PFC model. We first consider a derivation of the PFC model based on the Swift-Hohenberg equation [63] developed for examining pattern formation arising from convective instability. This is the phenomenological approach by which PFC was first introduced. We then describe a derivation of the PFC model from a theoretical ground, which is based on classical density-functional theory (cDFT) [48, 49, 64].

2.1 The PFC Model Based on Swift-Hohenberg Equation

The Swift-Hohenberg equation [63] was originally developed to study the effects of thermal fluctuations on convective instability for Rayleigh-Bérnard convection in which fluids are trapped between a hot and cold plate. When the temperature difference between the two plates are large enough (i.e., the Rayleigh number is large enough), an instability arises where convective rolls form to transport the hot fluid to the cold plate and vice versa [65]. Elder et al. [23, 24] recognized that the conserved-dynamics form of the SH equation gives rise to a periodic structure that resembles the arrangement of atoms in a crystal, resulting in the inception of the PFC model.

The PFC free-energy functional based on the SH equation is

$$\mathcal{F}_{\mathrm{SH}}[\phi(\mathbf{r})] = \int d\mathbf{r} \left[g\frac{\phi(\mathbf{r})^4}{4} + \alpha\frac{\phi(\mathbf{r})^2}{2} + \frac{\phi(\mathbf{r})}{2}\lambda(q_0^2 + \nabla^2)^2\phi(\mathbf{r}) \right], \tag{2.1}$$

where λ and g are fitting parameters and q_0 is a constant that sets the periodicity of $\phi(\mathbf{r})$ when representing a crystalline phase. The coefficient α is set to be proportional to a degree of undercooling, or $\alpha \propto \Delta T$, where ΔT is the temperature difference from the melting point. This form of the PFC free-energy functional, Eq. (2.1), will be referred to as the SH-PFC form and denoted by the subscript SH. Additionally, the evolution of $\phi(\mathbf{r})$ is governed by the mass conservation equation, along with the flux driven by the variational derivative of the free energy with respect to $\phi(\mathbf{r})$ and thermal noise [23, 24]:

$$\frac{\partial\phi(\mathbf{r})}{\partial t} = M\nabla^2\frac{\delta\mathcal{F}_{\mathrm{SH}}[\phi(\mathbf{r})]}{\delta\phi(\mathbf{r})} + \eta, \tag{2.2}$$

where M is a phenomenological constant and η is a noise term that accounts for stochastic thermal fluctuations. The SH-PFC model is minimized by either a constant or periodic order parameter, $\phi(\mathbf{r})$. The constant value of $\phi(\mathbf{r})$ describes a liquid phase, while a $\phi(\mathbf{r})$ that is periodic in space represents a crystalline phase with a periodicity that matches the spatial arrangement of atoms in a crystal.

Equation (2.1) can be nondimensionalized by using the scaling scheme [24, 62]:

$$\tilde{\mathbf{r}} = q_0\mathbf{r}, \qquad \tilde{\epsilon} = -\frac{\alpha}{\lambda q_0^4}, \qquad \tilde{\phi}(\tilde{\mathbf{r}}) = \sqrt{\frac{g}{\lambda q_0^4}}\phi(\mathbf{r}), \qquad \tilde{t} = M\lambda q_0^{6-d}t, \tag{2.3}$$

where the tilde indicates the scaled dimensionless quantities and d denotes the spatial dimensionality of the problem. The typographical error in the definition of $\tilde{t}$ from Ref. [24] is corrected in Ref. [62]. Using the above scheme, one can express Eq. (2.1) in a scaled form as

$$\tilde{\mathcal{F}}_{\mathrm{SH}} = \frac{g}{\lambda^2 q_0^{8-d}} \mathcal{F}_{\mathrm{SH}} = \int \left(\frac{\tilde{\phi}(\tilde{\mathbf{r}})}{2} \left[-\tilde{\epsilon} + \left(\tilde{\nabla}^2 + 1 \right)^2 \right] \tilde{\phi}(\tilde{\mathbf{r}}) + \frac{\tilde{\phi}(\tilde{\mathbf{r}})^4}{4} \right) d\tilde{\mathbf{r}}, \tag{2.4}$$

where $\tilde{\epsilon}$ is related to undercooling. The evolution equation, Eq. (2.2), becomes [24]

$$\frac{\partial \tilde{\phi}(\tilde{\mathbf{r}})}{\partial \tilde{t}} = \tilde{\nabla}^2 \frac{\delta \tilde{\mathcal{F}}_{\mathrm{SH}}\big(\tilde{\phi}(\tilde{\mathbf{r}})\big)}{\delta \tilde{\phi}(\tilde{\mathbf{r}})} + \tilde{\eta}, \tag{2.5}$$

where $\tilde{\eta}$ represents the scaled thermal fluctuations.

Although simplistic in form, the SH-PFC free-energy functional in Eq. (2.4) gives rise to fairly complex phase diagrams containing *bcc*, *fcc*, *hcp*, rod and stripe phases in three dimensions [24, 66]. Along with the evolution equation of (2.5), the SH-PFC model has been used to study a wide variety of complex phenomena that simultaneously involve crystal orientations, anisotropic interfacial energies, and plastic and elastic deformations [24, 26, 27, 67].

2.2 The PFC Model Based on cDFT

Despite the success of the SH-PFC model in studying complex material phenomena, its application to physical material systems is limited due to the phenomenological origin of its free-energy functional. Later, Elder et al. [45] established a connection between the PFC model and cDFT, providing links between the PFC model parameters and measurable quantities in experiments and atomistic simulations and enabling several systematic improvements to the model.

In this section, we provide an overview of cDFT followed by the derivation of several variations of the PFC model that depend on the choice of the two-body DCF defined in Fourier space. A thorough review of different formulations and extensions of the PFC model is given in Refs. [65, 68]. Below, we consider four different formulations of the model: (i) a fourth-order-polynomial fit (FOF) approximation of the two-body DCF, which is the original cDFT-based PFC model [45], (ii) an eighth-order-polynomial fit (EOF) approximation of the two-body DCF, which has been shown to accurately predict multiple thermodynamic properties of *bcc* Fe simultaneously [54], (iii) a rational-function-fit (RFF) approximation of the two-body DCF, which has been used to examine the short-wavelength contributions of the DCF for cDFT and the PFC model [69], and (iv) a Gaussian approximation of the two-body DCF, which has been used to selectively stabilize different crystal structures by adjusting the peak heights and location of the two-body DCF [55]. Finally, the link between the PFC evolution equation in Eq. (2.5) and dynamic density-functional theory (dDFT) [70, 71, 72] is discussed.

2.2.1 Overview of cDFT

We first provide an overview of cDFT to formally define the atomic probability density and the Helmholtz free energy. The theory resembles the density functional treatment used in quantum mechanics, where the energy is expressed as a functional of the electron-density field [73]. However, unlike the density functional treatment used in quantum mechanics, cDFT considers the equilibrium one-body density, $\rho_{eq}(\mathbf{r})$, which is the grand canonical average of the density operator, $\sum_i \delta(\mathbf{r}-\mathbf{r}_i)$ [49, 74]:

$$\rho_{eq}(\mathbf{r}) = \left\langle \sum_i \delta(\mathbf{r}-\mathbf{r}_i) \right\rangle_{GC} , \tag{2.6}$$

where $\mathbf{r}_i$ is the particle position, $\delta(\mathbf{r})$ is the Dirac delta function, and the subscript GC denotes the grand canonical ensemble.

The key theorem in the formulation of cDFT is the existence of a one-to-one correspondence between $\rho_{eq}(\mathbf{r})$ and an external potential, $V_{ext}(\mathbf{r})$, at a given temperature T, and chemical potential μ [48, 49, 64]. This theorem enables a variational formulation for an atomic-probability density, $\rho(\mathbf{r})$, which involves an intrinsic free energy functional, $\mathcal{F}[\rho(\mathbf{r})]$. When $\rho(\mathbf{r}) = \rho_{eq}(\mathbf{r})$, for a corresponding $V_{ext}(\mathbf{r})$, the quantity $\mathcal{F}[\rho(\mathbf{r})]$ becomes the Helmholtz free energy and satisfies [48, 49, 64, 75]

$$\left.\frac{\delta\mathcal{F}[\rho(\mathbf{r})]}{\delta\rho(\mathbf{r})}\right|_{\rho=\rho_{eq}} + V_{ext}(\mathbf{r}) - \mu = 0. \tag{2.7}$$

Following Refs. [48, 49, 64], $\mathcal{F}[\rho(\mathbf{r})]$ is divided into ideal and excess parts, i.e., $\mathcal{F}[\rho(\mathbf{r})] = \mathcal{F}_{id}[\rho(\mathbf{r})] + \mathcal{F}_{ex}[\rho(\mathbf{r})]$. The ideal contribution can be obtained exactly from the ideal gas system and is given by

$$\mathcal{F}_{id}[\rho(\mathbf{r})] = k_BT\int d\mathbf{r}\rho(\mathbf{r})\left\{\ln[\rho(\mathbf{r})\lambda_T^3] - 1\right\}, \tag{2.8}$$

where λ_T is the de Broglie wavelength and k_B is the Boltzmann constant. The excess contribution involves direct correlation functions (DCFs) that are generated through the functional derivative

$$C^{(n)}(\mathbf{r}_1, ..., \mathbf{r}_n; [\rho]) = -\frac{1}{k_BT}\frac{\delta^n\mathcal{F}_{ex}[\rho(\mathbf{r})]}{\delta\rho(\mathbf{r}_1)...\delta\rho(\mathbf{r}_n)}. \tag{2.9}$$

The function $C^{(n)}(\mathbf{r}_1, ..., \mathbf{r}_n; [\rho])$ is the n-body DCF, which contains the information of the interparticle interactions and determines structural properties of the system. In general there is no exact expression for $\mathcal{F}_{ex}[\rho(\mathbf{r})]$, and thus numerous techniques have been proposed to approximate this quantity [48, 49].

In the context of freezing, $\mathcal{F}_{ex}[\rho(\mathbf{r})]$ is approximated with a functional Taylor expansion around a liquid reference density, ρ_0, that is truncated beyond the second-order term. Combining the approximate form of $\mathcal{F}_{ex}[\rho(\mathbf{r})]$ with $\mathcal{F}_{id}[\rho(\mathbf{r})]$, the free energy can be expressed as follows [46, 47]:

$$\begin{aligned}\frac{\mathcal{F}[\rho(\mathbf{r})]}{k_BT} &= \frac{\mathcal{F}[\rho_0]}{k_BT}+\frac{\mu_0}{k_BT}\int d\mathbf{r}\Delta\rho(\mathbf{r})+\int d\mathbf{r}\left\{\rho(\mathbf{r})\ln\left[\frac{\rho(\mathbf{r})}{\rho_0}\right]-\Delta\rho(\mathbf{r})\right\}\\ &-\frac{1}{2}\int\int d\mathbf{r}_1 d\mathbf{r}_2\Delta\rho(\mathbf{r}_1)C^{(2)}(\mathbf{r}_1,\mathbf{r}_2;[\rho_0])\Delta\rho(\mathbf{r}_2),\end{aligned} \tag{2.10}$$

where μ_0 is the chemical potential of the liquid reference state, $\Delta\rho(\mathbf{r})\equiv\rho(\mathbf{r})-\rho_0$, and $C^{(2)}(\mathbf{r}_1,\mathbf{r}_2;[\rho_0])$ is the two-body DCF of the reference liquid state. Additional approximations are applied to Eq. (2.10) to obtain PFC models. In particular, the two-body DCF can be approximated in various manners, leading to different formulations of PFC, as will be discussed below.

2.2.2 Derivation of PFC from cDFT

The original cDFT-based formulation of the PFC model involves approximating the two-body DCF with a fourth-order polynomial, resulting in a form analogous to the SH-PFC model. First, a scaled dimensionless number-density,

$$n(\mathbf{r})\equiv\frac{\rho(\mathbf{r})-\rho_0}{\rho_0}, \tag{2.11}$$

is used to rewrite Eq. (2.10) as

$$\begin{aligned}\frac{\Delta\mathcal{F}[n(\mathbf{r})]}{\rho_0 k_BT} &= \int d\mathbf{r}\Bigg\{[1+n(\mathbf{r})]\ln[1+n(\mathbf{r})]-n(\mathbf{r})+\frac{\mu_0 n(\mathbf{r})}{k_BT}\\ &-\frac{\rho_0 n(\mathbf{r})}{2}\int d\mathbf{r}'C^{(2)}(|\mathbf{r}-\mathbf{r}'|)n(\mathbf{r}')\Bigg\},\end{aligned} \tag{2.12}$$

where the two-body DCF, $C^{(2)}(\mid\mathbf{r}-\mathbf{r}'\mid)$, is assumed to be spherically symmetric. This assumption is valid for a system whose interaction potential is isotropic. Following Ref. [45], two approximations are made to Eq. (2.12). The first approximation, which is used in all forms of the PFC, is a polynomial expansion of the first two terms of the integrand in Eq. (2.12),

$$[1+n(\mathbf{r})]\ln[1+n(\mathbf{r})]-n(\mathbf{r}) \approx \frac{1}{2}n(\mathbf{r})^2-\frac{a_t}{6}n(\mathbf{r})^3+\frac{b_t}{12}n(\mathbf{r})^4, \tag{2.13}$$

where the constants a_t and b_t are introduced to account for contributions from the zeroth-mode of higher-order DCFs [30, 32, 54, 55, 76, 77]. A Taylor expansion ($a_t = 1$ and $b_t = 1$) was used in the original derivation presented by Elder et al. [45]. The second approximation is the Taylor expansion of the two-body DCF in Fourier space

$$\rho_0\hat{C}^{(2)}(k) \approx -\mathcal{C}_0+\mathcal{C}_2k^2-\mathcal{C}_4k^4, \tag{2.14}$$

where $\mathcal{C}_0$, $\mathcal{C}_2$, and $\mathcal{C}_4$ are fitting constants, k is the magnitude of the wave vector, and the hat denotes the Fourier transform of the corresponding quantity. Figure 2.1 shows the two-body DCF from molecular dynamics simulations [78], $\rho_0\hat{C}^{(2)}_{MD}(k)$, and the approximations of Eq. (2.14) with two different sets of $\mathcal{C}_0$, $\mathcal{C}_2$, and $\mathcal{C}_4$. The first approximation, shown as the red dotted curve, captures the value of $\rho_0\hat{C}^{(2)}_{MD}(0)$, the maximum value of $\rho_0\hat{C}^{(2)}_{MD}(k)$, and its location [54]. The second approximation, shown as the blue dashed curve, also captures the maximum value of $\rho_0\hat{C}^{(2)}_{MD}(k)$ and its location, but instead of capturing $\rho_0\hat{C}^{(2)}_{MD}(0)$, it matches the curvature of the maximum [78].

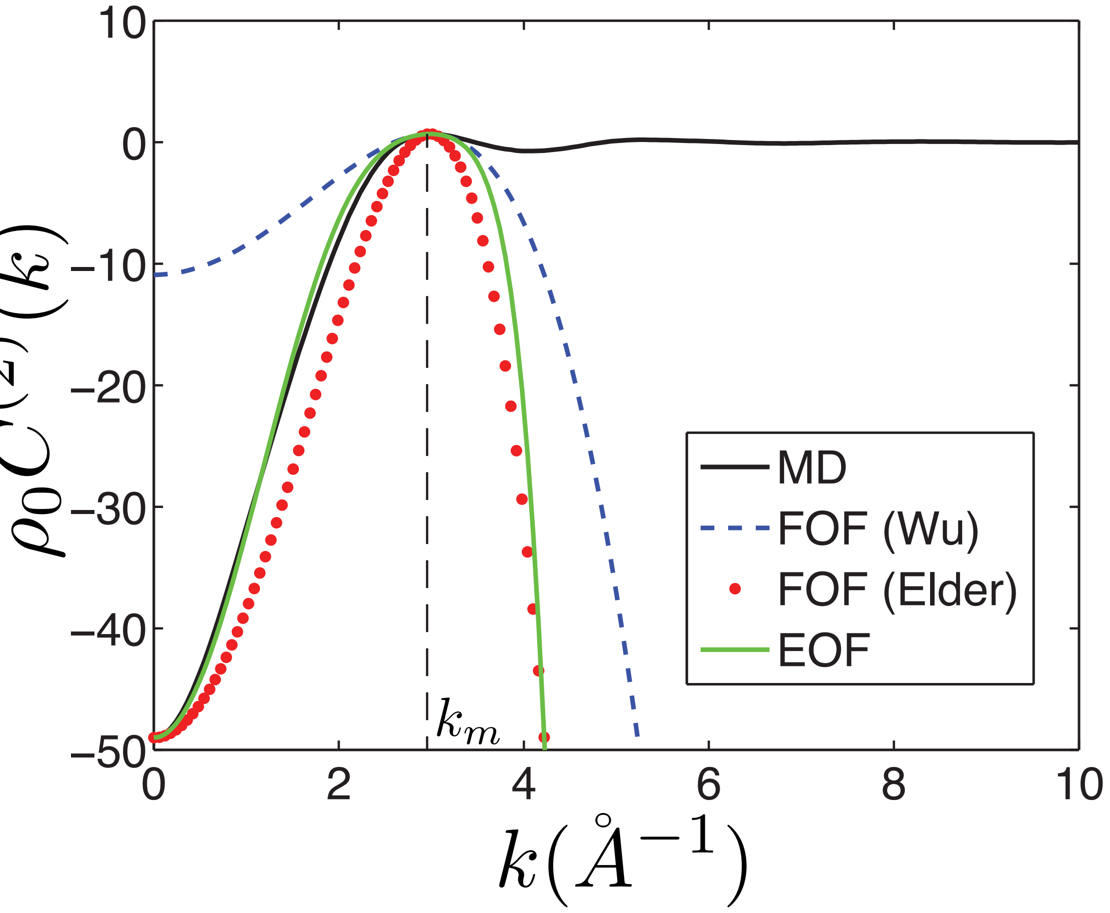

Figure 2.1: Two-body direct correlation functions (DCFs). The variables ρ_0 is the reference liquid density, k is the magnitude of the wave vector, and k_m is the value of k corresponding to the maximum of the two-body DCF (marked by the vertical dashed black line). The black solid curve denotes the DCF from molecular dynamics simulations, $\rho_0\hat{C}^{(2)}_{MD}(k)$, of Fe at 1772 K [78]. The red dotted curve and the blue dashed curve denote the fourth-order-polynomial fit (Eq. (2.14)) with different choices of fitting parameters ($\mathcal{C}_0$, $\mathcal{C}_2$, and $\mathcal{C}_4$). The red dotted curve captures the value of $\rho_0\hat{C}^{(2)}_{MD}(0)$, the value of k_m, and $\rho_0\hat{C}^{(2)}_{MD}(k_m)$. The blue dashed curve captures the value of k_m and $\rho_0\hat{C}^{(2)}_{MD}(k_m)$, and the curvature at $\rho_0\hat{C}^{(2)}_{MD}(k_m)$. The green solid curve denotes an eighth-order-polynomial approximation (Eq. (2.18)), which captures all four features of $\rho_0\hat{C}^{(2)}_{MD}(k)$ that are mentioned previously. This figure is based on Ref. [54].

The inverse Fourier transform of Eq. (2.14) yields an approximated two-body DCF of the form

$$\rho_0 C^{(2)}(|\mathbf{r}-\mathbf{r}'|) \approx (-\mathcal{C}_0 - \mathcal{C}_2\nabla^2 - \mathcal{C}_4\nabla^4)\delta(|\mathbf{r}-\mathbf{r}'|). \tag{2.15}$$

Equations (2.13) and (2.15) are substituted into Eq. (2.12) to obtain

$$\begin{aligned}\frac{\Delta\mathcal{F}_{\mathrm{FOF}}[n(\mathbf{r})]}{\rho_0 k_B T} &= \int d\mathbf{r}\Bigg[\frac{\mu_0 n(\mathbf{r})}{k_B T} + n(\mathbf{r})\frac{1+\mathcal{C}_0+\mathcal{C}_2\nabla^2+\mathcal{C}_4\nabla^4}{2}n(\mathbf{r}) \\ &\qquad -\frac{a_t}{6}n(\mathbf{r})^3 + \frac{b_t}{12}n(\mathbf{r})^4\Bigg],\end{aligned} \tag{2.16}$$

where $\Delta\mathcal{F}_{\mathrm{FOF}}$ is the PFC free energy and the subscript FOF denotes that a fourth-order polynomial is used to approximate the two-body DCF in Fourier space (see Eq. (2.14)). The linkage between the cDFT and the PFC free energies shows that the PFC free energy is the Helmholtz free energy change from a reference state when $n(\mathbf{r})$ takes the equilibrium profile, $n_{eq}(\mathbf{r})$, for a given external potential.

As pointed out in Ref. [54], the PFC free energy of Eq. (2.16) does not produce a stable crystal structure when $a_t = b_t = 1$. In order for a stable crystal structure to arise from Eq. (2.16), either the values of a_t and b_t need to be adjusted [54], or the scaled density is alternatively defined [45] to be

$$n(\mathbf{r}) \equiv \frac{\rho(\mathbf{r})-\bar{\rho}}{\bar{\rho}}, \tag{2.17}$$

where $\bar{\rho} \equiv 1/V\int\rho(\mathbf{r})dV$ is the average density of the system. As mentioned earlier, change in a_t and b_t can be attributed to the zeroth-mode of higher-order DCFs. The redefinition of $n(\mathbf{r})$ may introduce an inconsistency since the density is no longer scaled with respect to the reference state at which the correlation function is obtained.

2.2.3 Eighth-Order-Polynomial Fit PFC Formulation

Jaatinen et al. [54] attempted to use the FOF-PFC formulation of Eq. (2.16) to describe multiple thermodynamic properties of Fe at the melting temperature and found the model too limited due to the small number of available fitting parameters. They overcame this problem by using the approximation of the ideal contribution of the free energy in Eq. (2.13) and proposing an improved EOF approximation of the two-body DCF in Fourier space,

$$\rho_0 \hat{C}^{(2)}_{\mathrm{EOF}}(k) = \mathcal{C}_m - \Gamma \left(\frac{k_m^2 - k^2}{k_m^2} \right)^2 - E_B \left(\frac{k_m^2 - k^2}{k_m^2} \right)^4 , \tag{2.18}$$

where

$$\Gamma = -\frac{k_m^2 \mathcal{C}_c}{8}, \quad E_B = \mathcal{C}_m - \mathcal{C}_0 - \Gamma, \tag{2.19}$$

and k_m, $\mathcal{C}_0$, $\mathcal{C}_m$ as well as $\mathcal{C}_c$ are fitting constants. Compared with the two-body DCF approximation in Eq. (2.14), this model provides one additional fitting parameter. The corresponding free energy is

$$\begin{aligned} \frac{\Delta \mathcal{F}_{\mathrm{EOF}}[n(\mathbf{r})]}{k_B T \rho_0} &= \int d\mathbf{r} \Bigg[\frac{n(\mathbf{r})}{2} \left(1 - \mathcal{C}_m + \Gamma \left(\frac{k_m^2 + \nabla^2}{k_m^2} \right)^2 + E_B \left(\frac{k_m^2 + \nabla^2}{k_m^2} \right)^4 \right) n(\mathbf{r}) \\ & -\frac{a_t}{6} n(\mathbf{r})^3 + \frac{b_t}{12} n(\mathbf{r})^4 \Bigg]. \end{aligned} \tag{2.20}$$

This new form of the free energy allows the first peak of the two-body DCF of Fe to be captured more accurately, as shown in Fig. 2.1. Specifically, the fitting constants were selected so that the EOF matches (i) the value of the DCF at $k = 0$, (ii) the value of the DCF at the first peak, (iii) the location of the first peak, and (iv) the curvature of the first peak. Furthermore, in Ref. [54], the values of a_t and b_t were chosen to match the equilibrium amplitude of the density wave in the solid phase to those calculated for the solid phase in MD simulations.

The EOF-based PFC model has been parameterized to match solid-liquid interfacial energy and bulk modulus of *bcc* Fe, and was used to calculate grain boundary energies that are in reasonable agreement with MD calculations [54]. The bulk modulus calculated from the model is 94.5GPa, while the solid-liquid interfacial energies for the (100), (110), and (111) interfaces were 165.7, 161.5, and 157.2 ergs/cm^2, respectively [54]. The fitting parameters of the parameterized model are listed in table 2.1. The EOF for the listed parameter values is plotted as the green curve in Fig. 2.1.

Constant	Value
a_t	0.6917
b_t	0.08540
k_m	$2.985\mathring{A}^{-1}$
$\mathcal{C}_0$	$-49\mathring{A}^{-3}$
$1-\mathcal{C}_m$	$0.332\mathring{A}^{-3}$
$\mathcal{C}_c$	$-10.40\mathring{A}^{-1}$
ρ_0	$0.0801\mathring{A}^{-3}$

Table 2.1: Constants used in the work of Ref. [54].

2.2.4 Rational-Function-Fit Formulation

The FOF- and EOF-PFC formulations presented so far are based on fits to the two-body DCF up to the first peak. As a result, the short-wavelength features of the DCF cannot be captured by these formulations. In order to examine the contributions of the short-wavelength features of the two-body DCF, a RFF approximation to the two-body DCF in Fourier space was presented by Pisutha-Arnond et al. [69]. Their study on *bcc* Fe showed that the short-wavelength contributions of the two-body DCF affect the thermodynamic properties calculated from the model. Furthermore, they showed that the RFF technique can be used to empirically parameterize the two-body DCF to increase the computational efficiency of cDFT while retaining its accuracy.

In the RFF formulation, the two-body DCF is approximated by a rational function,

$$\rho_0 \hat{C}^{(2)}_{\mathrm{RFF}}(k) = \frac{P(k)}{Q(k)}, \tag{2.21}$$

where $P(k)$ and $Q(k)$ are polynomials of k with the order of $P(k)/Q(k)$ being $1/k^2$. This rational function can be decomposed into a summation of partial fractions as

$$\rho_0 \hat{C}^{(2)}_{\mathrm{RFF}}(k) = \sum_j \left[\frac{A_j}{k^2 + \alpha_j} + \frac{A_j^*}{k^2 + \alpha_j^*} \right], \tag{2.22}$$

where A_j and α_j are fitting constants and the asterisk denotes their complex conjugate. The RFF captures the oscillatory behavior of the two-body DCF, as shown in Fig. 2.2, where the approximation of the two-body DCF improves as the number of partial-fraction terms in Eq. (2.22) increases (or equivalently the order of $P(k)$ and $Q(k)$ increases).

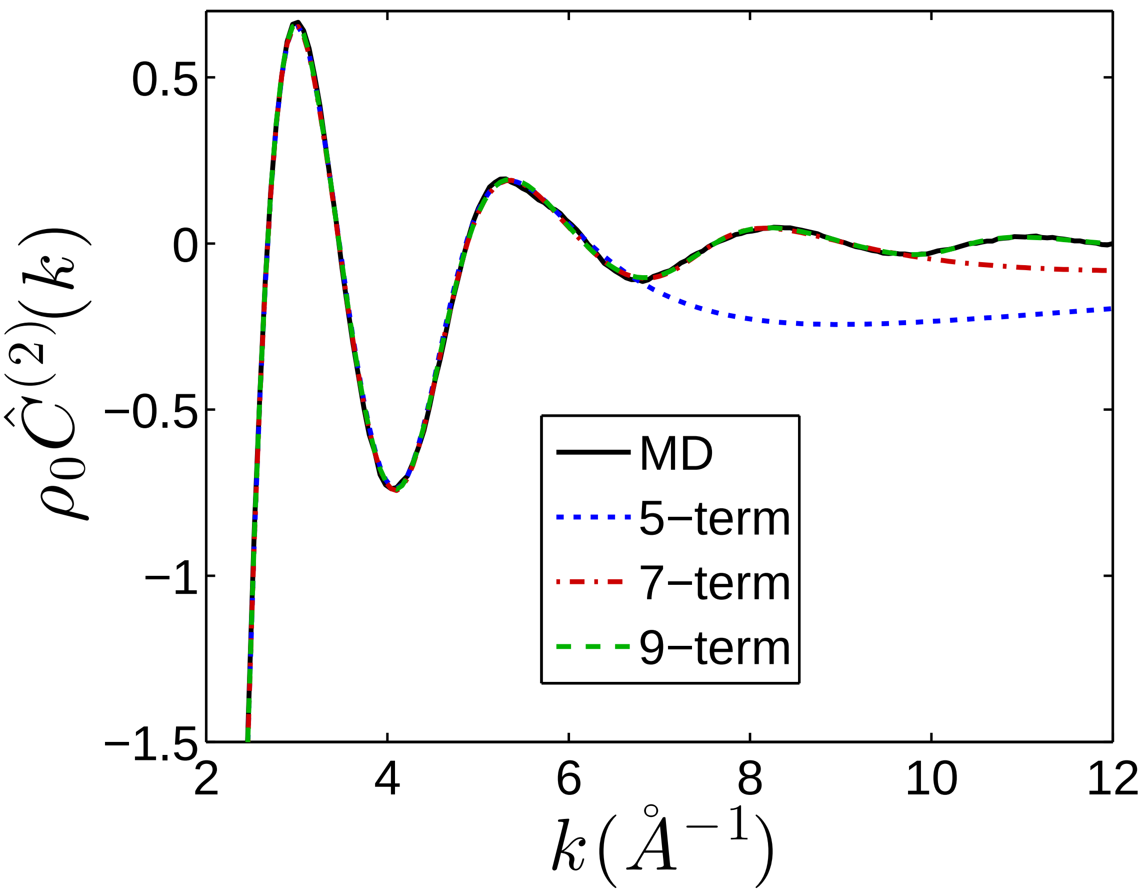

Figure 2.2: Different rational-function fits (RFF) to the two-body direct correlation function (DCF) of Fe at 1772 K. ρ_0 is the reference liquid density and k is the magnitude of the wave vector. The black solid curve denotes the two-body DCF from molecular dynamics simulations [78] $\left(\hat{C}^{(2)}_{MD}(k)\right)$. The curves denote the RFFs with 5 (dotted blue), 7 (dot-dashed red), and 9 (dashed green) partial-fraction terms. The fit to $\hat{C}^{(2)}_{MD}(k)$ improves as the number of terms in the RFF increases. This figure is based Ref. [69]

The partial fraction decomposition in Eq. (2.22) also allows one to evaluate the convolution integral in Eq. (2.12),

$$\mathcal{I}_c(\mathbf{r}) = \int C^{(2)}(|\mathbf{r}-\mathbf{r}'|)n(\mathbf{r}')d\mathbf{r}', \tag{2.23}$$

in real space by solving a set of inhomogeneous Helmholtz equations. When $\hat{C}^{(2)}(k)$ is approximated with $\hat{C}^{(2)}_{\mathrm{RFF}}(k)$, $\mathcal{I}_c(\mathbf{r})$ can be expressed as

$$\begin{aligned}\mathcal{I}_c(\mathbf{r}) &= \int C^{(2)}_{\mathrm{RFF}}(|\mathbf{r}-\mathbf{r}'|)n(\mathbf{r}')d\mathbf{r}' \\ &= \sum_j [L_j(\mathbf{r}) + L_j^*(\mathbf{r})],\end{aligned} \tag{2.24}$$

where $L_j(\mathbf{r})$ and $L_j^*(\mathbf{r})$ are solutions to the inhomogeneous Helmholtz equations [69],

$$\begin{aligned}-\nabla^2 L_j(\mathbf{r}) + \alpha_j L_j(\mathbf{r}) &= A_j n(\mathbf{r}) \\ -\nabla^2 L_j^*(\mathbf{r}) + \alpha_j L_j^*(\mathbf{r}) &= A_j^* n(\mathbf{r}).\end{aligned} \tag{2.25}$$

Therefore, the RFF formulation also allows one to solve the PFC equation with an improved DCF in real space, where techniques such as adaptive mesh refinement and the finite element method can be employed [69].

2.2.5 Structural PFC (XPFC) Formulation

Unlike the EOF- and RFF-PFC formulations, which use approximations to a physical two-body DCF as input, the structural PFC (XPFC) model uses a phenomenologically constructed two-body DCF as input [55, 58]. In this method, the emergence of different crystal structures is controlled by setting the positions of the peaks in a two-body DCF to correspond to those in the structure factor. Specifically, the two-body DCF of the XPFC model is constructed from a combination of modulated Gaussian functions, each of which is centered at the position of a peak in the structure factor,

$$\rho_0 \hat{C}^{(2)}(k) = \max\big(G^i(k), G^{i+1}(k), \ldots, G^N(k)\big), \tag{2.26}$$

where N is the total number of Gaussian functions used in the approximation of the DCF, and

$$G^i(k) = \exp\left(-\frac{\sigma^2 k_i^2}{2\lambda_i \beta_i}\right) \exp\left(-\frac{(k-k_i)^2}{2\alpha_i^2}\right) \tag{2.27}$$

is the modulated Gaussian function (i.e., a Gaussian function with its height modified by an exponential function). The subscripts and superscripts i denote the i^{th} family of crystallographic planes that are being considered; the families of planes are typically enumerated in order of decreasing interplanar spacings, where $i = 1$ corresponds to the family of crystallographic planes with the largest interplanar spacing. The parameter k_i specifies the position of the i^{th} Gaussian peak and the value of k_1 corresponds to the reciprocal lattice spacing of a crystal structure; α_i corresponds to the root-mean-square width of the i^{th} Gaussian peak and controls the excess energy associated with defects, interfaces, and strain [55]; σ controls the height of the Gaussian peaks and is related to temperature [55]; λ_i and β_i are the planar atomic density and the number of planar symmetries of the i^{th} family of crystallographic planes, respectively, and control how much the height of the Gaussian functions change when σ is adjusted. Since the parameter k_i also exists in the exponential term in front of the Gaussian functions in Eq. (2.27), k_i also affects the change in the height of the Gaussian functions when σ is adjusted.

Each value of k_i sets the interplanar spacing, L_i, for a family of crystallographic planes within a crystal structure; specifically, $k_i = 2\pi/L_i$. For example, the k_1 and k_2 values for a *bcc* structure corresponds to the {110} and {200} families of planes, respectively, and have values of $k_1 = 2\pi\sqrt{2}/a_{bcc}$ and $k_2 = 4\pi/a_{bcc}$, where a_{bcc} is the lattice constant of the *bcc* structure. On the other hand, the k_1 and k_2 values for an

fcc structure correspond to the {111} and {200} families of planes, respectively, and have values of $k_1 = 2\pi\sqrt{3}/a_{fcc}$ and $k_2 = 4\pi/a_{fcc}$, where a_{fcc} is the lattice constant of the fcc structure. The planes corresponding to the k_1 and k_2 reciprocal lattice spacings in one unit-cell of the bcc and fcc structures are illustrated in Fig. 2.3.

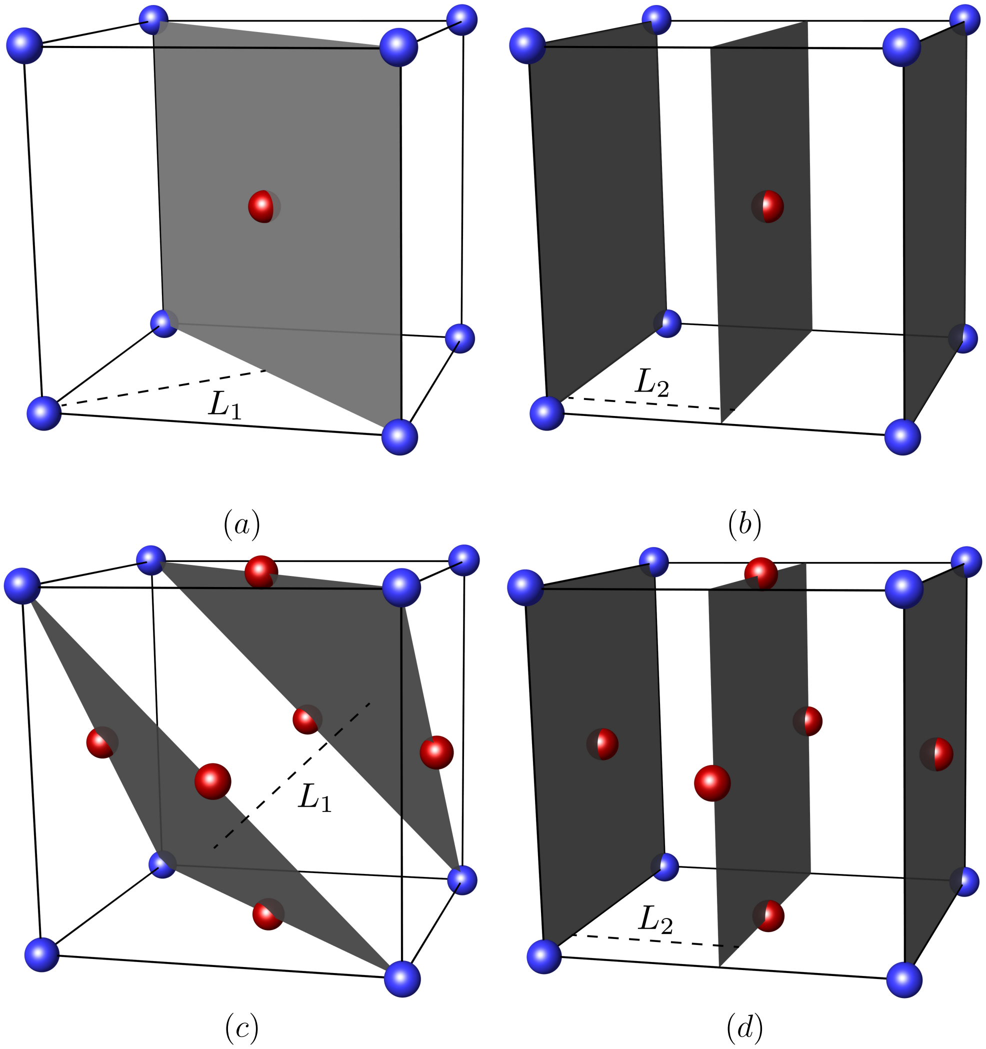

Figure 2.3: Schematic of the (a) (110) and (b) (200) planes of the bcc structure, as well as (c) (111) and (d) (200) planes of the fcc structure. Figure is based on Ref. [58]. The corner lattice sites are colored red, while the body-centered (a and b) and face-centered (c and d) lattice sites are colored blue.

As demonstrated by Greenwood et al. [58], the XPFC model for the *bcc* structure can be constructed with a two-body DCF that is approximated with a single Gaussian function centered at $k_1 = 2\pi\sqrt{2}/a_{bcc}$ in Fourier space. On the other hand, the fcc structure is stabilized by two Gaussian functions centered at $k_1 = 2\pi\sqrt{3}/a_{fcc}$ and $k_2 = 4\pi/a_{fcc}$ at sufficiently low temperatures. Note that the ratio of the peak positions of the fcc structure, $k_2/k_1 = \sqrt{4/3}$, is independent of a_{fcc}.

Although the XPFC model lacks a direct link to physical systems (unlike other cDFT-based PFC models that use a physical DCF), it has the advantage of employing a DCF that is easily customizable. The peak heights and positions of the two-body DCF in the XPFC model has been adjusted to systematically stabilize a wide variety of crystal structures, such as the *bcc*, fcc, simple-cubic (*sc*) and *hcp* phases in three dimensions [55, 58], and square and triangle phases in two dimensions [55]. Furthermore, the XPFC model has been applied to study a diverse range of materials phenomena, including solute drag effects on grain boundary motion [79], clustering and precipitation in an Al-Cu alloy [80, 81], and the stability of stacking faults and partial dislocations [28].

2.2.6 Evolution Equation from dDFT

The evolution equation for cDFT can be formulated by introducing the time-dependent one-body density, $\rho(\mathbf{r}, t)$, as an ensemble average of the instantaneous density operator over the realizations of random thermal noise [70, 71, 72]. By considering overdamped Brownian dynamics without hydrodynamic interactions, one can describe the evolution of a particle system by stochastic differential equations governing particle positions (Langevin equations), or a deterministic evolution equation of a probability density (Smoluchowski equation). Marconi and Tarazona [71, 72] employed the former equations while Archer and Evans [70] started with the latter equation to arrive at the equation of motion for $\rho(\mathbf{r},t)$:

$$\frac{\partial\rho(\mathbf{r},t)}{\partial t} = \gamma^{-1}\nabla\cdot\left[\rho(\mathbf{r},t)\nabla\frac{\delta\mathcal{F}\big(\rho(\mathbf{r},t)\big)}{\delta\rho(\mathbf{r},t)}\right], \tag{2.28}$$

where γ is the mobility. By writing $\rho(\mathbf{r},t) = \rho_0 n(\mathbf{r},t) + \rho_0$, the evolution equation in Eq. (2.28), becomes

$$\frac{\partial n(\mathbf{r},\tau)}{\partial\tau} = \nabla\cdot\left\{[n(\mathbf{r},\tau)+1]\nabla\frac{\delta\Delta\tilde{\mathcal{F}}\big(n(\mathbf{r},\tau)\big)}{\delta n(\mathbf{r},\tau)}\right\}, \tag{2.29}$$

where $\tau = \gamma^{-1}k_BT\rho_0 t$ is the rescaled time and $\Delta\tilde{\mathcal{F}} = \Delta\mathcal{F}/k_BT\rho_0$ is the dimensionless free energy.

As suggested by Teeffelen et al. [82], one can obtain the PFC evolution equation by replacing $n(\mathbf{r},\tau)$ with $\bar{n}$. With this approximation, we obtain

$$\frac{\partial n(\mathbf{r},\tau)}{\partial\tau} = (\bar{n}+1)\nabla^2\frac{\delta\Delta\tilde{\mathcal{F}}\big(n(\mathbf{r},\tau)\big)}{\delta n(\mathbf{r},\tau)}, \tag{2.30}$$

which, aside from the noise term, has a similar form to the PFC evolution equation, Eq. (2.5). From the dDFT derivation, the noise term will not be present in the evolution equation because of the noise averaging procedure that is performed on the Langevin equations. Therefore, the presence of the noise term in Eq. (2.5) is not justified from a fundamental viewpoint because it adds fluctuations that have already been accounted for [72]. However, the study by Archer and Rauscher [83] showed that the noise term is present in the evolution equation if one instead interprets the density field as a temporally coarse-grained density operator. Nevertheless, if one adopts this interpretation, the free energy functional in the evolution equation will no longer be the Helmholtz free energy, and its interpretation is yet to be developed. Despite these different viewpoints, the noise term is often included on the basis of necessity to model phenomena such as homogeneous nucleation that cannot be simulated without the noise term.

CHAPTER III

Thermodynamic Relationships for Bulk Crystalline and Liquid Phases in the Phase-Field Crystal Model

Although the PFC model parameters have been linked to measurable quantities, the procedures for calculating equilibrium material properties from the PFC model are not straightforward [53] because the thermodynamic interpretation of the PFC free energy has not been fully developed. In this chapter, we present a thermodynamic interpretation for bulk phases of the PFC model. As a starting point, we follow the thermodynamic formalism for a crystalline system that was introduced by Larché and Cahn [56] and was detailed in Voorhees and Johnson [57] to derive a thermodynamic relationship between the PFC free energy and thermodynamic state variables. We then apply the equilibrium conditions between a bulk crystal and liquid from Voorhees and Johnson [57] to the thermodynamic relationship for the PFC model to obtain a thermodynamically consistent procedure for determining solid-liquid phase coexistence, which is demonstrated to be in agreement with the common-tangent construction commonly used in the PFC community [24, 58, 66]. Finally, we apply this procedure to a PFC model parameterized for body-centered-cubic (*bcc*) Fe [54] via an eighth-order fit (EOF) of the two-body DCF in Fourier space. The EOF-PFC model is used to demonstrate the procedure as well as to examine how the average value of the order parameter, $\bar{n}$, and lattice spacing, a, are related to the number of atoms and vacancies in a crystal simulated by the PFC model.

This chapter is outlined as follows. In Section 3.1, we describe the PFC free-energy density for bulk crystalline and liquid phases. In Section 3.2, we describe the thermodynamics for bulk liquid and crystalline phases. In Section 3.3, we derive the free-energy densities (FED) for the bulk liquid and crystalline phases, which serve as the basis for the thermodynamic interpretation of the PFC free energy. In Section 3.5, we present the equilibrium conditions between a bulk crystal and liquid phase and apply these conditions to the thermodynamic relationship for the PFC model to obtain a procedure for determining solid-liquid phase coexistence. In Section 3.6, this procedure is applied to the EOF-PFC model to demonstrate the procedure, as well as to develop physical intuition about the PFC model parameters. For this model, we derive an upper-bound expression for $\bar{n}$, above which the vacancy density becomes negative. We further show that the EOF-PFC model does not stabilize *bcc* structures if values of $\bar{n}$ are below the upper bound. These results indicate a need for an alternative parameterization of the PFC model. Finally, in Section 3.7, we summarize the results of this chapter.

3.1 PFC Free-Energy Density for Bulk Crystalline and Liquid Phases

Thermodynamics describe the properties of systems that are in equilibrium. In the PFC model, an equilibrium density profile, $n_{eq}(\mathbf{r})$, is obtained by relaxing $n(\mathbf{r})$ via conserved dissipative dynamics [23, 24, 45],

$$\frac{\partial n(\mathbf{r})}{\partial t} = \nabla^2 \frac{\delta \Delta \mathcal{F}[n(\mathbf{r})]}{\delta n(\mathbf{r})}, \tag{3.1}$$

until a stationary state is reached. This state corresponds to the lowest energy state for the given constraints on the order-parameter average, $\bar{n} \equiv (1/\mathcal{V}) \int n(\mathbf{r}) d\mathbf{r}$, and lattice spacing, a, and will be referred to as the single-phase equilibrium state. In a single-phase equilibrium bulk liquid phase (i.e., away from any interfaces or boundaries), $n_{eq}(\mathbf{r}) = n_{eq}^{\text{bulk},l}(\mathbf{r}) = \bar{n}$. Thus, a coarse-grained FED for the bulk liquid phase is $\Delta f_{\text{PFC}}^{\text{bulk},l}(\bar{n}) \equiv \Delta f_{id}(\bar{n}) + \Delta f_{ex}(\bar{n})$. On the other hand, in a single-phase equilibrium bulk crystalline phase, $n_{eq}(\mathbf{r}) = n_{eq}^{\text{bulk},c}(\mathbf{r})$, which has a density profile that is periodic with a uniform amplitude for each value of $\bar{n}$. Therefore, the free energy of a bulk crystalline phase corresponding to $n_{eq}^{\text{bulk},c}(\mathbf{r})$ is a function of $\bar{n}$, a, and system volume, $\mathcal{V}$. Consequently, the coarse-grained FED of a bulk crystalline phase is given by

$$\Delta f_{\text{PFC}}^{\text{bulk},c}(\bar{n}, a) \equiv \lim_{\mathcal{V} \to \infty} \left(\frac{\Delta \mathcal{F}[n_{eq}^{\text{bulk},c}(\mathbf{r})]}{\mathcal{V}} \right), \tag{3.2}$$

where the limit indicates that the system volume is large enough such that the bulk phase is far away from any interfaces or boundaries. The definition in Eq. (3.2) shows that the PFC FED of a bulk crystalline phase is a function of $\bar{n}$ and a, and is defined in terms of $\mathcal{V}$. Since $\bar{n}$ and a are coarse-grained variables, a system having $n(\mathbf{r}) = n_{eq}^{\text{bulk},c}(\mathbf{r})$ for the solid phase and $n(\mathbf{r}) = n_{eq}^{\text{bulk},l}(\mathbf{r}) = \bar{n}$ for the liquid phase can be described by the thermodynamics of bulk phases.

The value of a that minimizes $\Delta f_{\text{PFC}}^{\text{bulk}}(\bar{n}, a)$ for each $\bar{n}$ is denoted as a^*. Its value is set by the position of the maximum of the primary (first) peak of the two-body DCF in Fourier space, k_m, where $a^* \propto k_m^{-1}$ [45, 55]. Since the position of the primary peak in the two-body DCF is weakly dependent on $\bar{n}$ in the PFC model, the value of a^* remains essentially unchanged for all values of $\bar{n}$.

3.2 Thermodynamics for Bulk Phases

In this section, we review the thermodynamics for bulk liquid and crystalline phases. First, we consider the thermodynamics for a bulk liquid phase, i.e., $n(\mathbf{r}) = n_{eq}^{\text{bulk},l}(\mathbf{r}) = \bar{n}$, and provide definitions for the entropy, S^l, hydrostatic pressure, P^l, and chemical potential, μ_A^l, for the bulk liquid phase, where the superscript l denotes quantities associated with the liquid phase. Next, we consider the thermodynamics of a bulk crystalline phase, i.e., $n(\mathbf{r}) = n_{eq}^{\text{bulk},c}(\mathbf{r})$, which incorporates the description of a lattice with sites that contain either atoms or vacancies, as introduced by Larché and Cahn [56]. The definitions for the entropy, S^c, hydrostatic pressure, P^c, and two different chemical potentials, μ_A^c and μ_L^c, are provided for the bulk crystalline phase, where the superscript c denotes quantities associated with the crystalline phase.

3.2.1 Bulk Liquid Phase

The free energy of the PFC model is the Helmholtz free energy [45]. For the bulk liquid phase, the Helmholtz free energy is

$$F^l = F^l(\theta^l, \mathcal{V}^l, N_A^l), \tag{3.3}$$

where θ^l, $\mathcal{V}^l$, and N_A^l are the temperature, volume, and the number of atoms in the bulk liquid, respectively. The differential form of F^l is

$$dF^l = -S^l d\theta^l - P^l d\mathcal{V}^l + \mu_A^l dN_A^l \tag{3.4}$$

where

$$S^l \equiv -\left.\frac{\partial F^l}{\partial \theta^l}\right|_{\mathcal{V}^l, N_A^l}, \quad P^l \equiv -\left.\frac{\partial F^l}{\partial \mathcal{V}^l}\right|_{\theta^l, N_A^l}, \quad \mu_A^l \equiv \left.\frac{\partial F^l}{\partial N_A^l}\right|_{\theta^l, \mathcal{V}^l}. \tag{3.5}$$

The integrated form of Eq. (3.4) is

$$F^l(\theta^l, \mathcal{V}^l, N_A^l) = -P^l\mathcal{V}^l + \mu_A^l N_A^l \tag{3.6}$$

and the corresponding Gibbs-Duhem relation is

$$0 = S^l d\theta^l - \mathcal{V}^l dP^l + N_A^l d\mu_A^l. \tag{3.7}$$

Equations (3.6) and (3.7) will be used later to derive FEDs for the bulk liquid phase.

3.2.2 Bulk Crystalline Phase

For a bulk crystalline solid, a lattice is employed to represent the spatially periodic structure of a crystal, where each lattice site contains either an atom or a vacancy [56, 57]. For a one-component bulk crystalline phase, the total number of lattice sites, N_L^c, is related to the number of atoms, N_A^c, and vacancies, N_V^c, by

$$N_L^c = N_A^c + N_V^c. \tag{3.8}$$

As discussed in Voorhees and Johnson [57], any two of the three thermodynamic variables in Eq. (3.8) can be used to describe the thermodynamic state of a one-component crystal. In this work we consider the Helmholtz free energy as a function of N_A^c and N_L^c,

$$F^c = F^c(\theta^c, \mathcal{V}^c, N_A^c, N_L^c), \tag{3.9}$$

where θ^c and $\mathcal{V}^c$ are the temperature and the crystal volume, respectively. The differential form of F^c is

$$dF^c = -S^c d\theta^c - P^c d\mathcal{V}^c + \mu_A^c dN_A^c + \mu_L^c dN_L^c \tag{3.10}$$

where

$$S^c \equiv -\frac{\partial F^c}{\partial \theta^c}\bigg|_{\mathcal{V}^c, N_A^c, N_L^c}, \quad P^c \equiv -\frac{\partial F^c}{\partial \mathcal{V}^c}\bigg|_{\theta^c, N_A^c, N_L^c}, \quad \mu_A^c \equiv \frac{\partial F^c}{\partial N_A^c}\bigg|_{\theta^c, \mathcal{V}^c, N_L^c}, \quad \mu_L^c \equiv \frac{\partial F^c}{\partial N_L^c}\bigg|_{\theta^c, \mathcal{V}^c, N_A^c}. \tag{3.11}$$

The partial derivative that defines μ_A^c provides the energy change due to the addition or removal of an atom while the number of lattice sites and crystal volume are held constant for an isothermal system. The definition of μ_A^c requires a vacancy to be eliminated when an atom is added to the crystal and a vacancy to be generated when an atom is removed from the crystal. This chemical potential is hereafter referred to as the diffusion potential [57] to distinguish from the chemical potential of atoms for the bulk liquid phase. On the other hand, the partial derivative that defines μ_L^c provides the energy change due to a change in the number of lattice sites while the crystal volume and the number of atoms are held constant for an isothermal system. A lattice site can be added by moving an atom within the crystal to the surface while simultaneously creating a vacancy within the crystal. This process will cause an increase in the pressure when the crystal volume is held constant and the partial molar volume of the vacancy is nonzero [57].

The integrated form of Eq. (3.10) is

$$F^c(\theta^c, \mathcal{V}^c, N_A^c, N_L^c) = -P^c\mathcal{V}^c + \mu_A^c N_A^c + \mu_L^c N_L^c \tag{3.12}$$

and the corresponding Gibbs-Duhem relation is

$$0 = S^c d\theta^c - \mathcal{V}^c dP^c + N_A^c d\mu_A^c + N_L^c d\mu_L^c, \tag{3.13}$$

the derivation of which is presented in Appendix A. Equations (3.12) and (3.13) will be used later to derive FEDs for a bulk crystalline phase.

3.3 Free-Energy Densities for Bulk Phases

In this section, we derive FEDs that are defined on a reference (undeformed) volume, $\mathcal{V}'$, and the (potentially deformed) system volumes, $\mathcal{V}^l$ and $\mathcal{V}^c$, for the bulk liquid and crystalline phases, respectively. FEDs defined on $\mathcal{V}'$ are referred to as reference-volume FEDs, while those defined on $\mathcal{V}^l$ or $\mathcal{V}^c$ are referred to as system-volume FEDs. By defining the reference-volume FED for the bulk crystalline phase, we make an important distinction between two sources of pressure change: mechanical and configurational forces [57]. The system-volume FEDs are used to develop a thermodynamic relationship between the PFC FED and thermodynamic state variables.

3.3.1 Bulk Liquid Phase

The reference-volume FED for the bulk liquid phase, denoted as $f^l_{\mathcal{V}'}$, is obtained by dividing F^l by $\mathcal{V}'$,

$$f^l_{\mathcal{V}'} \equiv \frac{F^l}{\mathcal{V}'} = -P^l J^l + \mu^l_A \rho'^l_A, \tag{3.14}$$

where

$$J^l \equiv \frac{\mathcal{V}^l}{\mathcal{V}'}, \quad \rho'^l_A \equiv \frac{N^l_A}{\mathcal{V}'}. \tag{3.15}$$

The variable J^l describes volume change due to hydrostatic pressure and ρ'^l_A is the atomic density of the liquid phase defined on $\mathcal{V}'$, as denoted by the prime symbol. Similarly, the Gibbs-Duhem relation in Eq. (3.7) is divided by $\mathcal{V}'$ to obtain

$$0 = s^l_{\mathcal{V}'} d\theta^l - J^l dP^l + \rho'^l_A d\mu^l_A, \tag{3.16}$$

where $s^l_{\mathcal{V}'} \equiv S^l/\mathcal{V}'$. Differentiating Eq. (3.14) and subtracting Eq. (3.16) gives an expression for $df^l_{\mathcal{V}'}$,

$$df^l_{\mathcal{V}'} = -s^l_{\mathcal{V}'} d\theta^l - P dJ^l + \mu^l_A d\rho'^l_A, \tag{3.17}$$

where $f^l_{\mathcal{V}'}$ is a function of natural variables θ^l, J^l, and ρ'^l_A.

Alternatively, the system-volume FED for the bulk liquid phase, as denoted by $f^l_{\mathcal{V}}$, is obtained by dividing F^l by $\mathcal{V}^l$,

$$f^l_{\mathcal{V}} \equiv \frac{F^l}{\mathcal{V}^l} = -P^l + \mu^l_A \rho^l_A, \tag{3.18}$$

where $\rho^l_A \equiv N^l_A/\mathcal{V}^l$. Similarly, the Gibbs-Duhem relation in Eq. (3.7) is divided by $\mathcal{V}^l$ to obtain

$$0 = s^l_{\mathcal{V}} d\theta^l - dP^l + \rho^l_A d\mu^l_A, \tag{3.19}$$

where $s^l_{\mathcal{V}} \equiv S^l/\mathcal{V}^l$. The variables $s^l_{\mathcal{V}}$ and ρ^l_A are defined on the system volume of the bulk liquid phase, $\mathcal{V}^l$. Differentiating Eq. (3.18) and subtracting Eq. (3.19) gives a relationship for $df^l_{\mathcal{V}}$,

$$df^l_{\mathcal{V}} = -s^l_{\mathcal{V}} d\theta^l + \mu^l_A d\rho^l_A, \tag{3.20}$$

where $f^l_{\mathcal{V}}$ is a function of natural variables θ^l and ρ^l_A. Equation (3.20) is defined in terms of the system volume of the liquid phase and is a function of ρ^l_A, which is related to $\bar{n}$ of the PFC FED for a bulk liquid via $\bar{n} = \rho^l_A/\rho_0 - 1$. Therefore, Eq. (3.20) will be employed to develop a thermodynamic interpretation of the PFC free energy for the bulk liquid phase.

3.3.2 Bulk Crystalline Phase

The reference-volume FED for the bulk crystalline phase, denoted as $f^c_{\mathcal{V}'}$, is determined by dividing F^c with $\mathcal{V}'$,

$$f^c_{\mathcal{V}'} \equiv \frac{F^c}{\mathcal{V}'} = -P^c J^c + \mu^c_A \rho'^c_A + \mu^c_L \rho'^c_L, \tag{3.21}$$

where

$$J^c \equiv \frac{\mathcal{V}^c}{\mathcal{V}'}, \quad \rho'^c_A \equiv \frac{N^c_A}{\mathcal{V}'}, \quad \rho'^c_L \equiv \frac{N^c_L}{\mathcal{V}'}. \tag{3.22}$$

Similar to the bulk liquid phase, J^c describes volume change due to hydrostatic pressure in a bulk crystalline phase, and $\rho_A'^c$ and $\rho_L'^c$ are the atomic and lattice densities, respectively, that are defined on the reference volume. The Gibbs-Duhem relation in Eq. (3.13) is divided by $\mathcal{V}'$ to obtain

$$0 = s^c_{\mathcal{V}'} d\theta^c - J^c dP^c + \rho_A'^c d\mu_A^c + \rho_L'^c d\mu_L^c, \tag{3.23}$$

where $s^c_{\mathcal{V}'} \equiv S^c/\mathcal{V}'$. Differentiating Eq. (3.21) and subtracting Eq. (3.23) gives an expression for $df^c_{\mathcal{V}'}$,

$$df^c_{\mathcal{V}'} = -s^c_{\mathcal{V}'} d\theta^c - P^c dJ^c + \mu_A^c d\rho_A'^c + \mu_L^c d\rho_L'^c, \tag{3.24}$$

where $f^c_{\mathcal{V}'}$ is a function of natural variables θ^c, J^c, $\rho_A'^c$, and $\rho_L'^c$.

Changing the volume of an isothermal bulk crystalline system (reflected by a change in J^c because $\mathcal{V}'$ is constant) while keeping the mass constant (equivalent to fixing $\rho_A'^c$) will cause the pressure to change. This pressure change arises from deforming the system with a *mechanical force*. Alternatively, as mentioned earlier, a pressure change also arises when the number of lattice sites change when $\rho_L'^c$ is adjusted and the crystal volume is constant. To understand this latter type of pressure change, consider a thought experiment where a crystal is enclosed by a rigid wall where $\mathcal{V}^c$ is fixed ($\mathcal{V}^c = \mathcal{V}'$). When a lattice site is added to the system, the constraint imposed by the rigid walls prevent a volume change, resulting in a pressure change. This type of pressure change arises from a *configurational force* [57]. Therefore, the thermodynamic framework for crystalline solids described above allows us to distinguish between pressure changes due to mechanical and configurational forces [1].

As mentioned earlier, the PFC FED is defined on the system volume. Therefore, a

---

[1] The thermodynamic framework for a crystal has also been used to distinguish between volume change due to configurational and mechanical forces [57].

system-volume FED for a bulk crystalline phase will be most appropriate for developing a thermodynamic relationship for the PFC model of a bulk crystal. To reformulate the reference-volume FED, Eq. (3.21), and Eq. (3.23) in terms of the system volume, we divide both sides of the equations by J^c (see Eq. (3.22) for definition):

$$\mathbb{f}^c_{\mathcal{V}} \equiv \frac{f^c_{\mathcal{V}'}}{J^c} = -P^c + \mu^c_A \frac{\rho'^c_A}{J^c} + \mu^c_L \frac{\rho'^c_L}{J^c} \tag{3.25}$$

and

$$0 = \frac{s^c_{\mathcal{V}'}}{J^c} d\theta^c - dP^c + \frac{\rho'^c_A}{J^c} d\mu^c_A + \frac{\rho'^c_L}{J^c} d\mu^c_L, \tag{3.26}$$

where $\mathbb{f}^c_{\mathcal{V}}$ is one expression for the system-volume FED. The division by J^c above maps ρ'^c_A, ρ'^c_L, and $s^c_{\mathcal{V}'}$ to their system-volume counterparts: ρ^c_A, ρ^c_L, and $s^c_{\mathcal{V}}$, respectively. The differential form of Eq. (3.25) is obtained by taking its derivative and subtracting Eq. (3.26),

$$d\mathbb{f}^c_{\mathcal{V}} = -\frac{s^c_{\mathcal{V}'}}{J^c} d\theta^c + \frac{\mu^c_A}{J^c} d\rho'^c_A + \frac{\mu^c_L}{J^c} d\rho'^c_L + \left(\mu^c_A \rho'^c_A + \mu^c_L \rho'^c_L\right) d(1/J^c), \tag{3.27}$$

where it can now be observed that $\mathbb{f}^c_{\mathcal{V}}$ is a function of natural variables θ^c, ρ'^c_A, ρ'^c_L, and $1/J^c$. Therefore, the FED denoted by $\mathbb{f}^c_{\mathcal{V}}$ is a system-volume FED that is a function of densities defined on the reference volume.

In order to obtain a FED with independent variables that match those of the PFC FED, the variables ρ'^c_A and ρ'^c_L are related to ρ^c_A and ρ^c_L by the chain rule

$$d\rho'^c_A = d(\rho^c_A J^c) = J^c d\rho^c_A + \rho^c_A dJ^c \quad \text{and} \quad d\rho'^c_L = d(\rho^c_L J^c) = J^c d\rho^c_L + \rho^c_L dJ^c. \tag{3.28}$$

Substituting Eq. (3.28) into Eq. (3.27), one obtains

$$\begin{aligned}
df^c_{\mathcal{V}} &= -\frac{s^c_{\mathcal{V}'}}{J^c}d\theta^c + \frac{\mu^c_A}{J^c}\left(J^c d\rho^c_A + \rho^c_A dJ^c\right) + \frac{\mu^c_L}{J^c}\left(J^c d\rho^c_L + \rho^c_L dJ^c\right) + \left(\mu^c_A \rho'^c_A + \mu^c_L \rho'^c_L\right) d(1/J^c) \\
&= -\frac{s^c_{\mathcal{V}'}}{J^c}d\theta^c + \mu^c_A d\rho^c_A + \mu^c_L d\rho^c_L + \left(\frac{\rho^c_A \mu^c_A}{J^c} + \frac{\rho^c_L \mu^c_L}{J^c}\right) dJ^c + \left(\mu^c_A \rho'^c_A + \mu^c_L \rho'^c_L\right) d(1/J^c) \\
&= -\frac{s^c_{\mathcal{V}'}}{J^c}d\theta^c + \mu^c_A d\rho^c_A + \mu^c_L d\rho^c_L + \left(\mu^c_A \rho'^c_A + \mu^c_L \rho'^c_L - \mu^c_A J^c \rho^c_A - \mu^c_L J^c \rho^c_L\right) d(1/J^c) \\
&= -s^c_{\mathcal{V}} d\theta^c + \mu^c_A d\rho^c_A + \mu^c_L d\rho^c_L, \qquad (3.29)
\end{aligned}$$

where we have used the relationships

$$dJ^c = -(J^c)^2 d(1/J^c) \quad \text{and} \quad s^c_{\mathcal{V}} = \frac{s^c_{\mathcal{V}'}}{J^c}. \qquad (3.30)$$

The same expression can be obtained by starting from a FED based on the system volume; however, we derive it in this manner to explicitly illustrate the connection between reference-volume and system-volume variables. This expression of the system-volume FED for the bulk crystal, $f^c_{\mathcal{V}}$, given in Eq. (3.29) is now a function of natural variables θ^c, ρ^c_A, and ρ^c_L. By expressing ρ^c_L in terms of the volume of a lattice site, $\mathcal{V}^c_L$,

$$\rho^c_L = \frac{1}{\mathcal{V}^c_L}, \qquad (3.31)$$

Eq. (3.29) is related to the lattice spacing via the unit-cell volume, $\mathcal{V}^c_C$, which is written in terms of $\mathcal{V}^c_L$ using the number of lattice sites per unit cell, $\chi^c \equiv \mathcal{V}^c_C/\mathcal{V}^c_L$. The value of χ^c depends on the lattice structure. For example, a *bcc* structure, which contains 2 lattice sites per unit cell, has $\chi^c = 2$.

Equation (3.31) is used to express $df^c_{\mathcal{V}}$ as

$$df^c_{\mathcal{V}} = -s^c_{\mathcal{V}} d\theta^c + \mu^c_A d\rho^c_A + \chi^c \mu^c_L d(1/\mathcal{V}^c_C), \qquad (3.32)$$

where $f^c_{\mathcal{V}}$ is a function of natural variables θ^c, ρ^c_A, and $1/\mathcal{V}^c_C$. Since $\mathcal{V}^c_C$ is a sole function of a (e.g., for a *bcc* structure, $\mathcal{V}_C^c = a^3$), the FED representation in Eq. (3.32) is a function of natural variables that correspond to those of the PFC FED of the bulk crystal. Therefore, Eq. (3.32) is employed in developing a thermodynamic interpretation of the PFC free energy for a bulk crystalline phase. The integrated form of Eq. (3.32) is derived from Eqs. (3.25) and (3.31) to be

$$f_{\mathcal{V}}^c = -P^c + \mu_A^c \rho_A^c + \frac{\chi^c \mu_L^c}{\mathcal{V}_C^c}, \tag{3.33}$$

and Eqs. (3.28) and (3.31) are substituted into Eq. (3.26) to obtain

$$0 = -s_{\mathcal{V}}^c d\theta^c - dP^c + \rho_A^c d\mu_A^c + \frac{\chi^c}{\mathcal{V}_C^c} d\mu_L^c. \tag{3.34}$$

The expressions in Eqs. (3.32) and (3.33) form the basis for deriving a thermodynamic relationship for a bulk crystalline phase in the PFC model.

As observed from Eq. (3.32), $\mu_A^c = \partial f_{\mathcal{V}}^c / \partial \rho_A^c |_{\theta^c, \mathcal{V}_C^c}$ and thus changing ρ_A^c while holding $\mathcal{V}_C^c$ and θ^c constant is equivalent to changing the number of atoms while the number of lattice sites is held constant. A negative value of μ_A^c indicates the presence of a driving force for adding an atom into a vacant lattice site. On the other hand, a positive value of μ_A^c indicates the presence of a driving force for removing an atom from an occupied lattice site. Additionally, it can be observed that $\chi^c \mu_L^c = \partial f_{\mathcal{V}}^c / \partial (1/\mathcal{V}_C^c) |_{\theta^c, \rho_A^c}$ and thus changing $\mathcal{V}_C^c$ (equivalent to changing lattice spacing) while holding ρ_A^c and θ^c constant is equivalent to changing the number of lattice sites while the crystal volume is held constant. Therefore, the process of changing $\mathcal{V}_C^c$ while holding ρ_A^c constant gives rise to a configurational force, just as in the case for changing the number of lattice sites as indicated in Eq. (3.11). This point will be further examined in the next section after the FED in Eq. (3.32) is linked to the PFC FED.

3.4 Thermodynamic Relationship for the Phase-Field Crystal Model

In this section, we use the system-volume FEDs derived in the previous section to develop the relationship of the PFC FED to thermodynamic state variables for the bulk liquid and crystalline phases.

3.4.1 Bulk Liquid Phase

Since the PFC model is based on a free-energy difference from a reference liquid phase, the PFC FED of a bulk liquid phase is related to $f_{\mathcal{V}}^{l}$ in Eq. (3.18) by

$$\Delta f_{\text{PFC}}^{\text{bulk},l}(\bar{n}) = f_{\mathcal{V}}^{l} - f^{0}, \tag{3.35}$$

where f^0 is the Helmholtz FED of the reference liquid phase with a density of ρ_0. Note that f^0 remains constant as $\bar{n}$ changes because the two-body DCF is taken at the reference state and is assumed to be independent of $\bar{n}$. Furthermore, $\bar{n}$ is related to ρ_A^l of Eq. (3.18) by

$$\rho_A^l = \bar{n}\rho_0 + \rho_0. \tag{3.36}$$

Equations (3.35) and (3.36) are combined with Eq. (3.18) to obtain

$$\Delta f_{\text{PFC}}^{\text{bulk},l}(\bar{n}) \equiv f_{\mathcal{V}}^{l} - f^{0} = -P^{l} + \rho_0 \mu_A^l \left(\bar{n} + 1\right) - f^{0}. \tag{3.37}$$

Similarly, Eq. (3.36) is combined with Eq. (3.19) to obtain

$$0 = s_{\mathcal{V}}^{l} d\theta^{l} - dP^{l} + \rho_0(\bar{n}+1)d\mu_A^l. \tag{3.38}$$

Differentiating Eq. (3.37) and subtracting Eq. (3.38) gives an expression for

$d(\Delta f_{\mathrm{PFC}}^{\mathrm{bulk},l}(\bar{n}))$,

$$d(\Delta f_{\mathrm{PFC}}^{\mathrm{bulk},l}(\bar{n})) \equiv d\left(f_{\mathcal{V}}^{l} - f^{0}\right) = -s_{\mathcal{V}}^{l} d\theta^{l} + \rho_0 \mu_A^{l} d\bar{n}. \tag{3.39}$$

It is important to note that the PFC model derived from cDFT in Ref. [45] applies to isothermal systems, and thus $d\theta^l$ in Eq. (3.39) is zero. The EOF-PFC model follows the same approach, and thus $d\theta^l = 0$. However, a recent formulation, called the structural PFC model, has phenomenologically extended the PFC model to account for temperature change via a change of peak height in the two-body DCF [55]. Therefore, for the XPFC model, $d\theta^l$ is related to the peak height of the two-body DCF.

3.4.2 Bulk Crystalline Phase

The PFC FED of a bulk crystalline phase is related to $f_{\mathcal{V}}^{c}$ in Eq. (3.33) by

$$\Delta f_{\mathrm{PFC}}^{\mathrm{bulk},c}(\bar{n}, a) = f_{\mathcal{V}}^{c} - f^{0}, \tag{3.40}$$

and $\bar{n}$ is related to ρ_A^c of Eq. (3.33) by

$$\rho_A^c = \bar{n}\rho_0 + \rho_0. \tag{3.41}$$

Equations (3.40) and (3.41) are combined with Eq. (3.33) to obtain

$$\Delta f_{\mathrm{PFC}}^{\mathrm{bulk},c}(\bar{n}, a) \equiv f_{\mathcal{V}}^{c} - f^{0} = -P^{c} + \rho_0 \mu_A^{c}\left(\bar{n} + 1\right) + \frac{\chi^{c}\mu_L^{c}}{\mathcal{V}_C^{c}} - f^{0}. \tag{3.42}$$

Similarly, Eq. (3.41) is combined with Eq. (3.34) to obtain

$$0 = -s_{\mathcal{V}}^{c} d\theta^{c} - dP^{c} + \rho_0(\bar{n} + 1) d\mu_A^{c} + \frac{\chi^{c}}{\mathcal{V}_C^{c}} d\mu_L^{c}. \tag{3.43}$$

Differentiating Eq. (3.42) and subtracting Eq. (3.43) gives an expression for

$d(\Delta f_{\mathrm{PFC}}^{\mathrm{bulk},c}(\bar{n},a))$,

$$d(\Delta f_{\mathrm{PFC}}^{\mathrm{bulk},c}(\bar{n},a)) \equiv d\left(f_{\mathcal{V}}^{c} - f^{0}\right) = -s_{\mathcal{V}}^{c} d\theta^{c} + \rho_0 \mu_A^c d\bar{n} + \chi^c \mu_L^c d(1/\mathcal{V}_C^c), \tag{3.44}$$

where $\mathcal{V}_C^c$ is a function of a. As mentioned earlier, the EOF-PFC model we consider in this work is formulated for isothermal systems and thus $d\theta^c = 0$.

Equation (3.44) is central to this work because it links the PFC FED to μ_A^c and μ_V^c, which are chemical potentials that correspond to different thermodynamic processes. As seen in Eq. (3.44), $\mu_A^c = 1/\rho_0(\partial \Delta f_{\mathrm{PFC}}^{\mathrm{bulk},c}/\partial \bar{n}|_{\theta^c,\mathcal{V}_C^c})$ and therefore varying $\bar{n}$ when the temperature and lattice spacing are held constant in the PFC model is equivalent to changing the number of atoms while θ^c, $\mathcal{V}^c$, and N_L^c are fixed. Similarly, since $\mu_V^c = 1/\chi^c(\partial \Delta f_{\mathrm{PFC}}^{\mathrm{bulk},c}/\partial(1/\mathcal{V}_C^c)|_{\theta^c,\bar{n}})$, varying lattice spacing when temperature and $\bar{n}$ are held constant in the PFC model is equivalent to changing the number of lattice sites while θ^c, $\mathcal{V}^c$, and N_A^c are fixed.

As discussed earlier, the addition or removal of lattice sites while the crystal volume is held constant gives rise to a pressure change due to a configurational force. This point has not previously been elucidated, and the resulting pressure has been instead attributed to pressure change due to mechanical forces, leading to an improper procedure for elastic constant calculations with the PFC model [24, 58, 62]. A thermodynamically consistent procedure for calculating elastic constants [53] was developed in our previous work, and the framework above further validates our approach.

3.5 Solid-Liquid Phase Coexistence in the PFC Model

In this section, we apply the thermodynamic relationship developed in the previous section to derive a procedure for determining solid-liquid phase coexistence in the PFC model. First, we describe the equilibrium conditions presented in Voorhees and Johnson [57] between bulk crystalline and liquid phases, which involve constraints on

P, μ_A, and μ_L^c. These equilibrium conditions are then imposed on the thermodynamic relationship for the PFC model, Eqs. (3.39) and (3.44), to obtain a thermodynamically consistent procedure for determining solid-liquid phase coexistence.

3.5.1 Solid-Liquid Phase Coexistence in the Phase-Field Crystal Model

As described in Voorhees and Johnson [57], a bulk crystalline and liquid phase are in equilibrium when the variation in the total energy of a system vanishes. They showed that the variation in the system energy vanishes when thermal, mechanical, and chemical equilibria are achieved. For a one-component bulk crystalline phase in equilibrium with a bulk liquid phase, the equilibrium conditions are

$$\theta^c = \theta^l, \quad P^c = P^l, \quad \mu_A^c = \mu_A^l, \quad \mu_L^c = 0. \tag{3.45}$$

The last condition of $\mu_L^c = 0$ is unique to crystalline solids and indicates that there is no driving force for an addition or removal of a lattice site. This condition can be used to calculate equilibrium vacancy concentration [57].

The condition for thermal equilibrium is met when considering an isothermal system. Furthermore, $\mu_L^c = 0$ when the FED of the bulk crystalline phase, $\Delta f_{\text{PFC}}^{\text{bulk},c}(\bar{n}, a)$, is relaxed with respect to the lattice spacing while $\bar{n}$ and θ^c are held constant (see Eq. (3.44)). Therefore, the task of finding solid-liquid coexistence lies in satisfying the equilibrium conditions, $P^c = P^l$ and $\mu_A^c = \mu_A^l$.

A relationship for pressure is obtained by rearranging the expressions for the PFC FEDs in Eqs. (3.37) and (3.42):

$$-P^l = \Delta f_{\text{PFC}}^{\text{bulk},l}(\bar{n}) - \rho_0 \mu_A^l (\bar{n}+1) + f_0 \text{ and } -P^c = \Delta f_{\text{PFC}}^{\text{bulk},c}(\bar{n}, a) - \rho_0 \mu_A^c (\bar{n}+1) - \frac{\chi^c \mu_L^c}{\mathcal{V}_C^c} + f_0, \tag{3.46}$$

respectively, where the determination of P^l and P^c require a knowledge of f^0. However, since both the liquid and solid phases have the same reference state, f^0 will cancel when equating their pressures. By using

$$\rho_0 \mu_A^l = \left. \frac{\partial \Delta f_{\mathrm{PFC}}^{\mathrm{bulk},l}}{\partial \bar{n}} \right|_{\theta^l} \tag{3.47}$$

obtained from Eq. (3.39), P^l in terms of $\Delta f_{\mathrm{PFC}}^{\mathrm{bulk},l}(\bar{n})$ and $\bar{n}$ is expressed as

$$\begin{aligned} -P^l &= \Delta f_{\mathrm{PFC}}^{\mathrm{bulk},l}(\bar{n}) - \left. \frac{\partial \Delta f_{\mathrm{PFC}}^{\mathrm{bulk},l}}{\partial \bar{n}} \right|_{\theta^l} (\bar{n}+1) + f_0 \\ &= \mathcal{Y}^l - \mathcal{S}^l + f_0 \end{aligned} \tag{3.48}$$

where

$$\mathcal{Y}^l \equiv \Delta f_{\mathrm{PFC}}^{\mathrm{bulk},l}(\bar{n}) - \mathcal{S}^l \bar{n} \quad \text{and} \quad \mathcal{S}^l \equiv \left. \frac{\partial \Delta f_{\mathrm{PFC}}^{\mathrm{bulk},l}}{\partial \bar{n}} \right|_{\theta^l} \tag{3.49}$$

are the y-intercept and slope of a $\Delta f_{\mathrm{PFC}}^{\mathrm{bulk},l}(\bar{n})$ vs. $\bar{n}$ curve, respectively, when θ^l is constant. A schematic of Eq. (3.49) is shown in Fig. 3.1.

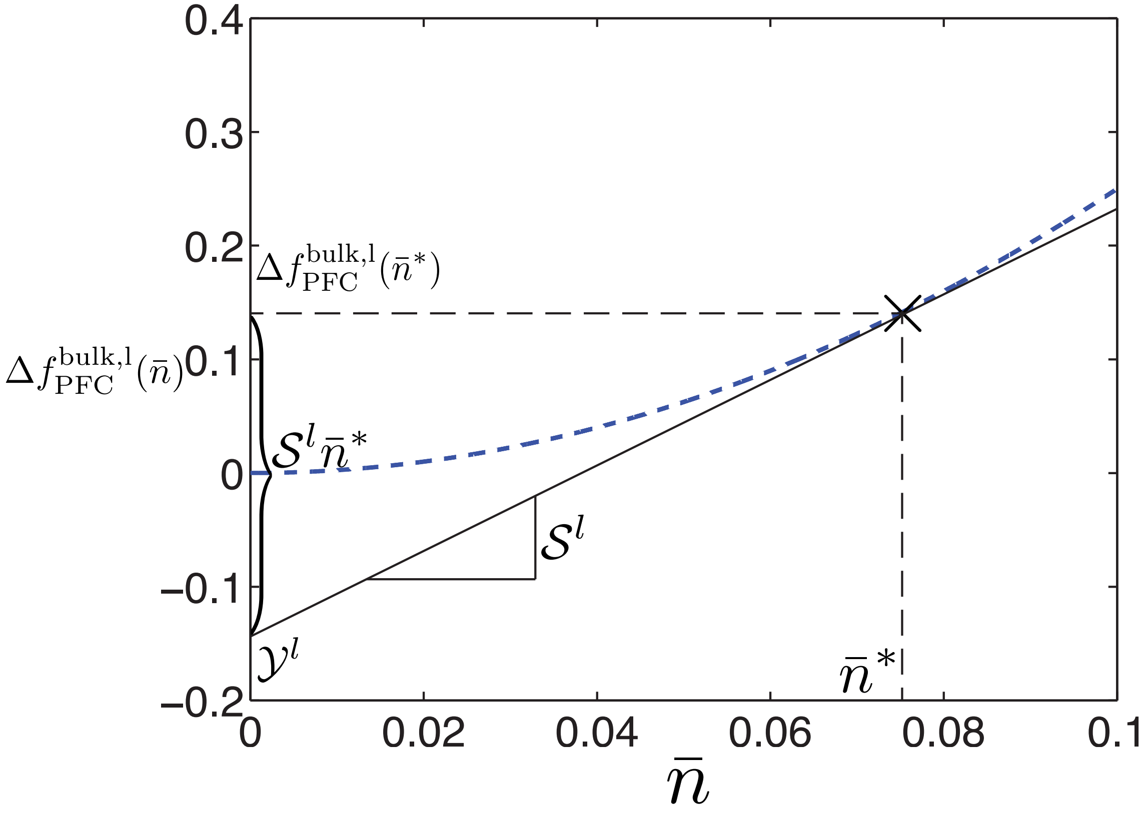

Figure 3.1: Schematic of Eq. (3.49) on a liquid FED curve (dashed line) with tangent line (solid line) at the point $\bar{n} = \bar{n}^*$, which is marked with "×". The schematic for Eq. (3.52) is similar, but for the FED curve of a bulk crystalline phase.

Similarly, by using

$$\rho_0 \mu_A^c = \left.\frac{\partial \Delta f_{\mathrm{PFC}}^{\mathrm{bulk},c}}{\partial \bar{n}}\right|_{\theta^c, \mu_L^c} \tag{3.50}$$

obtained from Eq. (3.44), P^c in terms of $\Delta f_{\mathrm{PFC}}^{\mathrm{bulk},c}(\bar{n}, a)$ and $\bar{n}$ is expressed as

$$\begin{aligned} -P^c &= \Delta f_{\mathrm{PFC}}^{\mathrm{bulk},c}(\bar{n}, a) - \left.\frac{\partial \Delta f_{\mathrm{PFC}}^{\mathrm{bulk},c}}{\partial \bar{n}}\right|_{\theta^c, \mu_L^c} (\bar{n}+1) - \frac{\chi^c \mu_L^c}{\mathcal{V}_C^c} + f_0 \\ &= \mathcal{Y}^c - \mathcal{S}^c - \frac{\chi^c \mu_L^c}{\mathcal{V}_C^c} + f_0, \end{aligned} \tag{3.51}$$

where

$$\mathcal{Y}^c \equiv \Delta f_{\mathrm{PFC}}^{\mathrm{bulk},c}(\bar{n}, a) - \mathcal{S}^c \bar{n}, \quad \text{and} \quad \mathcal{S}^c \equiv \left.\frac{\partial \Delta f_{\mathrm{PFC}}^{\mathrm{bulk},c}}{\partial \bar{n}}\right|_{\theta^c, \mu_L^c} \tag{3.52}$$

are the y-intercept and slope of a $\Delta f_{\mathrm{PFC}}^{\mathrm{bulk},c}$ vs. $\bar{n}$ curve, respectively, when μ_L^c and θ^c are constant. Note that the condition $\mu_L^c = 0$ has not been imposed in Eq. (3.51), but will be applied later to fulfill the equilibrium conditions listed in Eq. (3.45).

According to Eqs. (3.48) and (3.51), mechanical equilibrium for solid-liquid phase coexistence is fulfilled when $\mathcal{Y}^c = \mathcal{Y}^l$, $\mathcal{S}^c = \mathcal{S}^l$, and $\mu_L^c = 0$. Furthermore, the condition, $\mu_A^c = \mu_A^l$, for chemical equilibrium is also satisfied when $\mathcal{S}^c = \mathcal{S}^l$. Therefore, satisfying the common-tangent condition (i.e., the y-intercept and slope of the two curves are equal) for the $\Delta f_{\mathrm{PFC}}^{\mathrm{bulk},c}$ vs. $\bar{n}$ and $f_{\mathrm{PFC}}^{\mathrm{bulk},l}(\bar{n})$ vs. $\bar{n}$ curves with $\mu_L^c = 0$ fulfills the equilibrium conditions for solid-liquid phase coexistence. This procedure, which involves thermal, mechanical, and chemical equilibria, is in agreement with the common-tangent construction commonly used for calculating solid-liquid phase coexistence in the PFC model [24, 58, 66]. Therefore, the above analysis justifies the use of the common-tangent construction to determine solid-liquid phase coexistence in the PFC model.

As noted earlier, the condition of $\mu_L^c = 0$ is accomplished in the PFC model by minimizing the PFC FED for the bulk crystalline phase with respect to $\mathcal{V}_C^c$ while θ^c and $\bar{n}$ are held constant, as seen in Eq. (3.44). Therefore, the minimization of the density profile according to the PFC FED with respect to lattice spacing for a crystalline solid, which is conventionally done in the PFC model [66], is a necessary step for obtaining the state in which $\mu_L^c = 0$ and for determining solid-liquid phase coexistence.

3.6 Application to EOF-PFC Model

In this section, we apply the thermodynamic relationships for the PFC model developed in the previous section to the EOF-PFC model (see Section 2.2.3) to demonstrate the procedure for determining phase coexistence, as well as to develop physical intuition about the PFC input parameters.

3.6.1 Free-Energy Density Curves and Phase Coexistence for *bcc* Fe

We calculate the solid and liquid FED curves for the EOF-PFC model with the fitting parameters of Ref. [54], which are listed in Table 2.1. The dimensionless PFC FED for the solid and liquid phases are plotted as functions of $\bar{n}$ in Fig. 3.2.

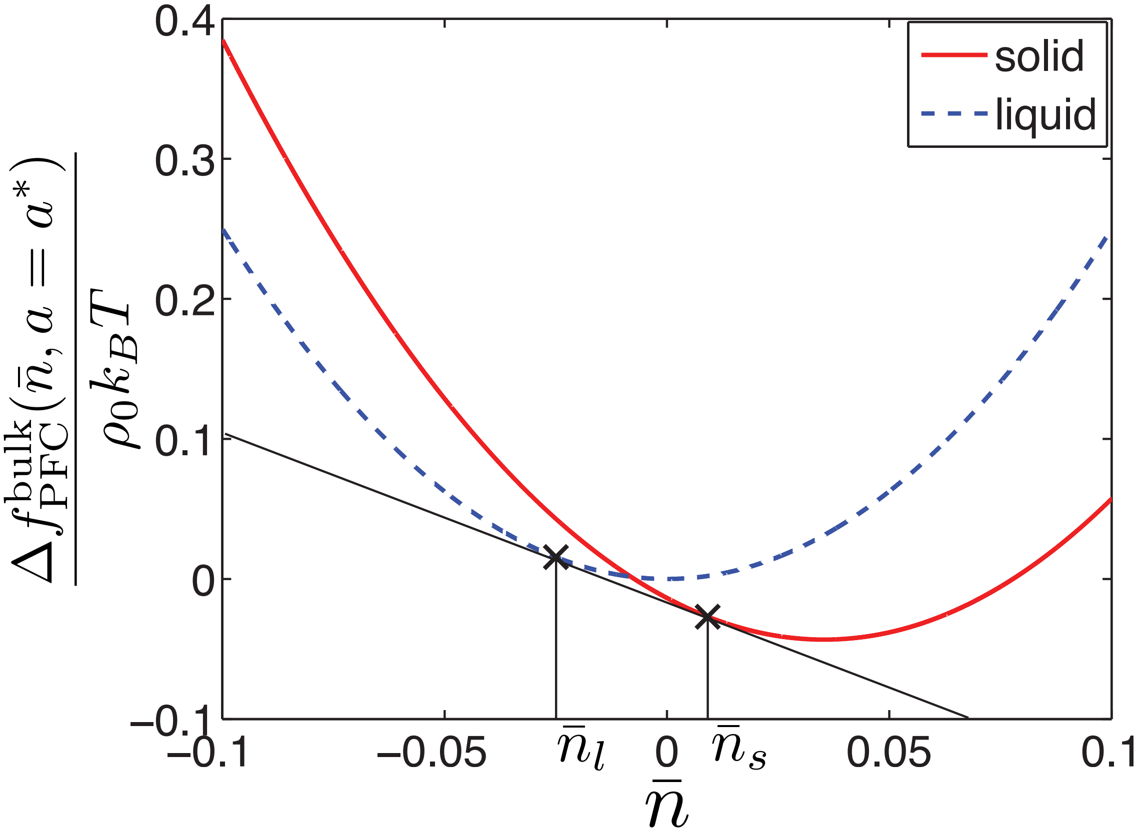

Figure 3.2: Plot of the dimensionless PFC FEDs of the EOF-PFC model for the solid (solid red line) and liquid (dashed blue line) phases as a function of $\bar{n}$. Each point on the solid FED curve is minimized with respect to lattice spacing, and thus satisfies $\mu^c_L = 0$. The dimensionless coexistence number density for the solid, $\bar{n}_s$, and liquid, $\bar{n}_l$, phases are marked with "×" marks.

The equilibrium FED for each value of $\bar{n}$ was calculated by relaxing a one-mode approximation of *bcc* Fe according to the PFC FED via Eq. (3.1), as done in Ref. [66]. Each point in the solid FED curve of Fig. 3.2 satisfies $\mu_L^c = 0$, which is achieved by minimizing the PFC FED with respect to lattice spacing. As described in Section 3.1, the value of a that minimizes the PFC FED, denoted as a^*, remains constant because the position of the primary peak in the two-body DCF of the PFC model is assumed to be independent of $\bar{n}$. For the calculations in Fig. 3.2, $a^* = 2.978\mathring{A}$ for all values of $\bar{n}$.

The scaled dimensionless coexistence number densities for the solid, $\bar{n}_s$, and liquid, $\bar{n}_l$, phases were determined with a common-tangent construction on the FED curves in Fig. 3.2. The values for solid and liquid coexistence densities are $\bar{n}_s = 9.17 \times 10^{-3}$ and $\bar{n}_l = -2.49 \times 10^{-2}$, respectively. These values are in agreement with those presented in Ref. [54].

3.6.2 Diffusion Potential

Figure 3.3 shows the diffusion potential calculated from Eq. (3.50) for the single-phase solid region of the EOF-PFC model, $\bar{n} > \bar{n}_s$. As can be observed, μ_A^c transitions from a negative to a positive value at $\bar{n} = 3.54 \times 10^{-2}$. As described earlier, μ_A^c represents the energy change due to the addition or removal of atoms in an isothermal system when the number of lattice sites and the crystal volume are held constant. When $\mu_A^c < 0$ (left of dashed vertical line in Fig. 3.3), there is a driving force for adding an atom into a vacant lattice site, which decreases as $\bar{n}$ increases. On the other hand, when $\mu_A^c > 0$ (right of dashed vertical line in Fig. 3.3), there is a driving force for removing an atom from an occupied lattice site, which decreases as $\bar{n}$ decreases. When $\mu_A^c = 0$, there is no driving force for adding or removing atoms to and from lattice sites, and the condition $\mu_L^c = 0$ allows us to determine the single-phase equilibrium vacancy density.

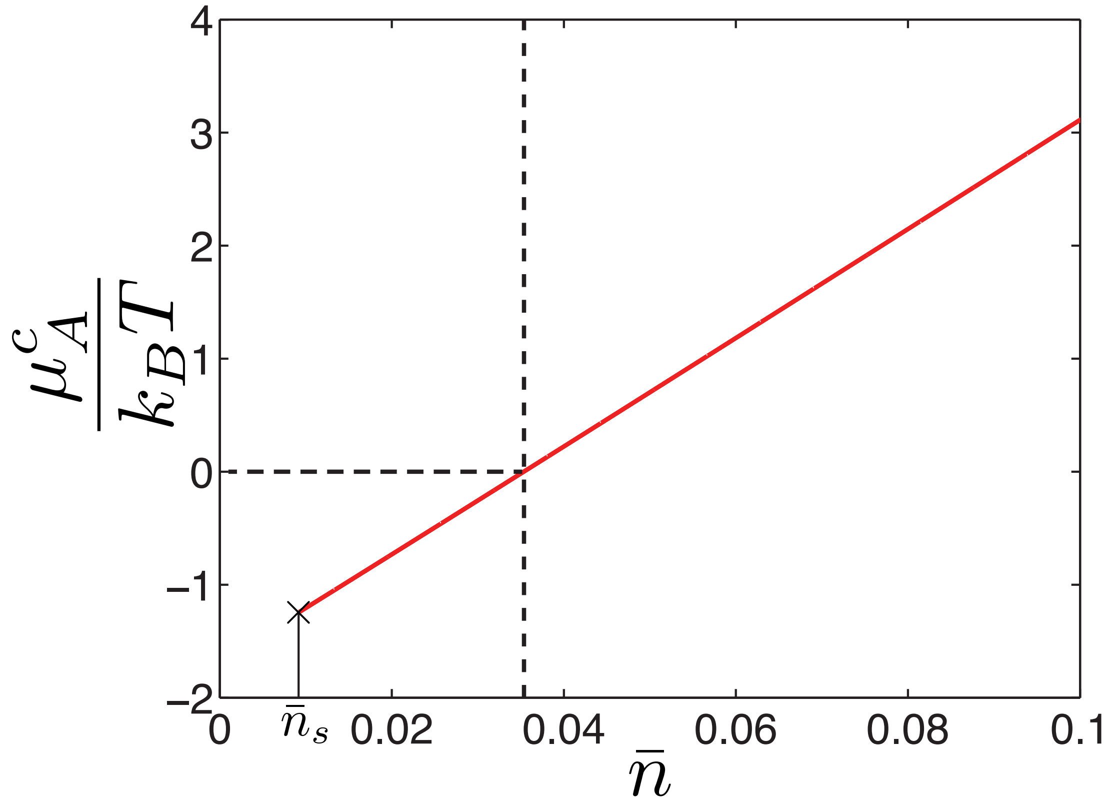

Figure 3.3: Plot of diffusion potential, μ_A^c, for $\bar{n} > \bar{n}_s$, where only solid is stable (see Fig. 3.2). The dashed vertical line corresponds to $\bar{n} = 3.54 \times 10^{-2}$, which is the value of $\bar{n}$ where $\mu_A^c = 0$ (denoted by horizontal dashed line).

In the solid-liquid coexistence region ($\bar{n}_l < \bar{n} < \bar{n}_s$), chemical equilibrium requires that the chemical potentials of the two phases are equal, which will give rise to nonzero diffusion potentials. Thus, the equilibrium vacancy density is determined from $\mu_A^c = \mu_A^l$ and $\mu_L^c = 0$.

3.6.3 An Upper Bound for $\bar{n}$

As discussed earlier the number of atoms, vacancies, and lattice sites of a crystal are related to each other by Eq. (3.8). As a result, the vacancy density, ρ_V^c, can be expressed in terms of ρ_A^c and ρ_L^c as $\rho_V^c = \rho_L^c - \rho_A^c$. By substituting Eqs. (3.31) and

(3.41), ρ_V^c is expressed in terms of $\bar{n}$ and $\mathcal{V}_C^c$ as

$$\rho_V^c = \frac{\chi^c}{\mathcal{V}_C^c} - \rho_0\left(\bar{n}+1\right). \tag{3.53}$$

Since $\mathcal{V}_C^c$ is constant for all $\bar{n}$ values (see Section 3.6.1), an upper bound for $\bar{n}$ arises when the value ρ_V^c is specified. An upper bound for $\bar{n}$, $\bar{n}_{\max}$, is obtained when $\rho_V^c = 0$ (i.e., crystal with no vacancies),

$$\bar{n}_{\max} = \frac{\chi^c}{\mathcal{V}_C^c\rho_0} - 1. \tag{3.54}$$

For $\bar{n} > \bar{n}_{\max}$, the vacancy density takes a negative value, which is unphysical.

The upper bound for the EOF-PFC model with the fitting parameters described in Section 3.1 is $\bar{n}_{\max} = -5.46\times 10^{-2}$, where $\chi^c = 2$ for a *bcc* structure, $\mathcal{V}_C^c = (2.978\mathring{A})^3$, and $\rho_0 = 0.0801\mathring{A}^{-3}$ [54]. Surprisingly, $\bar{n}_{\max} < \bar{n}_l$, where the solid phase is unstable. Therefore, the EOF-PFC model parameterized in Ref. [54] does not stabilize a *bcc* Fe structure with $\rho_V^c \geq 0$.

A potential interpretation of $\rho_V^c < 0$ is the presence of mobile interstitials. However, further investigation is needed to examine this possibility and its validity. In this work, we simply consider this case as an artifact of the model parameterization and proceed to suggest potential solutions. For example, changing the correlation function, as well as the parameterization of a_t and b_t in Eq. (2.13), can change the stability of the solid phase such that $\bar{n}_l < \bar{n}_{\max}$. Another approach is to require the position of the primary peak of the two-body DCF, k_m, to be a function of $\bar{n}$,

$$\begin{aligned} k_m(\bar{n}) &= 2\pi\sqrt{l^2+m^2+n^2}(\mathcal{V}_C^c)^{-\frac{1}{3}} \\ &= 2\pi\sqrt{l^2+m^2+n^2}\left(\frac{\chi^c}{[\rho_V^c+\rho_0(\bar{n}+1)]}\right)^{-\frac{1}{3}}, \end{aligned} \tag{3.55}$$

where

$$\mathcal{V}_C^c(\bar{n}) = \frac{\chi^c}{[\rho_V^c + \rho_0(\bar{n}+1)]} \tag{3.56}$$

is obtained by rearranging Eq. (3.53), and l, m, and n are the Miller indices of the primary family of planes (e.g., $l = 1$, $m = 1$, and $n = 0$ for the *bcc* structure). In this case, the upper bound in $\bar{n}$ no longer arises. Equation (3.55) also allows the direct control of ρ_V^c, which has not been previously possible. It also indicates that the manner in which the two-body DCF changes with $\bar{n}$ depends on the crystal structure via χ^c and the Miller indices. Equation (3.55) should only be applied when the change in $\bar{n}$ is due to the addition or removal of an atom while θ^c, $\mathcal{V}^c$, and N_L^c are held constant. This corresponds to changing $\bar{n}$ while holding θ^c and $\mathcal{V}_C^c$ constant in the PFC model. Note that, in the case where the change in $\bar{n}$ is due to a change in $\mathcal{V}^c$ while N_A^c is held constant, the value of k_m must remain fixed in order to apply a mechanical force, which gives rise to a pressure change.

We point out that a change in k_m reflects a change in the liquid reference state. Therefore, a parameterization that requires k_m to be a function of $\bar{n}$ (as in Eq. (3.55)) requires ρ_0 and the liquid reference pressure, P^0, to change with $\bar{n}$. Since $\bar{n}$ is a function of ρ_0, a relationship for k_m as a function $\bar{n}$ can only be obtained from the dependence of k_m on ρ_0, which must be determined from atomistic simulations.

3.7 Chapter Summary

We have applied the thermodynamic formalism for crystalline solids of Larché and Cahn [56] to develop a thermodynamic relationship between the PFC free energy and thermodynamic state variables. This relationship allows us to examine the thermodynamic processes associated with varying the PFC model parameters. We showed that varying $\bar{n}$ while keeping the unit-cell volume, $\mathcal{V}_C^c$ (and thus lattice spacing, a), and temperature, θ^c, of the bulk crystalline phase constant in a PFC simulation reflects the thermodynamic process of adding or removing atoms to and from lattice sites. Furthermore, changing the computational size of a PFC simulation, while keeping $\bar{n}$ and θ^c constant, reflects the thermodynamic process of adding or removing lattice sites.

The equilibrium conditions between bulk crystalline solid and liquid phases were then imposed on the thermodynamic relationships for the PFC model to obtain a procedure for determining solid-liquid phase coexistence, which we found to be in agreement with the common-tangent construction commonly used in the PFC community. By using the procedure, we found that no stable *bcc* phase with a vacancy density greater than or equal to zero exists for the EOF-PFC model that has been parameterized to *bcc* Fe [54]. Therefore, we proposed an alternative parameterization of the EOF-PFC model, which requires the position of the primary peak of the two-body DCF to be a function of $\bar{n}$.

CHAPTER IV

Thermodynamic Relationships for Calculating Elastic Constants in the Phase-Field Crystal Model

In this chapter, we build on the work of Pisutha-Arnond et al. [53] to derive a thermodynamically consistent procedure for calculating elastic constants from the cDFT-based PFC model. Similar to the thermodynamic relationships of Chapter III, the formulation for calculating elastic constants also uses the thermodynamic formalism for crystalline solids of Larché and Cahn [56]. However, the crystal volume that was used for an independent variable in the Helmholtz free energy in Chapter III (see Eq. (3.9)) is replaced by the Lagrangian strain tensor with elements E_{ij} in order to describe nonhydrostatic strains. Compared to the procedure derived in Ref. [53], we find that the procedure for calculating elastic constants in the cDFT-based PFC model requires the knowledge of the bulk modulus and pressure of the liquid reference state.

This chapter is outlined as follows. First, we review the formalism for representing deformation of a solid. Then, we present the Helmholtz free energy that has elements of the strain tensor as independent variables. We show that elastic constants can be defined from the coefficients of a Taylor expansion of this Helmholtz free energy around the undeformed reference state. These definitions of the elastic constants are used to derive relationships for calculating elastic constants in cDFT-based PFC models. Finally, a relationship between the solid bulk modulus and the PFC free energy is presented.

4.1 Deformation

To represent deformation, consider position vectors that are attached to material points in the undeformed and deformed configurations. These position vectors for the undeformed and deformed configurations, $\mathbf{R}$ and $\mathbf{r}$, respectively, can be expressed in terms of the Cartesian basis vectors, $\{\mathbf{e}_i\}$, as

$$\mathbf{R} = R_1\mathbf{e}_1 + R_2\mathbf{e}_2 + R_3\mathbf{e}_3 \quad \text{and} \quad \mathbf{r} = r_1\mathbf{e}_1 + r_2\mathbf{e}_2 + r_3\mathbf{e}_3, \tag{4.1}$$

where the variables R_1, R_2, R_3 and r_1, r_2, r_3 are the coordinate values. A transformation that maps $\mathbf{R}$ to $\mathbf{r}$ is described by a deformation-gradient tensor, $\boldsymbol{\alpha}$, whose elements are defined as

$$\alpha_{ij} = r_{i,j} = \frac{\partial r_i}{\partial R_j}, \tag{4.2}$$

where the subscripts i and j vary from 1 to 3 in three dimensions and the subscript "$,j$" denotes the derivative with respect to R_j. In this work, we consider only affine deformations.

The degree of deformation of $n(\mathbf{r})$ from R_i can be described by the elements of a displacement-gradient tensor, $u_{i,j}$,

$$u_{i,j} = \frac{\partial(r_i - R_i)}{\partial R_j} = \alpha_{ij} - \delta_{ij}, \tag{4.3}$$

The value of $u_{i,j}$ is also related to the Lagrangian strain tensor by the following relationship (see [57, 84])

$$E_{ij} = \frac{1}{2}\left(u_{i,j} + u_{j,i} + u_{k,i}u_{k,j}\right). \tag{4.4}$$

The values of $u_{i,j}$ and E_{ij} depend on the type of deformation, which is described by the values of α_{ij}. For example, $\boldsymbol{\alpha}$ for isotropic, biaxial, and simple shear deformations, $\boldsymbol{\alpha}_{\text{iso}}$, $\boldsymbol{\alpha}_{\text{bi}}$, and $\boldsymbol{\alpha}_{\text{sh}}$, respectively, are

$$\boldsymbol{\alpha}_{\text{iso}} = \begin{bmatrix} 1+\xi & 0 & 0 \\ 0 & 1+\xi & 0 \\ 0 & 0 & 1+\xi \end{bmatrix}, \quad \boldsymbol{\alpha}_{\text{bi}} = \begin{bmatrix} 1+\xi & 0 & 0 \\ 0 & 1-\xi & 0 \\ 0 & 0 & 1 \end{bmatrix}, \quad \boldsymbol{\alpha}_{\text{sh}} = \begin{bmatrix} 1 & -\xi & 0 \\ 0 & 1 & 0 \\ 0 & 0 & 1 \end{bmatrix}, \tag{4.5}$$

where ξ is a parameter that quantifies the amount of deformation.

Consequently, the displacment-gradient tensor for isotropic, biaxial, and simple-shear deformations, $\mathbf{u}_{\text{iso}}$, $\mathbf{u}_{\text{bi}}$, and $\mathbf{u}_{\text{sh}}$, respectively, are

$$\mathbf{u}_{\text{iso}} = \begin{bmatrix} \xi & 0 & 0 \\ 0 & \xi & 0 \\ 0 & 0 & \xi \end{bmatrix}, \quad \mathbf{u}_{\text{bi}} = \begin{bmatrix} \xi & 0 & 0 \\ 0 & -\xi & 0 \\ 0 & 0 & 0 \end{bmatrix}, \quad \mathbf{u}_{\text{sh}} = \begin{bmatrix} 0 & -\xi-1 & 0 \\ 0 & 0 & 0 \\ 0 & 0 & 0 \end{bmatrix}, \tag{4.6}$$

and the corresponding strain tensors are

$$\begin{aligned}
\mathbf{E}_{\text{iso}} &= \begin{bmatrix} \xi+\frac{1}{2}\xi^2 & 0 & 0 \\ 0 & \xi+\frac{1}{2}\xi^2 & 0 \\ 0 & 0 & \xi+\frac{1}{2}\xi^2 \end{bmatrix}, \\
\mathbf{E}_{\text{bi}} &= \begin{bmatrix} \xi+\frac{1}{2}\xi^2 & 0 & 0 \\ 0 & -\xi+\frac{1}{2}\xi^2 & 0 \\ 0 & 0 & 0 \end{bmatrix}, \\
\mathbf{E}_{\text{sh}} &= \begin{bmatrix} 0 & -\frac{1}{2}\xi & 0 \\ -\frac{1}{2}\xi & \frac{1}{2}\xi & 0 \\ 0 & 0 & 0 \end{bmatrix},
\end{aligned} \tag{4.7}$$

respectively.

4.2 Thermodynamics for Non-Hydrostatically Stressed Bulk Crystalline Phase

In Chapter III, we considered only hydrostatic deformation so that the deformation can be specified solely by the crystal volume, $\mathcal{V}^c$. Therefore, the thermodynamic relationship for a bulk crystalline phase presented in Chapter III is only valid for systems under hydrostatic pressure. In order to consider nonhydrostatic stresses, which are required for defining the full set of elastic constants, the Helmholtz free energy is now written in terms of E_{ij} instead of $\mathcal{V}^c_C$ [84], i.e.,

$$F^c = F^c(\theta^c, E_{ij}, N^c_A, N^c_L). \tag{4.8}$$

As in Eq. (3.9), Eq. (4.8) is defined for an equilibrium bulk crystalline phase.

The elastic constants as well as other thermodynamic quantities can be defined from the coefficients of a Taylor expansion of Eq. (4.8) around the reference undeformed state, $E_{ij} = 0$ [61, 84],

$$\begin{aligned} F^c(\theta^c, E_{ij}, N_A^c, N_L^c) &= F^c(\theta^c, 0, N_A^c, N_L^c) + \left.\frac{\partial F^c}{\partial E_{ij}}\right|^{u}_{\theta^c, E^*_{mn}, N_A^c, N_L^c} E_{ij} \\ &\quad + \frac{1}{2}\left.\frac{\partial^2 F^c}{\partial E_{ij}\partial E_{kl}}\right|^{u}_{\theta^c, E^*_{mn}, N_A^c, N_L^c} E_{ij}E_{kl} + \cdots , \end{aligned} \tag{4.9}$$

where the superscript u denotes that the derivatives are evaluated at the undeformed state and the subscripts E^*_{mn} indicate that the elements of the strain tensors other than those involved in the partial derivative are held constant. According to thermoelasticity theory for stressed crystals [61, 84], the elements of the Piola-Kirchoff stress, T_{ij}, and strain, E_{ij}, tensors can be defined from the partial derivatives of F^c with respect to E_{ij},

$$T_{ij} \equiv \frac{1}{\mathcal{V}'}\left.\frac{\partial F^c}{\partial E_{ij}}\right|^{u}_{\theta^c, E^*_{mn}, N_A^c, N_L^c} \quad \text{and} \quad C_{ijkl} \equiv \frac{1}{\mathcal{V}'}\left.\frac{\partial^2 F^c}{\partial E_{ij}\partial E_{kl}}\right|^{u}_{\theta^c, E^*_{mn}, N_A^c, N_L^c} . \tag{4.10}$$

For a bulk crystal with cubic symmetry, the elastic constants can be reduced to three unique non-zero terms: $C_{11} = C_{iiii}$, $C_{12} = C_{iijj}$, and $C_{44} = C_{ijij} = C_{ijji}$. Under hydrostatic pressure, P^c, $T_{ij} = -P^c\delta_{ij}$.

A free energy that is explicitly a function of E_{ij} can employ Eq. (4.10) to determine T_{ij} and C_{ijkl} of the system. However, since the PFC free energy is not explicitly a function of E_{ij}, relationships that are in terms of ξ will be more convenient to calculate T_{ij} and C_{ijkl} in the PFC model. Such relationships are obtained by expressing F^c in terms of ξ by substituting Eq. (4.7) into Eq. (4.9). Expressions for F^c in terms of ξ

for isotropic, biaxial, and simple-shear deformations are

$$\begin{aligned} F^c_{\text{iso}}(\theta^c,\xi,N^c_A,N^c_L) &= F^c_{\text{iso}}(\theta^c,0,N^c_A,N^c_L)+T_{11}\mathcal{V}'(\xi+\frac{1}{2}\xi^2)+T_{22}\mathcal{V}'(\xi+\frac{1}{2}\xi^2) \\ &\quad +T_{33}\mathcal{V}'(\xi+\frac{1}{2}\xi^2)+3C_{12}\mathcal{V}'(\xi+\frac{1}{2}\xi^2)^2+\frac{3}{2}C_{11}\mathcal{V}'(\xi+\frac{1}{2}\xi^2)^2 \\ &= F^c_{\text{iso}}(\theta^c,0,N^c_A,N^c_L)-3P^c\mathcal{V}'\xi+\frac{1}{2}(-3P^c+3C_{11}+6C_{12})\mathcal{V}'\xi^2 \\ &\quad +\frac{1}{2}(3C_{11}+6C_{12})\mathcal{V}'\xi^3+\frac{1}{4}(3C_{12}+6C_{11})\mathcal{V}'\xi^4, \end{aligned} \tag{4.11}$$

$$\begin{aligned} F^c_{\text{bi}}(\theta^c,\xi,N^c_A,N^c_L) &= F^c_{\text{bi}}(\theta^c,0,N^c_A,N^c_L)+T_{11}\mathcal{V}'\left(\xi+\frac{1}{2}\xi^2\right)+T_{22}\mathcal{V}'\left(-\xi+\frac{1}{2}\xi^2\right) \\ &\quad +C_{11}\mathcal{V}'\left(-\xi+\frac{1}{2}\xi^2\right)^2+C_{11}\mathcal{V}'\left(\xi+\frac{1}{2}\xi^2\right)^2 \\ &\quad +C_{12}\mathcal{V}'\left(\frac{1}{4}\xi^4-\xi^2\right) \\ &= F^c_{\text{bi}}(\theta^c,0,N^c_A,N^c_L)+(-P^c+C_{11}-C_{12})\mathcal{V}'\xi^2 \\ &\quad +\frac{1}{4}(3C_{12}+6C_{11})\mathcal{V}'\xi^4, \end{aligned} \tag{4.12}$$

and

$$\begin{aligned} F^c_{\text{sh}}(\theta^c,\xi,N^c_A,N^c_L) &= F^c_{\text{sh}}(\theta^c,0,N^c_A,N^c_L)-\frac{1}{2}T_{12}\mathcal{V}'\xi-\frac{1}{2}T_{21}\mathcal{V}'\xi+\frac{1}{2}T_{22}\mathcal{V}'\xi^2 \\ &\quad +\frac{1}{2}C_{44}\mathcal{V}'\xi^2+\frac{1}{8}C_{11}\mathcal{V}'\xi^4 \\ &= F^c_{\text{sh}}(\theta^c,0,N^c_A,N^c_L)+\frac{1}{2}\left(-P^c+C_{44}\right)\mathcal{V}'\xi^2+\frac{1}{8}C_{11}\mathcal{V}'\xi^4, \end{aligned} \tag{4.13}$$

where the subscripts iso, bi, and sh denote isotropic, biaxial, and shear deformations, respectively.

Relationships for elastic constants are obtained from the second derivatives of Eqs.

(4.11), (4.12), and (4.13) with respect to ξ while holding θ^c, N_A^c, and N_L^c constant,

$$\begin{aligned}
\mathcal{Q}_{\mathrm{iso}} \equiv \left.\frac{1}{\mathcal{V}'}\frac{\partial^2 F_{\mathrm{iso}}^c}{\partial \xi^2}\right|_{\theta,N_A^c,N_L^c}^{\xi=0} &= -3P^c + 3C_{11} + 6C_{12} \\
\mathcal{Q}_{\mathrm{bi}} \equiv \left.\frac{1}{\mathcal{V}'}\frac{\partial^2 F_{\mathrm{bi}}^c}{\partial \xi^2}\right|_{\theta^c,N_A^c,N_L^c}^{\xi=0} &= -2P^c + 2C_{11} - 2C_{12} \\
\mathcal{Q}_{\mathrm{sh}} \equiv \left.\frac{1}{\mathcal{V}'}\frac{\partial^2 F_{\mathrm{sh}}^c}{\partial \xi^2}\right|_{\theta^c,N_A^c,N_L^c}^{\xi=0} &= -P^c + C_{44},
\end{aligned} \tag{4.14}$$

where the superscript $\xi = 0$ denotes that the derivatives are evaluated at the undeformed state. It is worth noting that the elastic constants are defined in terms of derivatives of the reference-volume FED (see Eq. (3.24)); thus, the pressure change is due to a mechanical force. The three elastic constants, C_{11}, C_{12}, and C_{44}, are determined by rewriting the expressions in Eq. (4.14) as

$$\begin{aligned}
C_{11} &= P^c + \frac{1}{9}\mathcal{Q}_{\mathrm{iso}} + \frac{1}{3}\mathcal{Q}_{\mathrm{bi}} \\
C_{12} &= \frac{1}{9}\mathcal{Q}_{\mathrm{iso}} - \frac{1}{6}\mathcal{Q}_{\mathrm{bi}} \\
C_{44} &= \mathcal{Q}_{\mathrm{sh}} + P^c,
\end{aligned} \tag{4.15}$$

where P^c is determined from

$$P^c = -\left.\frac{1}{3\mathcal{V}'}\frac{\partial F_{\mathrm{iso}}^c}{\partial \xi}\right|_{\theta,N_A^c,N_L^c}^{\xi=0}. \tag{4.16}$$

The expressions in Eqs. (4.14) and (4.15) form the basis for calculating elastic constants in the PFC model. In Ref. [53], these equations were used to determine the elastic constants for the SH-PFC model. We will now apply the approach to the cDFT-based PFC model.

4.3 Relationships for Calculating Elastic Constants in the cDFT-based PFC Model

The relationships in Section 4.2 are used to derive a procedure for calculating elastic constants from the cDFT-based PFC model. However, two modifications to Eq. (4.14) must be implemented before it can be directly applied to the cDFT-based PFC model. First, as shown in Eq. (4.14), the calculation of elastic constants requires that the total number of atoms, N_A^c, and lattice sites, N_L^c, to be constant during deformation. The value of N_L^c is fixed as long as the number of peaks in the computational domain remain constant during deformation. On the other hand, in order to fix N_A^c during deformation, the value of $\bar{n}$,

$$\bar{n} = \frac{\rho_A^c - \rho_0}{\rho_0} = \frac{\rho_A'^c / J_t - \rho_0}{\rho_0}, \tag{4.17}$$

must be modified so that $\rho_A'^c \equiv N_A^c/\mathcal{V}'$ is kept constant. To conveniently hold N_A^c constant, we define a new average scaled density that is in terms of $\bar{\rho}'$,

$$\bar{n}' \equiv \frac{\rho_A'^c - \rho_0}{\rho_0}, \tag{4.18}$$

where holding $\bar{n}'$ constant is equivalent to keeping N_A^c constant.

Second, since the PFC model is based on a free-energy difference from a reference liquid phase, the PFC free energy is related to F_t^c by

$$\Delta\mathcal{F}_{\mathrm{PFC},t}^{\mathrm{bulk},c}[n_{eq}^{\mathrm{bulk},c}(\mathbf{r}), \xi] = F_t^c - F_t^0, \tag{4.19}$$

where F_t^0 is the Helmholtz free energy of the liquid reference state, and the PFC free energy for the bulk crystalline phase depends on ξ and the type of deformation denoted by the subscript t (t=iso,bi, or sh). Using Eq. (4.19), an alternative form of

Eq. (4.14) is

$$\begin{aligned}
\mathcal{H}_t &= \frac{\partial^2}{\partial \xi^2}\left(\frac{\Delta \mathcal{F}^{\text{bulk},c}_{\text{PFC},t}}{\mathcal{V}'}\right)\Bigg|^{\xi=0}_{\theta^c,\bar{n}'} \\
&= \frac{\partial^2 F^c_t}{\partial \xi^2}\bigg|^{\xi=0}_{\theta^c,\bar{n}'} - \frac{\partial^2 F^0_t}{\partial \xi^2}\bigg|^{\xi=0}_{\theta^c,\bar{n}'} \\
&= \mathcal{Q}_t - \frac{\partial^2 F^0_t}{\partial \xi^2}\bigg|^{\xi=0}_{\theta^c,\bar{n}'}
\end{aligned} \tag{4.20}$$

where the second derivative of F^0_t with respect to ξ arises as an additional term as compared to the case for SH-PFC (Eq. (4.14)). Note that we have left out the dependence of $\Delta \mathcal{F}^{\text{bulk},c}_{\text{PFC},t}[n^{\text{bulk},c}_{eq}(\mathbf{r}),\xi]$ for brevity. Further note that N^c_A is held constant by keeping $\bar{n}'$ fixed.

The additional term associated with the liquid reference state in Eq. (4.20) is related to the bulk modulus, $\mathcal{K}^0$, and pressure, P^0, of the liquid reference state,

$$\begin{aligned}
P^0 &\equiv -\frac{\partial F^0_t}{\partial \mathcal{V}}\bigg|_{\theta,\bar{n}'} \\
\mathcal{K}^0 &\equiv -\mathcal{V}\frac{\partial P^0}{\partial \mathcal{V}}\bigg|_{\theta,\bar{n}'} = \mathcal{V}\frac{\partial^2 F^0_t}{\partial \mathcal{V}^2}\bigg|_{\theta,\bar{n}'},
\end{aligned} \tag{4.21}$$

To demonstrate this fact, we rewrite the second derivative of F^0_t to be with respect to the system volume, $\mathcal{V}$, by applying the chain rule,

$$\begin{aligned}
\frac{\partial^2}{\partial \xi^2} &= \frac{\partial}{\partial \xi}\left(\frac{\partial}{\partial \xi}\right) = \frac{\partial}{\partial \xi}\left(\frac{\partial \mathcal{V}}{\partial \xi}\frac{\partial}{\partial \mathcal{V}}\right) \\
&= \frac{\partial^2 \mathcal{V}}{\partial \xi^2}\frac{\partial}{\partial \mathcal{V}} + \frac{\partial \mathcal{V}}{\partial \xi}\left(\frac{\partial \mathcal{V}}{\partial \xi}\frac{\partial}{\partial \mathcal{V}}\left(\frac{\partial}{\partial \mathcal{V}}\right)\right) \\
&= \frac{\partial^2 \mathcal{V}}{\partial \xi^2}\frac{\partial}{\partial \mathcal{V}} + \left(\frac{\partial \mathcal{V}}{\partial \xi}\right)^2 \frac{\partial^2}{\partial \mathcal{V}^2}.
\end{aligned} \tag{4.22}$$

Thus, the second derivative of F^0_t with respect to ξ is expressed as

$$\frac{\partial^2 F^0_t}{\partial \xi^2}\bigg|^{\xi=0}_{\theta,\bar{n}'} = \frac{\partial^2 \mathcal{V}}{\partial \xi^2}\frac{\partial F^0_t}{\partial \mathcal{V}}\bigg|^{\xi=0}_{\theta,\bar{n}'} + \left(\frac{\partial \mathcal{V}}{\partial \xi}\right)^2 \frac{\partial^2 F^0_t}{\partial \mathcal{V}^2}\bigg|^{\xi=0}_{\theta,\bar{n}'}, \tag{4.23}$$

where the functional dependence of $\mathcal{V}$ on ξ depends on the type of deformation. Specifically, for isotropic deformations,

$$\begin{aligned}
\left.\frac{\partial^2 F^0_{\text{iso}}}{\partial \xi^2}\right|^{\xi=0}_{\theta,\bar{n}'} &= 6(1+\xi)\mathcal{V}'\left.\frac{\partial F^0_{\text{iso}}}{\partial \mathcal{V}}\right|^{\xi=0}_{\theta,\bar{n}'} + 9(1+\xi)^4(\mathcal{V}')^2\left.\frac{\partial^2 F^0_{\text{iso}}}{\partial \mathcal{V}^2}\right|^{\xi=0}_{\theta,\bar{n}'} \\
&= -6(1+\xi)\mathcal{V}'P^0\Big|^{\xi=0}_{\theta,\bar{n}'} + 9(1+\xi)^4(\mathcal{V}')^2\left.\frac{\mathcal{K}^0}{(1+\xi)^3\mathcal{V}'}\right|^{\xi=0}_{\theta,\bar{n}'} \\
&= -6\mathcal{V}'P^0 + 9\mathcal{V}'\mathcal{K}^0, \qquad (4.24)
\end{aligned}$$

where $\mathcal{V} = (1+\xi)^3\mathcal{V}'$ for isotropic deformation. Similary, for biaxial and simple-shear deformations,

$$\left.\frac{\partial^2 F^0_{\text{bi}}}{\partial \xi^2}\right|^{\xi=0}_{\theta,\bar{n}'} = 2\mathcal{V}'P^0 \qquad (4.25)$$

and

$$\left.\frac{\partial^2 F^0_{\text{sh}}}{\partial \xi^2}\right|^{\xi=0}_{\theta,\bar{n}'} = 0, \qquad (4.26)$$

respectively, where $\mathcal{V}$ is $(1-\xi^2)\mathcal{V}'$ and $\mathcal{V}'$ for biaxial and simple-shear deformations, respectively.

Substituting Eqs. (4.14), (4.24), (4.25), and (4.26) into Eq. (4.20), we obtain

$$\begin{aligned}
\mathcal{H}_{\text{iso}} &\equiv \frac{1}{\mathcal{V}'}\frac{\partial^2 \Delta\mathcal{F}^{\text{bulk},c}_{\text{PFC,iso}}}{\partial\xi^2}\bigg|^{\xi=0}_{\theta^c,\bar{n}'} \\
&= \frac{1}{\mathcal{V}'}\frac{\partial^2 F^c_{\text{iso}}}{\partial\xi^2}\bigg|^{\xi=0}_{\theta^c,\bar{n}'} - \frac{1}{\mathcal{V}'}\frac{\partial^2 F^0_{\text{iso}}}{\partial\xi^2}\bigg|^{\xi=0}_{\theta,\bar{n}'} \\
&= -3P^c + 3C_{11} + 6C_{12} - 9\mathcal{K}^0 + 6P^0
\end{aligned}$$

$$\begin{aligned}
\mathcal{H}_{\text{bi}} &\equiv \frac{1}{\mathcal{V}'}\frac{\partial^2 \Delta\mathcal{F}^{\text{bulk},c}_{\text{PFC,bi}}}{\partial\xi^2}\bigg|^{\xi=0}_{\theta^c,\bar{n}'} \\
&= \frac{1}{\mathcal{V}'}\frac{\partial^2 F^c_{\text{bi}}}{\partial\xi^2}\bigg|^{\xi=0}_{\theta^c,\bar{n}'} - \frac{1}{\mathcal{V}'}\frac{\partial^2 F^0_{\text{bi}}}{\partial\xi^2}\bigg|^{\xi=0}_{\theta,\bar{n}'} \\
&= -2P^c + 2C_{11} - 2C_{12} - 2P^0
\end{aligned}$$

$$\begin{aligned}
\mathcal{H}_{\text{sh}} &\equiv \frac{1}{\mathcal{V}'}\frac{\partial^2 \Delta\mathcal{F}^{\text{bulk},c}_{\text{PFC,sh}}}{\partial\xi^2}\bigg|^{\xi=0}_{\theta^c,\bar{n}'} \\
&= \frac{1}{\mathcal{V}'}\frac{\partial^2 F^c_{\text{sh}}}{\partial\xi^2}\bigg|^{\xi=0}_{\theta^c,\bar{n}'} - \frac{1}{\mathcal{V}'}\frac{\partial^2 F^0_{\text{sh}}}{\partial\xi^2}\bigg|^{\xi=0}_{\theta,\bar{n}'} \\
&= -P^c + C_{44}.
\end{aligned} \tag{4.27}$$

Therefore, the three elastic constants, C_{11}, C_{12}, and C_{44}, for the cDFT-based PFC model can be calculated from the derivatives of the PFC free energy via

$$\begin{aligned}
C_{11} &= P^c + \frac{1}{9}\mathcal{H}_{\text{iso}} + \frac{1}{3}\mathcal{H}_{\text{bi}} - 4\mathcal{K}^0 \\
C_{12} &= \frac{1}{9}\mathcal{H}_{\text{iso}} - \frac{1}{6}\mathcal{H}_{\text{bi}} + \frac{1}{2}\mathcal{K}^0 + P^0 \\
C_{44} &= P^c + \mathcal{H}_{\text{sh}},
\end{aligned} \tag{4.28}$$

where

$$\begin{aligned} P^c &= -\frac{1}{3\mathcal{V}'}\frac{\partial \Delta \mathcal{F}^{\mathrm{bulk},c}_{\mathrm{PFC,iso}}}{\partial \xi}\bigg|^{\xi=0}_{\theta^c,\bar{n}'} - \frac{1}{3\mathcal{V}'}\frac{\partial F^0_{\mathrm{iso}}}{\partial \xi}\bigg|^{\xi=0}_{\theta,\bar{n}'} \\ &= -\frac{1}{3\mathcal{V}'}\frac{\partial \Delta \mathcal{F}^{\mathrm{bulk},c}_{\mathrm{PFC,iso}}}{\partial \xi}\bigg|^{\xi=0}_{\theta^c,\bar{n}'} - \frac{1}{3\mathcal{V}'}\frac{\partial \mathcal{V}}{\partial \xi}\frac{\partial F^0_{\mathrm{iso}}}{\partial \mathcal{V}}\bigg|^{\xi=0}_{\theta,\bar{n}'} \\ &= -\frac{1}{3\mathcal{V}'}\frac{\partial \Delta \mathcal{F}^{\mathrm{bulk},c}_{\mathrm{PFC,iso}}}{\partial \xi}\bigg|^{\xi=0}_{\theta^c,\bar{n}'} + P^0. \end{aligned} \tag{4.29}$$

Additionally, the value of $\mathcal{K}^0$ is related to the two-body DCF at $k = 0$ [48] by

$$\mathcal{K}^0 = \frac{1}{\kappa^0} = \rho_0 k_B T(1 - \rho_0 \hat{C}^{(2)}(0)), \tag{4.30}$$

where κ^0 is the liquid compressibility of the liquid reference state.

4.4 Solid Bulk Modulus

The solid bulk modulus of the bulk crystalline phase, $\mathcal{K}^c$, which measures the Helmholtz energy change due to hydrostatic deformation, can be directly calculated from the derivative of the cDFT-based PFC free energy with respect to $\mathcal{V}^c$. To demonstrate this fact, consider the definition of $\mathcal{K}^c$ [84],

$$\mathcal{K}^c = \mathcal{V}^c \frac{\partial^2 F^c_{\mathrm{iso}}}{\partial (\mathcal{V}^c)^2}\bigg|_{\theta^c,\bar{n}'} = \mathcal{V}^c \frac{\partial^2 \mathcal{F}^{\mathrm{bulk},c}_{\mathrm{PFC,iso}}}{\partial (\mathcal{V}^c)^2}\bigg|^{\xi=0}_{\theta^c,\bar{n}'}. \tag{4.31}$$

The second derivative of $\mathcal{F}^{\mathrm{bulk},c}_{\mathrm{PFC,iso}}$ with respect to $\mathcal{V}^c$ can be written in terms of

C_{11}, C_{12}, and P^c using the chain rule in Eqs. (4.22) to be

$$\begin{aligned}
\mathcal{K}^c &= \mathcal{V}^c \left. \frac{\partial^2 \mathcal{F}^{\mathrm{bulk},c}_{\mathrm{PFC,iso}}}{\partial (\mathcal{V}^c)^2} \right|^{\xi=0}_{\theta^c,\bar{n}'} \\
&= \left. (1+\xi)^3 \mathcal{V}' \right|^{\xi=0} \left(\left. \frac{1}{3(1+\xi)^2 \mathcal{V}'} \right|^{\xi=0} \right)^2 \\
&\quad \left(\left. \frac{\partial^2 \mathcal{F}^{\mathrm{bulk},c}_{\mathrm{PFC,iso}}}{\partial \xi^2} \right|^{\xi=0}_{\theta^c,\bar{n}'} - \left. 6(1+\xi)\mathcal{V}' \right|^{\xi=0} \left. \frac{1}{3(1+\xi)^2 \mathcal{V}'} \right|^{\xi=0} \left. \frac{\partial \mathcal{F}^{\mathrm{bulk},c}_{\mathrm{PFC,iso}}}{\partial \xi} \right|^{\xi=0}_{\theta^c,\bar{n}'} \right) \\
&= \frac{1}{9\mathcal{V}'} \left(\left. \frac{\partial^2 \mathcal{F}^{\mathrm{bulk},c}_{\mathrm{PFC,iso}}}{\partial \xi^2} \right|^{\xi=0}_{\theta^c,\bar{n}'} - 2 \left. \frac{\partial \mathcal{F}^{\mathrm{bulk},c}_{\mathrm{PFC,iso}}}{\partial \xi} \right|^{\xi=0}_{\theta^c,\bar{n}'} \right) \\
&= \frac{1}{9\mathcal{V}'} \left(\left. \frac{\partial^2 F^c_{\mathrm{iso}}}{\partial \xi^2} \right|^{\xi=0}_{\theta^c,\bar{n}'} - 2 \left. \frac{\partial F^c_{\mathrm{iso}}}{\partial \xi} \right|^{\xi=0}_{\theta^c,\bar{n}'} \right) \\
&= \frac{C_{11} + 2C_{12} + P^c}{3},
\end{aligned} \tag{4.32}$$

where $\mathcal{V}^c = (1+\xi)^3 \mathcal{V}'$ for isotropic deformation, and Eqs. (4.14) and (4.16) are employed for the last equality. Since $\mathcal{F}^{\mathrm{bulk},c}_{\mathrm{PFC,iso}} = \Delta\mathcal{F}^{\mathrm{bulk},c}_{\mathrm{PFC,iso}} + F^0_{\mathrm{iso}}$, $\mathcal{K}_c$ can also be expressed in terms of the second derivative of the PFC free energy with respect to ξ

$$\begin{aligned}
\mathcal{K}^c &= \mathcal{V}^c \left. \frac{\partial^2 \mathcal{F}^{\mathrm{bulk},c}_{\mathrm{PFC,iso}}}{\partial (\mathcal{V}^c)^2} \right|^{\xi=0}_{\theta^c,\bar{n}'} \\
&= \mathcal{V}^c \left. \frac{\partial^2 \Delta\mathcal{F}^{\mathrm{bulk},c}_{\mathrm{PFC,iso}}}{\partial (\mathcal{V}^c)^2} \right|^{\xi=0}_{\theta^c,\bar{n}'} + \mathcal{V} \left. \frac{\partial^2 F^0_{\mathrm{iso}}}{\partial \mathcal{V}^2} \right|^{\xi=0}_{\theta,\bar{n}'} \\
&= \mathcal{V}^c \left. \frac{\partial^2 \Delta\mathcal{F}^{\mathrm{bulk},c}_{\mathrm{PFC,iso}}}{\partial (\mathcal{V}^c)^2} \right|^{\xi=0}_{\theta^c,\bar{n}'} + \mathcal{K}^0,
\end{aligned} \tag{4.33}$$

where a knowledge of $\mathcal{K}^0$ is required to determine $\mathcal{K}^c$ from the PFC free energy.

4.5 Chapter Summary

We have presented thermodynamic relationships for calculating elastic constants from cDFT-based PFC models. We demonstrated that a knowledge of the bulk modulus and pressure of the liquid reference state are required to calculate the elastic constants of a bulk crystalline phase with cubic symmetry. A relationship to calculate the bulk modulus of the crystalline phase from the PFC free energy was also derived.

CHAPTER V

Numerical Implementation of Deformation in the Phase-Field Crystal Model

In Chapter IV, we presented thermodynamic relationships for calculating elastic constants in the PFC model. We demonstrated that the calculation of elastic constants requires the evaluation of the PFC free energy, $\Delta\mathcal{F}^{\text{bulk,c}}_{\text{PFC},t}$, for different types of deformation. Numerical deformation is conventionally implemented in the PFC model by evaluating the free energy on coordinates that have been mapped to a desired deformed state via a deformation-gradient tensor [53, 55, 62]. Although straightforward, this method, as we will later show, requires interpolation of the order parameter values for shear-type deformations. Therefore, in this chapter we explore two alternative numerical methods for applying deformation. The first alternative method maps the Laplacian operator in the PFC free energy from deformed to undeformed coordinates, which eliminates the need for interpolation. The second alternative method is formulated in Fourier space and applies deformation via a scaling of the wave vectors, which can be used when the PFC free energy is expressed in Fourier space. Using these methods, we evaluate the PFC free-energy density (FED) for an order parameter profile of a *bcc* structure, assuming the one-mode approximation, and compare the accuracy and efficiency of these methods. The Fourier-space method is then used to implement the relationships developed in Chapter IV to calculate the elastic constants and solid bulk modulus for *bcc* structures stabilized by the EOF-PFC model.

This chapter is outlined as follows. In Section 5.1, we provide the theoretical background for numerically evaluating the FED in a deformed state within the PFC model. In Section 5.2, we review the conventional method used in the PFC literature for evaluating deformed-state FEDs, and illustrate the need for interpolation when applying deformations that skew the computational domain. In Section 5.3, we map the Laplacian operator from deformed to undeformed coordinates, which eliminates the need for interpolation. In Section 5.4, we formulate a Fourier-space method that applies deformation via a scaling of the wave vectors. In Section 5.5, the numerical accuracy and computational efficiency of the three methods for isotropic, biaxial, and simple-shear deformations are compared. Finally, in Section 5.6, the Fourier-space method for deformation is employed to implement the relationships developed in Chapter IV to calculate elastic constants and the solid bulk modulus for *bcc* structures from the EOF-PFC model.

5.1 Background

In this section, we present the theoretical concepts that are used to numerically evaluate the PFC free energy of a deformed system. We first discuss the mathematical formalism for describing deformations, and then provide the notations used to describe discretization in later sections.

5.1.1 Deformation

To represent deformation, we use the same notation described in Section 4.1, where the deformation-gradient tensor for isotropic, biaxial, and simple-shear deformations are repeated here:

$$\boldsymbol{\alpha}_{\text{iso}} = \begin{bmatrix} 1+\xi & 0 & 0 \\ 0 & 1+\xi & 0 \\ 0 & 0 & 1+\xi \end{bmatrix}, \quad \boldsymbol{\alpha}_{\text{bi}} = \begin{bmatrix} 1+\xi & 0 & 0 \\ 0 & 1-\xi & 0 \\ 0 & 0 & 1 \end{bmatrix}, \quad \boldsymbol{\alpha}_{\text{sh}} = \begin{bmatrix} 1 & -\xi & 0 \\ 0 & 1 & 0 \\ 0 & 0 & 1 \end{bmatrix}. \quad (5.1)$$

The tensor for biaxial deformation describes an expansion along the r_1 axis and compression along the r_2 axis, respectively, while the tensor for simple-shear deformation describes a shear along the r_1 coordinate. The inverses of these tensors are

$$\boldsymbol{\alpha}_{\text{iso}}^{-1} = \begin{bmatrix} \frac{1}{1+\xi} & 0 & 0 \\ 0 & \frac{1}{1+\xi} & 0 \\ 0 & 0 & \frac{1}{1+\xi} \end{bmatrix}, \quad \boldsymbol{\alpha}_{\text{bi}}^{-1} = \begin{bmatrix} \frac{1}{1+\xi} & 0 & 0 \\ 0 & \frac{1}{1-\xi} & 0 \\ 0 & 0 & 1 \end{bmatrix}, \quad \boldsymbol{\alpha}_{\text{sh}}^{-1} = \begin{bmatrix} 1 & \xi & 0 \\ 0 & 1 & 0 \\ 0 & 0 & 1 \end{bmatrix}. \quad (5.2)$$

The ratio of the system volume, $\mathcal{V}$, to the reference volume, $\mathcal{V}'$, denoted by $J \equiv \mathcal{V}/\mathcal{V}'$, is given by the determinant of $\boldsymbol{\alpha}$, i.e., $J = \det|\boldsymbol{\alpha}|$ [57]. The value of J for isotropic, biaxial, and simple-shear deformations are

$$J_{\text{iso}} = (1+\xi)^3, \quad J_{\text{bi}} = 1-\xi^2, \quad J_{\text{sh}} = 1. \quad (5.3)$$

The order parameter for the undeformed state is denoted as $\phi(\mathbf{x})$, while the order parameter for the deformed state is denoted as $\phi_t^D(\mathbf{x})$, where t denotes the type of deformation, e.g., t = iso for isotropic deformation. We focus on the potential applications of the methods for calculations of equilibrium properties such as elastic constants. Therefore, we consider the evaluation of the PFC FED for a single deformed unit cell.

5.1.2 Discretization

In this section, we present the notations for the discretization of the Laplacian operator, which is employed to numerically evaluate the PFC FED (see Chapter II). Specifically, we consider the discretizations of the Laplacian of an order parameter in the undeformed and deformed state. These notations will be used later to show that an interpolation step is required when applying simple-shear deformation with the conventional method.

In the undeformed configuration, we assume that the system of interest resides in a rectangular prism whose sides are parallel to each one of the coordinate axes. The lengths of the sides parallel to the axes of R_1, R_2, and R_3 are L_1, L_2, and L_3, respectively. The side parallel to the axis of coordinate R_i is discretized into $N_i + 1$ grid points with a grid spacing of ΔR_i, where $i = 1, 2$, or 3. Therefore, the coordinate values in each direction can be expressed as

$$R_1^l = R_1^0 + l\Delta R_1, \quad R_2^m = R_2^0 + m\Delta R_2, \quad R_3^n = R_3^0 + n\Delta R_3, \tag{5.4}$$

where l, m, and n are indices of the computational grid points and take on integer values $l = 0, \ldots, N_1$, $m = 0, \ldots, N_2$, $n = 0, \ldots, N_3$; the variables R_1^0, R_2^0, and R_3^0 are lower bounds of the coordinate values.

Using the notation presented above, the Laplacian of the order parameter of the undeformed state can be approximated with a second-order central-difference scheme as

$$
\begin{aligned}
&\nabla^2_{\mathbf{R}}\phi\left(R_1^l, R_2^m, R_3^n\right) \approx \\
&\frac{\phi\left(R_1^l+\Delta R_1, R_2^m, R_3^n\right)+\phi\left(R_1^l-\Delta R_1, R_2^m, R_3^n\right)-2\phi\left(R_1^l, R_2^m, R_3^n\right)}{\left(\Delta R_1\right)^2} \\
&+\frac{\phi\left(R_1^l, R_2^m+\Delta R_2, R_3^n\right)+\phi\left(R_1^l, R_2^m-\Delta R_2, R_3^n\right)-2\phi\left(R_1^l, R_2^m, R_3^n\right)}{\left(\Delta R_2\right)^2} \\
&+\frac{\phi\left(R_1^l, R_2^m, R_3^n+\Delta R_3\right)+\phi\left(R_1^l, R_2^m, R_3^n-\Delta R_3\right)-2\phi\left(R_1^l, R_2^m, R_3^n\right)}{\left(\Delta R_3\right)^2}.
\end{aligned}
\tag{5.5}
$$

Since Eq. (5.5) involves only the undeformed coordinates, we define the discretized order parameter value of the undeformed configuration at each grid point as

$$\phi_{l,m,n} \equiv \phi\left(R_1^l, R_2^m, R_3^n\right) \tag{5.6}$$

to rewrite Eq. (5.5) as

$$
\begin{aligned}
\nabla^2_{\mathbf{R}}\phi_{l,m,n} \approx &\frac{\phi_{l+1,m,n}+\phi_{l-1,m,n}-2\phi_{l,m,n}}{\left(\Delta R_1\right)^2}+\frac{\phi_{l,m+1,n}+\phi_{l,m-1,n}-2\phi_{l,m,n}}{\left(\Delta R_2\right)^2} \\
&+\frac{\phi_{l,m,n+1}+\phi_{l,m,n-1}-2\phi_{l,m,n}}{\left(\Delta R_3\right)^2}.
\end{aligned}
\tag{5.7}
$$

Since this expression requires solely the grid values of ϕ, $\phi_{l,m,n}$, its evaluation does not involve interpolations. Therefore, the evaluation of this expression is more computationally efficient than those that require interpolations.

The position vector associated with a material point in the undeformed configuration, $\left(R_1^l, R_2^m, R_3^n\right)$, will be mapped to the corresponding position after deformation, $\left(r_1^l, r_2^m, r_3^n\right)$, via

$$\begin{bmatrix} r_1^l \\ r_2^m \\ r_3^n \end{bmatrix} = \boldsymbol{\alpha}_t \begin{bmatrix} R_1^l \\ R_2^m \\ R_3^n \end{bmatrix}. \tag{5.8}$$

Thus, the equations corresponding to Eq. (5.4) for deformed coordinates are

$$\begin{aligned}
r_1^l\left(R_1^0, R_2^m, R_3^n\right) &= r_1^0\left(R_1^0, R_2^m, R_3^n\right) + l\Delta r_1,\\
r_2^m\left(R_1^l, R_2^0, R_3^n\right) &= r_2^0\left(R_1^l, R_2^0, R_3^n\right) + m\Delta r_2,\\
r_3^n\left(R_1^l, R_2^m, R_3^0\right) &= r_3^0\left(R_1^l, R_2^m, R_3^0\right) + n\Delta r_3, \qquad (5.9)
\end{aligned}$$

where the grid spacing Δr_i is given by

$$\Delta r_1 = \alpha_{11}\Delta R_1, \quad \Delta r_2 = \alpha_{22}\Delta R_2, \quad \Delta r_3 = \alpha_{33}\Delta R_3. \qquad (5.10)$$

Once again, using the notation above, the Laplacian of the order parameter of the deformed state can be approximated with a second-order central-difference scheme by

$$\begin{aligned}
\nabla_{\mathbf{r}}^2\phi_{l,m,n} \approx& \frac{\phi_t^D\left(r_1^l+\Delta r_1, r_2^m, r_3^n\right) + \phi_t^D\left(r_1^l-\Delta r_1, r_2^m, r_3^n\right) - 2\phi_{l,m,n}^D}{\left(\Delta r_1\right)^2}\\
&+ \frac{\phi_t^D\left(r_1^l, r_2^m+\Delta r_2, r_3^n\right) + \phi_t^D\left(r_1^l, r_2^m-\Delta r_2, r_3^n\right) - 2\phi_{l,m,n}^D}{\left(\Delta r_2\right)^2}\\
&+ \frac{\phi_t^D\left(r_1^l, r_2^m, r_3^n+\Delta r_3\right) + \phi_t^D\left(r_1^l, r_2^m, r_3^n-\Delta r_3\right) - 2\phi_{l,m,n}^D}{\left(\Delta r_3\right)^2}, \qquad (5.11)
\end{aligned}$$

where we have defined the discretized order parameter value of the deformed configuration at each grid point as

$$\phi_{l,m,n}^D \equiv \phi_t^D\left(r_1^l, r_2^m, r_3^n\right). \qquad (5.12)$$

For isotropic and biaxial deformations, the neighboring values of $\phi_t^D\left(r_1^l, r_2^m, r_3^n\right)$ can also be replaced by discretized order parameter values that exist at each grid point,

$$\begin{aligned}
\phi_t^D\left(r_1^l \pm \Delta r_1, r_2^m, r_3^n\right) &= \phi_{l\pm1,m,n}^D \\
\phi_t^D\left(r_1^l, r_2^m \pm \Delta r_2, r_3^n\right) &= \phi_{l,m\pm1,n}^D \\
\phi_t^D\left(r_1^l, r_2^m, r_3^n \pm \Delta r_3\right) &= \phi_{l,m,n\pm1}^D. \qquad (5.13)
\end{aligned}$$

On the other hand, for simple-shear deformation, as we will show later, only two of the three relationships in Eq. (5.13) are valid. Consequently, it is not possible to express the discretization of the Laplacian in Eq. (5.11) solely in terms of deformed-state discretized order parameter values resulting from the mapping of the grid points from the undeformed coordinates.

5.2 Method 1: Conventional Method for Applying Deformation

In this section, we describe the conventional method for applying deformation, which involves a mapping of undeformed coordinates to deformed coordinates [24, 53, 62]. This method, hereafter referred to as CM, has a deformed-state free energy

$$\mathcal{F}_{\text{def}} = \int_{\Omega(\xi)} f\left(\phi_t^D(\mathbf{r}), \nabla_{\mathbf{r}}^2\right) d\mathbf{r}, \qquad (5.14)$$

where f denotes the FED, $\nabla_{\mathbf{r}}^2 = \sum_{i=1}^3 \partial^2/\partial r_i^2$, and $\Omega(\xi)$ denotes the deformed unit cell. Note that we have explicitly written out the dependence of the PFC FED on the Laplacian operator. We will continue to use this notation for the remainder of this chapter to highlight the differences between the three methods. For an undeformed cubic unit cell with a side length of a, the deformed-state free energy for isotropic, biaxial, and simple-shear deformations are

$$\begin{aligned}
\mathcal{F}_{\text{iso}} &= \int_0^{a(1+\xi)} \left(\int_0^{a(1+\xi)} \left(\int_0^{a(1+\xi)} f\left(\phi^D_{\text{iso}}(\mathbf{r}), \nabla^2_{\mathbf{r}}\right) dr_1 \right) dr_2 \right) dr_3 \\
\mathcal{F}_{\text{bi}} &= \int_0^{a} \left(\int_0^{a(1-\xi)} \left(\int_0^{a(1+\xi)} f\left(\phi^D_{\text{bi}}(\mathbf{r}), \nabla^2_{\mathbf{r}}\right) dr_1 \right) dr_2 \right) dr_3 \\
\mathcal{F}_{\text{sh}} &= \int_0^{a} \left(\int_0^{a} \left(\int_{-\xi r_2}^{a-\xi r_2} f\left(\phi^D_{\text{sh}}(\mathbf{r}), \nabla^2_{\mathbf{r}}\right) dr_1 \right) dr_2 \right) dr_3, \qquad (5.15)
\end{aligned}$$

respectively, where we note that the integration limit for simple-shear deformation is over a non-rectangular domain, necessitating the expression for the integration limit to be dependent on r_2.

CM is straightforward to implement for deformations that do not skew the computational domain, such as isotropic and biaxial deformations, because the discretization of the Laplacian operator only involves values that lie on the computational grid points. However, for deformations that do skew the computational domain, such as the simple-shear deformation considered here, the discretization of the Laplacian operator involves values that must be interpolated from values on the computational grid point, which we refer to as resampling. In the following paragraphs we employ Eq. (5.11) and the notation of Section 5.1.2 to illustrate why resampling is required for simple-shear deformation, but not for isotropic and biaxial deformations.

We will first consider isotropic and biaxial deformations, where the relationship between deformed and undeformed coordinates is given by

$$r_1^l = \alpha_{11} R_1^l, \quad r_2^m = \alpha_{22} R_2^m, \quad r_3^n = \alpha_{33} R_3^n \qquad (5.16)$$

because only the diagonal elements of $\boldsymbol{\alpha}_t$ are nonzero. Using Eq. (5.10), the values of

ϕ_t^D at neighboring points along the r_1 coordinate in Eq. (5.11) can be expressed as

$$\begin{aligned}\phi_t^D\left(r_1^l \pm \Delta r_1, r_2^m, r_3^n\right) &= \phi_t^D\left(\alpha_{11}(R_1^l \pm \Delta R_1), \alpha_{22}R_2^m, \alpha_{33}R_3^n\right)\\ &= \phi_t^D\left(\alpha_{11}R_1^{l+1}, \alpha_{22}R_2^m, \alpha_{33}R_3^n\right)\\ &= \phi_{l\pm 1,m,n}^D. \end{aligned} \tag{5.17}$$

Similarly, the values of ϕ_t^D at the neighboring points along the r_2 and r_3 coordinates are

$$\begin{aligned}\phi_t^D\left(r_1^l, r_2^m \pm \Delta r_2, r_3^n\right) &= \phi_{l,m\pm 1,n}^D\\ \phi_t^D\left(r_1^l, r_2^m, r_3^n \pm \Delta r_3\right) &= \phi_{l,m,n\pm 1}^D. \end{aligned} \tag{5.18}$$

Combining Eqs. (5.17) and (5.18), the discretization of the Laplacian in Eq. (5.11) becomes

$$\begin{aligned}\nabla_{\mathbf{r}}^2\phi_{l,m,n}^D \approx &\frac{\phi_{l+1,m,n}^D + \phi_{l-1,m,n}^D - 2\phi_{l,m,n}^D}{(\Delta r_1)^2} + \frac{\phi_{l,m+1,n}^D + \phi_{l,m-1,n}^D - 2\phi_{l,m,n}^D}{(\Delta r_2)^2}\\ &+ \frac{\phi_{l,m,n+1}^D + \phi_{l,m,n-1}^D - 2\phi_{l,m,n}^D}{(\Delta r_3)^2}, \end{aligned} \tag{5.19}$$

where the discretization of the Laplacian of the order parameter values involve only values that lie on the grid points of the computational domain. A comparison of Eqs. (5.7) and (5.19) demonstrates that isotropic and biaxial deformations effectively change the grid spacing, where the choice of $\boldsymbol{\alpha}_t$ affects the magnitude of Δr_i (see Eq. (5.10)).

Schematics of the positions of grid points in two dimensions for an undeformed coordinate (Eq. (5.7)) and an isotropically deformed coordinate (Eq. (5.19)) are shown in Figs. 5.1(a) and (b), respectively. Each dot represents a computational grid point in the respective discretized coordinate system. Relative to the center grid point labeled with C, the grid points directly above $(m+1)$ and below $(m-1)$ are labeled T and B, respectively, while the grid points directly to the left $(l-1)$ and right $(l+1)$ are labeled L and R, respectively. As seen in Figs. 5.1(a) and (b), the discretization stencil of the Laplacian operator for the undeformed and isotropically deformed states solely involve values of the discretized order parameter that lie on a grid point, and therefore resampling is not required. The only difference between the undeformed and isotropically deformed state is the spacing between the grid points.

Next we consider simple-shear deformation where the relationship between the deformed and undeformed coordinates is

$$r_1^l = R_1^l - \xi R_2^m, \quad r_2^m = R_2^m, \quad r_3^n = R_3^n. \tag{5.20}$$

Thus, the neighboring values that lie on the computational grid points along the r_2 coordinate, $\phi^D_{l,m\pm1,n}$, are

$$\begin{aligned} \phi^D_{l,m\pm1,n} &= \phi^D_{\text{sh}}\left(r_1^l, r_2^{m\pm1}, r_3^n\right) \\ &= \phi^D_{\text{sh}}\left(R_1^l - \xi R_2^{m\pm1}, R_2^{m\pm1}, R_3^n\right) \\ &= \phi^D_{\text{sh}}\left(R_1^l - \xi(R_2^m \pm \Delta R_2), R_2^m \pm \Delta R_2, R_3^n\right), \end{aligned} \tag{5.21}$$

while the values in the discretization of the Laplacian term along the r_2 coordinate are

$$\phi^D_{\text{sh}}\left(r_1^l, r_2^m \pm \Delta r_2, r_3^n\right) = \phi^D_{\text{sh}}\left(R_1^l - \xi R_2^m, R_2^m \pm \Delta R_2, R_3^n\right). \tag{5.22}$$

Since Eq. (5.22) cannot simply be expressed as Eq. (5.21), the discretization of the Laplacian term along the r_2 coordinate for simple-shear deformation requires interpolation from $\phi^D_{l,m\pm1,n}$ to $\phi^D_{\text{sh}}\left(r_1^l, r_2^m \pm \Delta r_2, r_3^n\right)$.

A schematic of the two-dimensional discretization of the Laplacian operator for simple-shear deformation is illustrated in Fig. 5.1(c). As seen in the figure, the grid points directly above $(m+1)$ and below $(m-1)$ the grid point C, labeled T and B, respectively, do not coincide with the discretization stencil of the Laplacian operator ($\mathrm{I_T}$ and $\mathrm{I_B}$). Therefore, resampling to $\mathrm{I_T}$ and $\mathrm{I_B}$ is required.

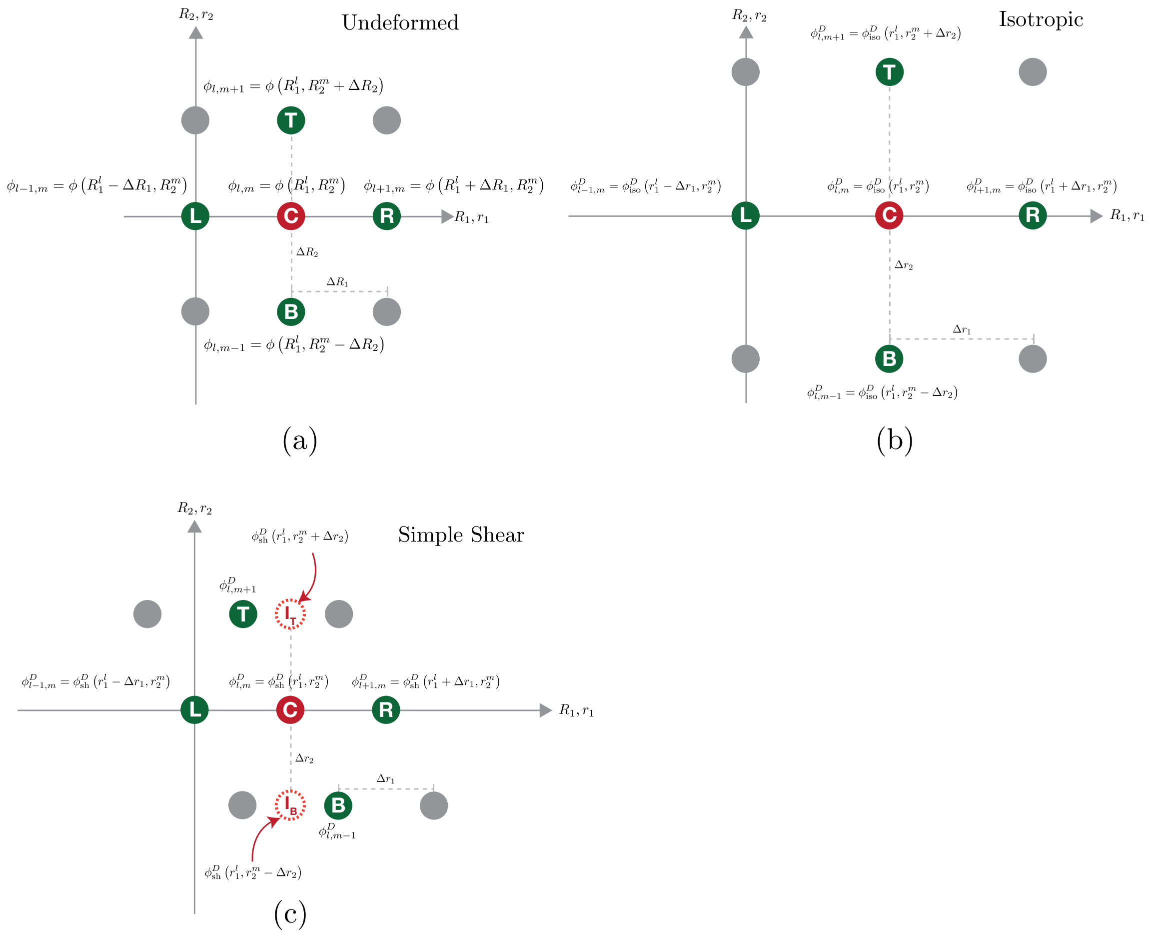

Figure 5.1: A two-dimensional schematic of the material points in (a) the undeformed configuration and deform configuration due to (b) isotropic and (c) simple-shear deformations. Each dot represents a computational grid point. Relative to the center grid point labeled with C, the grid points directly above $(m+1)$, below $(m-1)$, to the right $(l+1)$, and to the left $(l-1)$ are labeled T, B, R, and L, respectively. The points $\mathrm{I_T}$ and $\mathrm{I_B}$ in (c) mark the position to which the order parameter values need to be interpolated for the discretization of the Laplacian term.

5.3 Method 2: Transformation of Laplacian Operator

In this section, we describe a method for evaluating a deformed-state PFC free energy when ϕ_t^D is expressed in terms of undeformed coordinates, $\mathbf{R}$, i.e., $\phi_t^D(\mathbf{R})$. This method, hereafter referred to as LM (for Laplacian mapping), does not require resampling for all types of deformation. In order to describe deformation when the deformed-state FED is in terms of $\phi_t^D(\mathbf{R})$, the Laplacian operator in the PFC FED must be transformed instead to account for the coordinate mapping. A relationship between the derivatives in terms of deformed coordinates, r_i, to those with respect to undeformed coordinates, R_i, can be obtained via the chain rule,

$$\frac{\partial}{\partial r_m} = \frac{\partial R_i}{\partial r_m}\frac{\partial}{\partial R_i} = \alpha_{im}^{-1}\frac{\partial}{\partial R_i}. \tag{5.23}$$

Using Eq. (5.23), the Laplacian operator of the deformed system is

$$\nabla_t^2 = \frac{\partial}{\partial r_m}\left(\frac{\partial}{\partial r_m}\right) = \alpha_{im}^{-1}\frac{\partial}{\partial R_i}\left(\alpha_{jm}^{-1}\frac{\partial}{\partial R_j}\right) = \alpha_{im}^{-1}\alpha_{jm}^{-1}\frac{\partial}{\partial R_i}\frac{\partial}{\partial R_j}, \tag{5.24}$$

where α_{jm}^{-1} is independent of R_i for affine transformations, and the subscript t denotes the type of deformation.

Combining Eqs. (5.2) and (5.24), the Laplacian operator for isotropic, biaxial, and simple-shear deformations are

$$\begin{aligned}
\nabla_{\text{iso}}^2 &= \frac{1}{(1+\xi)^2}\frac{\partial^2}{\partial R_1^2} + \frac{1}{(1+\xi)^2}\frac{\partial^2}{\partial R_2^2} + \frac{1}{(1+\xi)^2}\frac{\partial^2}{\partial R_3^2} \\
\nabla_{\text{bi}}^2 &= \frac{1}{(1+\xi)^2}\frac{\partial^2}{\partial R_1^2} + \frac{1}{(1-\xi)^2}\frac{\partial^2}{\partial R_2^2} + \frac{\partial^2}{\partial R_3^2} \\
\nabla_{\text{sh}}^2 &= (1+\xi^2)\frac{\partial^2}{\partial R_1^2} + 2\xi\frac{\partial^2}{\partial R_1 \partial R_2} + \frac{\partial^2}{\partial R_2^2} + \frac{\partial^2}{\partial R_3^2},
\end{aligned} \tag{5.25}$$

respectively. Note that, the discretization of the Laplacian operators for isotropic and biaxial deformations are identical to Eq. (5.19), where $r_i = (1+\xi)R_i$ for isotropic deformation, and $r_1 = (1+\xi)R_1$, $r_2 = (1-\xi)R_2$, and $r_3 = R_3$ for biaxial deformation. Furthermore, since LM involves a FED that is defined on undeformed coordinates (and on the undeformed domain), the integral must be written in terms of the undeformed coordinates. In general, the integral over the deformed volume can be written in terms of the integral taken in the undeformed coordinates as

$$\int\int\int_{\Omega(\xi)} dr_1 dr_2 dr_3 = J_t \int\int\int_{\Omega'} dR_1 dR_2 dR_3, \tag{5.26}$$

where J_t is independent of R_i, and Ω' denotes the reference undeformed unit cell. Combining Eqs. (5.24) and (5.26), the free energy of a deformed system for LM is

$$\mathcal{F}_{\mathrm{def}} = J_t \int_{\Omega'} f\left(\phi_t^D(\mathbf{R}), \nabla_t^2\right) d\mathbf{R}. \tag{5.27}$$

LM does not require resampling for all types of deformation because the discretized Laplacian in LM only involves order parameter values that lie on the computational grid (i.e., $\phi^D_{l,m,n}$). To demonstrate this fact, consider the discretized Laplacian for simple-shear deformation, $\nabla^2_{\mathrm{sh}}\phi^D_t(\mathbf{R}) = \nabla^2_{\mathrm{sh}}\phi^D_{l,m,n}$,

$$\begin{aligned}\nabla^2_{\mathrm{sh}}\phi^D_{l,m,n} \approx &(1+\xi^2)\frac{\phi^D_{l+1,m,n} + \phi^D_{l-1,m,n} - 2\phi^D_{i,j,k}}{(\Delta R_1)^2}\\ &+ 2\xi\frac{\phi^D_{i+1,j+1,k} - \phi^D_{i+1,j-1,k} - \phi^D_{i-1,j+1,k} + \phi^D_{i-1,j-1,k}}{4\Delta R_1 \Delta R_2}\\ &\frac{\phi^D_{l,m+1,n} + \phi^D_{l,m-1,n} - 2\phi^D_{i,j,k}}{(\Delta R_2)^2} + \frac{\phi^D_{l,m,n+1} + \phi^D_{l,m,n-1} - 2\phi^D_{i,j,k}}{(\Delta R_3)^2},\end{aligned} \tag{5.28}$$

where all points involved in the Laplacian lies on a computational grid point.

5.4 Method 3: Fourier Space Formulation

In this section, we describe a numerical method for implementing deformation when the PFC free energy is expressed in Fourier space. This method, hereafter referred to as FM, is necessary when the PFC FED only has a closed-form FED expression in Fourier space, but not in real space, e.g., the structural PFC (XPFC) [55] and the rational-function fit (RFF) PFC [69] formulations. An alternative numerical method for implementing shear-type deformation in Fourier space, which involves the interpolation of order parameter values, was described in Ref. [58]. In this method, the deformed free energy can only be calculated when the deformed configuration is periodic. As a result, this method requires a large system size when applying shear deformations that involve small strains, and is impractical for three-dimensional calculations.

FM is formulated based on the similarity theorem of the Fourier transform [85], where deformation is described by shifts in the wave vector [86, 87]. As shown in Appendix B, the mapping from undeformed to deformed coordinates in reciprocal space is given by $\boldsymbol{\alpha}_t^{-T}$, which is the transpose of the inverse of $\boldsymbol{\alpha}_t$. Therefore, the deformed-state free energy in Eq. (5.14) becomes

$$\begin{aligned}\mathcal{F}_{\text{def}} &= \int_{\Omega'} \mathscr{F}^{-1}\left[\hat{f}\left(\hat{\phi}_t^D(\mathbf{k}'), (\mathbf{k}')^2\right)\right] J_t d\mathbf{R} \\ &= \int_{\Omega'} \mathscr{F}^{-1}\left[\hat{f}\left(\hat{\phi}_t^D(\boldsymbol{\alpha}_t^{-T}\cdot\mathbf{k}), \left(\boldsymbol{\alpha}_t^{-T}\cdot\mathbf{k}\right)^2\right)\right] J_t d\mathbf{R}, \end{aligned} \tag{5.29}$$

where $\mathbf{k}'$ denotes the deformed coordinates in reciprocal space, the notation $\mathscr{F}^{-1}[g(\mathbf{k})]$ indicates the inverse Fourier transform operation of $g(\mathbf{k})$, the hat symbols denote quantities in Fourier space, and the volume change of the unit cell due to mapping is accounted for by J_t. For the set of deformations we consider, $\boldsymbol{\alpha}_t^{-T}$ is given by

$$\boldsymbol{\alpha}_{\text{iso}}^{-T} = \begin{bmatrix} \frac{1}{1+\xi} & 0 & 0 \\ 0 & \frac{1}{1+\xi} & 0 \\ 0 & 0 & \frac{1}{1+\xi} \end{bmatrix}, \quad \boldsymbol{\alpha}_{\text{bi}}^{-T} = \begin{bmatrix} \frac{1}{1+\xi} & 0 & 0 \\ 0 & \frac{1}{1-\xi} & 0 \\ 0 & 0 & 1 \end{bmatrix}, \quad \boldsymbol{\alpha}_{\text{sh}}^{-T} = \begin{bmatrix} 1 & 0 & 0 \\ \xi & 1 & 0 \\ 0 & 0 & 1 \end{bmatrix}. \tag{5.30}$$

Equation (5.30) can be used to rewrite the Fourier-space representation of the

Laplacian operator,

$$\hat{L}_{\mathbf{k}} = -\left(k_1^2 + k_2^2 + k_3^2\right), \tag{5.31}$$

as

$$\begin{aligned}
\hat{L}_{\rm iso} &= -\frac{1}{(1+\xi)^2}\left[k_1^2 + k_2^2 + k_3^2\right] \\
\hat{L}_{\rm bi} &= -\frac{1}{(1+\xi)^2}\left[k_1^2 + k_2^2\right] + k_3^2 \\
\hat{L}_{\rm sh} &= -\left[(1+\xi^2)k_1^2 + k_2^2 + k_3^2 + 2\xi k_1 k_2\right],
\end{aligned} \tag{5.32}$$

for isotropic, biaxial, and simple-shear deformations, respectively, and k_1, k_2, and k_3 are the undeformed coordinate values in real space.

5.5 Comparison of Methods

In this section, we compare the accuracy and efficiency of CM, LM, and FM for the numerical evaluation of the PFC FED in Eq. (2.4) for a deformed unit cell. Since unit-cell deformations are employed to determine elastic constants in the PFC model [53, 55, 62], we will compare the values of

$$\mathcal{Q} \equiv \left.\frac{\partial^2 f}{\partial \xi^2}\right|_{\bar{\phi}}^{\xi=0}, \tag{5.33}$$

which are directly related to elastic constants [53]. The subscript $\bar{\phi}$ denotes that the average of ϕ is held constant and the superscript $\xi = 0$ denotes that $\mathcal{Q}$ is evaluated at the undeformed state.

For our calculations, we consider a single unit cell of the body-centered-cubic (*bcc*) structure, and thus the order parameter of the undeformed state can be expressed analytically in terms of the undeformed coordinates when a one-mode approximation is assumed [24]:

$$\begin{aligned}\phi_{\text{one}}(\mathbf{R}) &= \cos\left(\frac{2\pi R_1}{a}\right)\cos\left(\frac{2\pi R_2}{a}\right)+\cos\left(\frac{2\pi R_1}{a}\right)\cos\left(\frac{2\pi R_3}{a}\right)\\ &+ \cos\left(\frac{2\pi R_2}{a}\right)\cos\left(\frac{2\pi R_3}{a}\right), \end{aligned} \tag{5.34}$$

where a is the edge length of a unit cell.

For the purpose of this chapter, which focuses on the demonstration and validation of the proposed methods, we simply assume that ϕ is mapped to the deformed coordinates under deformation (i.e., without numerical relaxation). Such assumption is typically made when a one-mode approximation is assumed and the FED calculations are performed analytically or semianalytically [24, 62]. In this case,

$$\phi_t^D(\mathbf{r}) = \phi_{\text{one}}(\boldsymbol{\alpha}^{-1}\cdot\mathbf{r}) \tag{5.35}$$

and

$$\phi_t^D(\mathbf{R}) = \phi_{\text{one}}(\mathbf{R}) \tag{5.36}$$

for the free energy evaluations in Eqs. (5.14) and (5.27), respectively. While this assumption is sufficient for the demonstration and comparisons of the methods, it should be noted that ϕ_t^D must be relaxed in an actual calculation of elastic constants.

The accuracy of the numerical methods is measured by comparing the values of $\mathcal{Q}$ determined from numerical and analytical evaluations of the deformed-state PFC free energy, $\mathcal{Q}_{\text{numerical}}$ and $\mathcal{Q}_{\text{analytical}}$, respectively. Specifically, we consider the percent error of $\mathcal{Q}$, $\%e_{\mathcal{Q}}$,

$$\%e_{\mathcal{Q}} = \frac{|\mathcal{Q}_{\text{analytical}} - \mathcal{Q}_{\text{numerical}}|}{|\mathcal{Q}_{\text{analytical}}|}\times 100\%, \tag{5.37}$$

for isotropic, biaxial, and simple-shear deformations. To measure efficiency, we compare how $\%e_{\mathcal{Q}}$ decreases as the number of grid points in each direction, N, increases for the different methods.

The values of $\%e_{\mathcal{Q}}$ as a function of N is plotted in Fig. 5.2 for CM, LM, and FM for different deformations. The calculations in Fig. 5.2 are performed on a single unit cell given by Eq. (5.34) with $a = 2\pi\sqrt{2}$. Cubic interpolation [88] was implemented to evaluate the PFC FED for CM using the interp3 function of MATLAB R2013b (version 8.2.0.701). The PFC FED expressions with $\tilde{\epsilon} = 0.0923$ [53, 78] were numerically integrated using a three-dimensional trapezoidal rule. A single curve is plotted for CM and LM for isotropic and biaxial deformations because their implementations are identical in these methods. Additionally, only a single curve is plotted for FM because $\%e_{\mathcal{Q}} < 0.001\%$ for all deformations and values of N considered. As expected, $\%e_{\mathcal{Q}}$ decreases as N increases for all methods.

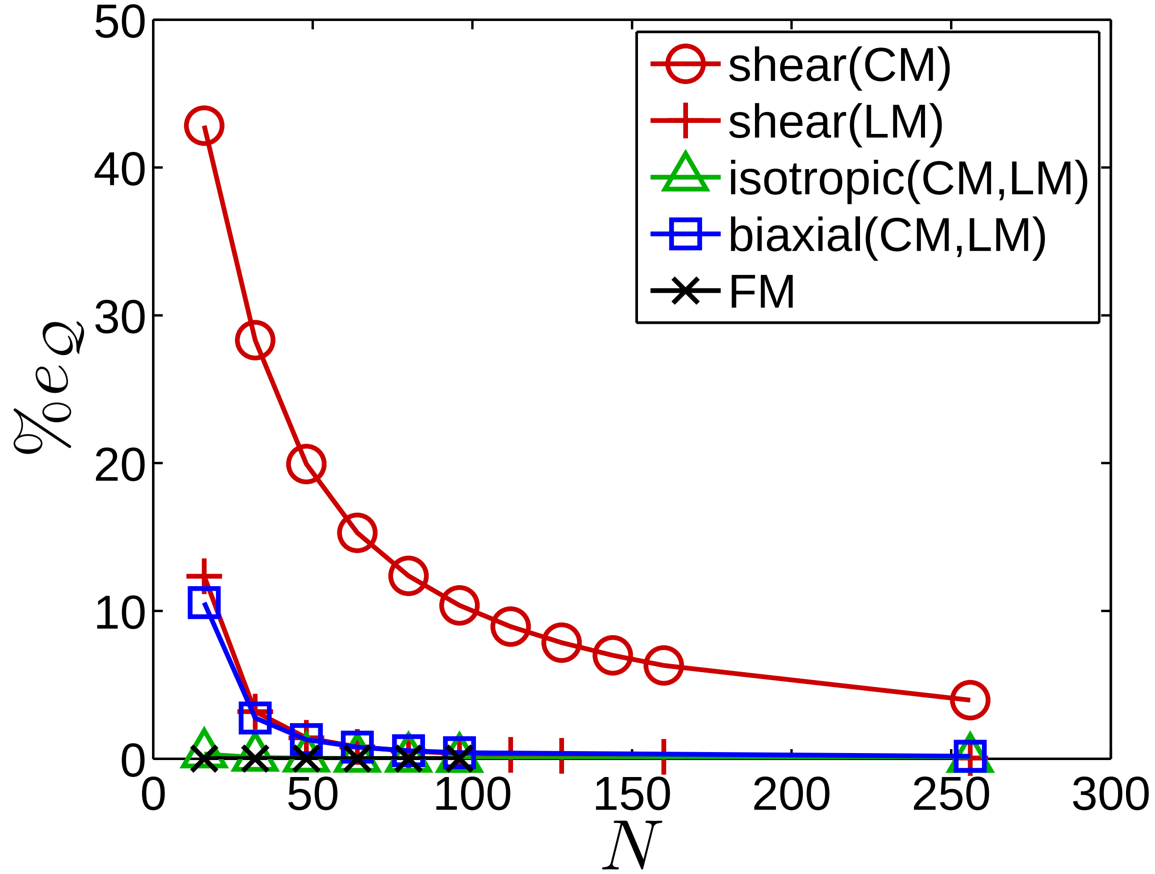

Figure 5.2: Percent error of $\mathcal{Q}$ as a function of N for CM, LM, and FM for isotropic, biaxial, and simple-shear deformations.

FM employs spectral differentiation (see Eq. (5.32)) to evaluate the PFC free energy and therefore exhibits spectral accuracy for smooth functions that have a rapidly decaying Fourier transform [89]. Since the calculations in Fig. 5.2 are for a one-mode approximation, which has a single wave mode in Fourier space, the results of FM are essentially identical to the analytical solution.

CM is fairly accurate for isotropic deformation with $\%e_{\mathcal{Q}} < 0.4\%$ for $N = 16$ and is less accurate for biaxial and simple-shear deformations. For biaxial deformation, $\%e_{\mathcal{Q}}$ drops below 1% for $N = 64$, while for simple-shear deformation $\%e_{\mathcal{Q}} > 3\%$ even at the highest resolution of $N = 256$. LM is identical to CM for isotropic and biaxial deformations. However, LM is significantly more accurate for simple-shear deformation where $\%e_{\mathcal{Q}}$ drops below 1% for $N = 64$ because the interpolation required for applying shear deformation is eliminated. Although the interpolation error in CM may be reduced by experimenting with various interpolation schemes [88], a thorough investigation is beyond the scope of this work.

Since $\mathcal{Q}$ is directly related to the values of elastic constants in the PFC model, the results in Fig. 5.2 reflect the errors that are expected when calculating elastic constants using these methods. FM is the most efficient method when the PFC free energy is expressed in Fourier space because FM requires significantly less resolution than CM or LM to accurately evaluate $\mathcal{Q}$. In the case where a real space evaluation of $\mathcal{Q}$ is necessary, LM is more accurate and efficient than CM.

5.6 Elastic Constants and Bulk Modulus of EOF-PFC Model

In this section, we employ FM to implement the thermodynamic relationships developed in Chapter IV to calculate the elastic constants and solid bulk modulus of two *bcc* structures that are stabilized by the EOF-PFC model at two different pressure states. The first structure is at the solid coexistence density, which corresponds to a non-zero pressure, while the second structure is at a zero-pressure state. In both cases, we calculate the elastic constants C_{11}, C_{12}, and C_{44}, as well as the solid bulk modulus, $\mathcal{K}^c$.

5.6.1 Elastic Constants and Bulk Modulus for *bcc* Structure at Solid Coexistence Density

To determine the elastic constants and bulk modulus of a *bcc* structure stabilized by the EOF-PFC model, FM is employed to calculate the EOF-PFC free energy (Eq. (2.20)) for different deformations (i.e., as a function of ξ). At each value of ξ, the free energy is relaxed according to Eq. (3.1) for the parameters listed in table 2.1, while $\bar{n}$ is held constant. However, the value of $\bar{n}$ may change during deformation (i.e., for different values of ξ) depending on the type of deformation by

$$\bar{n} = \frac{\left(\frac{\bar{n}'\rho_0 + \rho_0}{J_t(\xi)} - \rho_0\right)}{\rho_0} = \frac{\bar{n}' + 1}{J_t} - 1, \tag{5.38}$$

where $\bar{n}'$ is held constant to keep the number of atoms, N_A^c, and lattice sites, N_L^c, fixed, while J_t may be a function of ξ, depending on the type of deformation (see Eq. (5.3)). For elastic constants at the coexistence density $\bar{n}'$ is set to $\bar{n}_s = 9.17 \times 10^{-3}$ (see Section 3.6.1).

The values of $\mathcal{H}_{\text{iso}}$, $\mathcal{H}_{\text{bi}}$, and $\mathcal{H}_{\text{sh}}$, which are used to determine C_{11}, C_{12}, and C_{44}, as well as $\mathcal{K}^c$, are then calculated from the second derivative of the EOF-PFC free energy with respect to ξ for isotropic, biaxial, and simple-shear deformations, respectively (see Section 4.3). As seen in Eq. (4.27), the calculation of $\mathcal{H}_t$ requires a knowledge of the pressure, P^0, and bulk modulus, $\mathcal{K}^0$, of the liquid reference state. For the EOF-PFC model considered here, $\mathcal{K}^0 = 50\rho_0 k_B T$ because $\rho_0 \hat{C}^{(2)}(0) = -49$ [54], and P^0 is set to zero because the EAM-MD potential used to calculate the two-body DCF of *bcc* Fe [20] of Ref. [54] was fitted to a system at zero pressure.

The non-dimensionalized EOF-PFC FEDs as a function of ξ for isotropic, biaxial, and simple-shear deformations are plotted in Figs. 5.3, 5.4, and 5.5, respectively, and the dashed red curves are plots of a polynomial that is fitted to the simulation results. For isotropic and biaxial deformations, the value of $\bar{n}$ corresponding to each value of ξ is different, where $\bar{n} = \bar{n}_s = 9.17 \times 10^{-3}$ at $\xi = 0$. On the other hand, for simple-shear deformation, $\bar{n} = \bar{n}_s = 9.17 \times 10^{-3}$ for all values of ξ because the volume does not change during deformation. The values of $\mathcal{H}_{\text{iso}}$, $\mathcal{H}_{\text{bi}}$, and $\mathcal{H}_{\text{sh}}$, which are determined by evaluating the second derivative of the corresponding curves at $\xi = 0$ (undeformed state and marked by green square), are listed in Table 5.1. The hydrostatic pressure of the crystalline phase, P^c, is determined from evaluating the first derivative of Fig. 5.3 at $\xi = 0$ and multiplying by -1/3 (see Eq. (4.29)), and is also listed in Table 5.1.

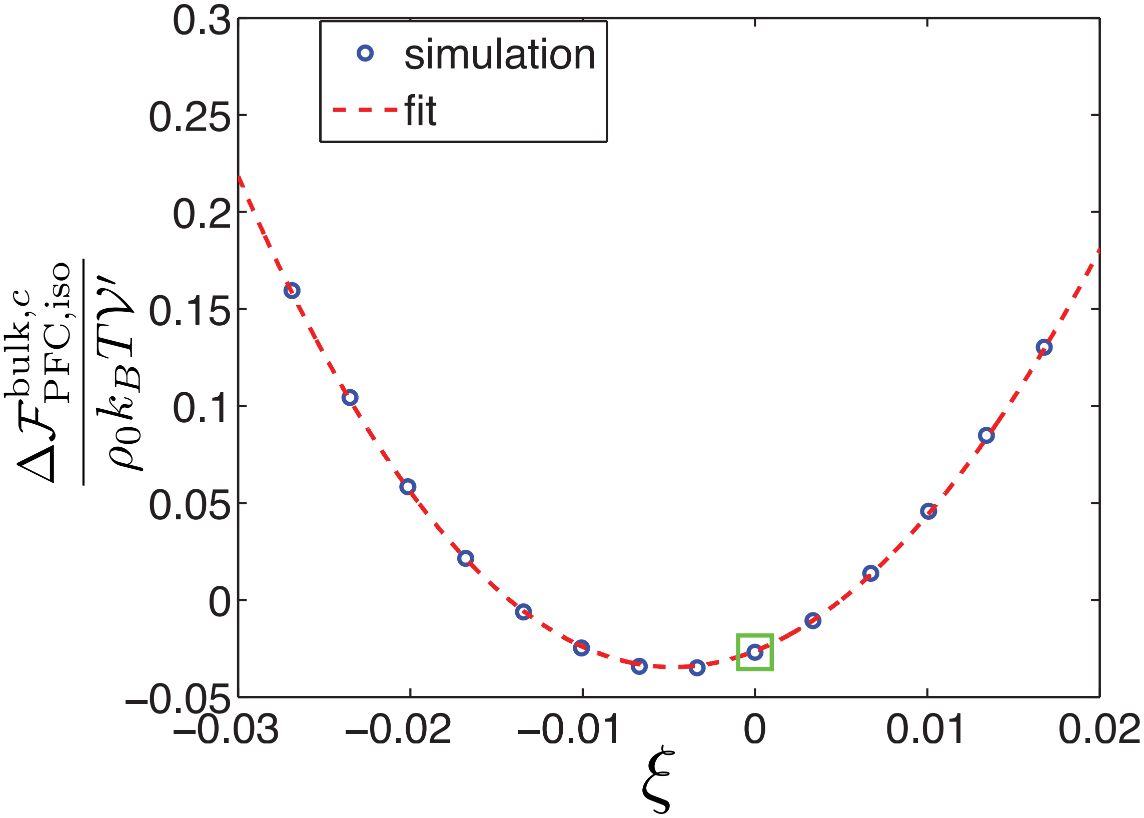

Figure 5.3: Plot of non-dimensionalized EOF-PFC FED as a function of ξ for isotropic deformation. All points have the same value of $\bar{n}'$ (N^c_A held constant), while $\bar{n}$ varies. The values calculated using FM (blue dots) are fitted with a third-order polynomial function (red dashed curve): $-910.6\xi^3 + 360.8\xi^2 + 3.480\xi - 0.0263$. The value of $\mathcal{H}_{\text{iso}}$ is 2 × the coefficient of ξ^2 and the pressure is -1/3 × the coefficient of ξ. The system corresponding to $\xi = 0$ has $\bar{n} = \bar{n}_s = 9.17 \times 10^{-3}$ and is marked with a green square.

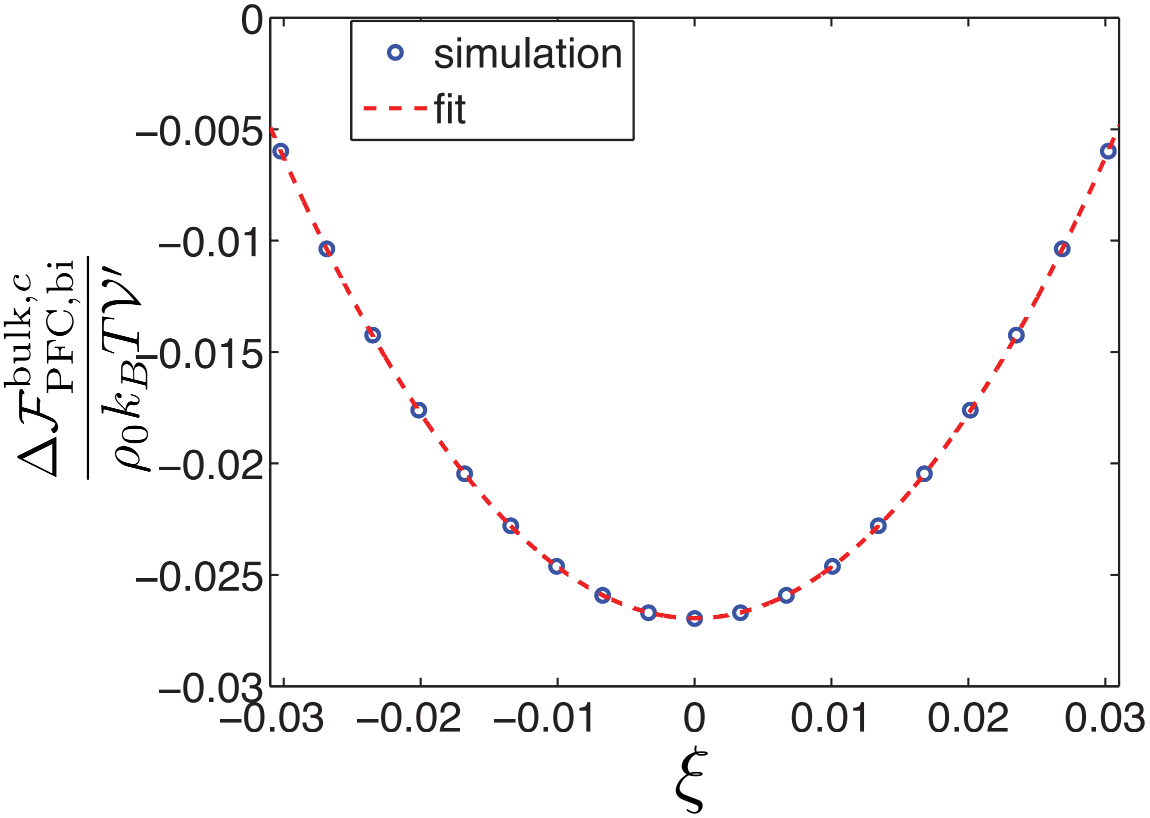

Figure 5.4: Plot of non-dimensionalized EOF-PFC FED as a function of ξ for biaxial deformation. All points have the same value of $\bar{n}'$ (N_A^c held constant), while $\bar{n}$ varies. The values calculated using FM (blue dots) are fitted with a third-order polynomial (red dashed curve): $0.800\xi^3 + 22.96\xi^2 - 4.134 \times 10^{-4}\xi - 0.0269$. The value of $\mathcal{H}_{\mathrm{bi}}$ is 2 × the coefficient of ξ^2.

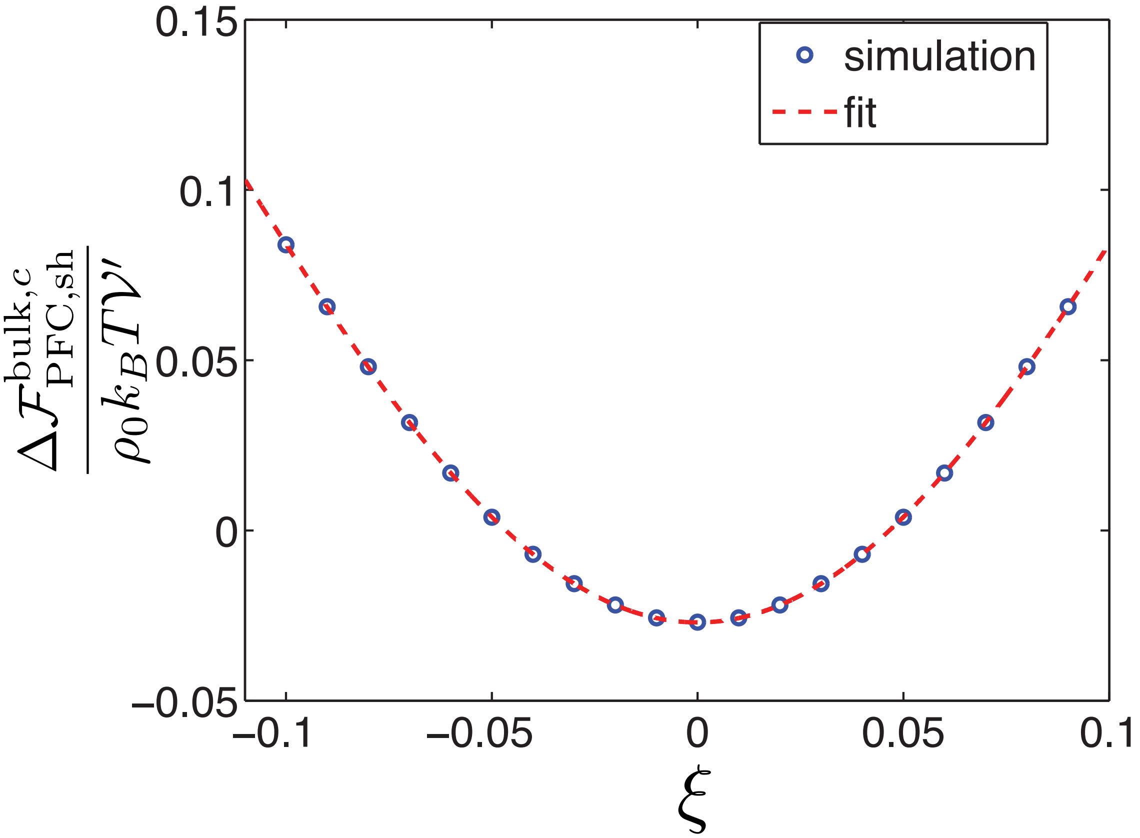

Figure 5.5: Plot of EOF-PFC FED as a function of ξ for simple-shear deformation. All points have the same value of $\bar{n}'$ (N_A^c held constant), while $\bar{n}$ varies. The values calculated using FM (blue dots) are fitted with a fourth-order polynomial (red dashed curve): $-169.0\xi^4 + 0.1838\xi^3 + 12.81\xi^2 - 7.775 \times 10^{-4}\xi - 0.0270$. The value of $\mathcal{H}_{\text{sh}}$ is 2 × the coefficient of ξ^2.

The values of C_{11}, C_{12}, and C_{44} calculated from $\mathcal{H}_t$ in Figs 5.3, 5.4, and 5.5, as well as $\mathcal{K}^c = (C_{11} + 2C_{12} + P^c)/3$ (see Eq. (4.33)) are listed in table 5.1. These values correspond to $\bar{n} = \bar{n}_s = 9.17 \times 10^{-3}$ and $a = 2.978\mathring{A}$ (see Section 3.6.1). The elastic constants and solid bulk modulus calculated from MD simulations and the solid bulk modulus from Jaatinen et al. [54] are also listed for comparison. The negative sign for P^c in table 5.1 suggests that the $\xi = 0$ state experiences a tensile load, which is illustrated in Fig 5.3, where the point corresponding to $\xi = 0$ (green square) is to the right of the minimum where $P^c = 0$ (when $P^0 = 0$).

	EOF-PFC	Jaatinen et al. [54]	MD [62]
$\mathcal{H}_{\text{iso}}$	721.7	-	-
$\mathcal{H}_{\text{bi}}$	45.92	-	-
$\mathcal{H}_{\text{sh}}$	25.61	-	-
P^c (GPa)	-2.27	-	0.00
C_{11} (GPa)	280.7	-	128.0
C_{12} (GPa)	240.1	-	103.4
C_{44} (GPa)	45.7	-	63.9
$\mathcal{K}^c$ (GPa)	252.9	94.5	111.6

Table 5.1: Elastic constants and solid bulk modulus of EOF-PFC model determined from relationships developed in Chapter IV (second column) and solid bulk modulus from Ref. [54] (third column) are listed. The elastic constants and solid bulk modulus from MD simulations [62] using the EAM-MD potential of Ref. [20] (fourth column) are also listed. The elastic constants from the EOF-PFC model are calculated for $\bar{n} = \bar{n}_s = 9.17 \times 10^{-3}$ (see Section 3.6.1).

The values of C_{11} and C_{12} calculated from the EOF-PFC model are more than twice the values from MD simulations, while C_{44} from the EOF-PFC model is approximately 30% less than that of MD simulations. Whether these discrepancies arise from the difference in pressure state between the values from EOF-PFC and MD simulations will be examined in the next section when we consider the elastic constants from the EOF-PFC model at a zero-pressure state.

It is also important to note that the value of $\mathcal{K}^c$ presented in Jaatinen et al. [54], which we denote as $\mathcal{K}'^c$, although closer to the value from MD simulations, is inconsistent with the definition of $(C_{11} + 2C_{12} + P^c)/3$ and is less than half the value that we calculate for the EOF-PFC model. This discrepancy is due to a difference in the procedure for calculating $\mathcal{K}^c$ and $\mathcal{K}'^c$. The relationships for determining $\mathcal{K}^c$ is based on thermoelasticity theory (see Chapter IV), while the relationship for determining $\mathcal{K}'^c$ is [54]

$$\begin{aligned} \mathcal{K}'^c &\equiv (\rho_A^c)^2 \left(\frac{\partial^2 (\Delta \mathcal{F}^{\text{bulk},c}_{\text{PFC,iso}} / \mathcal{V}_C^c)}{\partial (\rho_A^c)^2} \right) \Bigg|_{\theta^c} \\ &= (1+\bar{n})^2 \left(\frac{\partial^2 \Delta f^{\text{bulk},c}_{\text{PFC,iso}}}{\partial \bar{n}^2} \right) \Bigg|_{\theta^c}, \end{aligned} \tag{5.39}$$

where $\rho_A^c = \rho_0(1+\bar{n})$ (see Eq. (3.41)). As seen in Section 3.6.1, Eq. (5.39) is related to the curvature of the EOF-PFC FED curve vs. $\bar{n}$ in Fig. 3.2 (or slope of Fig. (3.3)), which is a measure of how the diffusion potential changes with $\bar{n}$.

5.6.2 Elastic Constants and Solid Bulk Modulus of *bcc* Structure at Zero-Pressure State

In this section, we examine whether matching the pressure state of the EOF-PFC model to MD simulations will improve the match between their values of elastic constants and solid bulk modulus. The elastic constants and solid bulk modulus values of the EOF-PFC model at the zero-pressure state are determined by evaluating $\mathcal{H}_{\text{iso}}$, $\mathcal{H}_{\text{bi}}$, and $\mathcal{H}_{\text{sh}}$ at $\xi = -0.00474$, which corresponds to the minimum of the FED vs. ξ curve in Fig. 5.3 where $P^c = 0$. The EOF-PFC FED as a function of $\bar{n}$ for isotropic deformation is replotted in Fig. 5.6 to illustrate the points corresponding to $\xi = -0.00474$ (black vertical dashed line) and $\xi = 0$ (green square). The value of $\bar{n}$ at $\xi = -0.00474$ is 9.30×10^{-3}, which is an increase from $\bar{n}_s$.

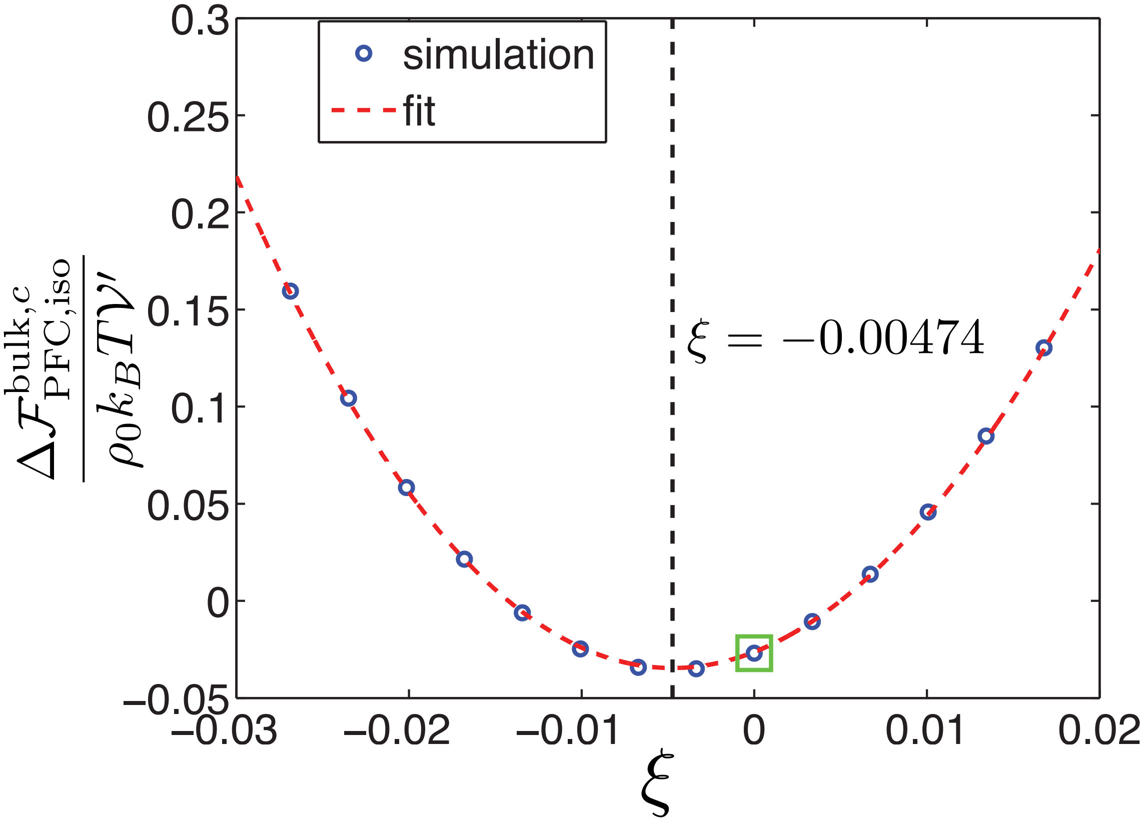

Figure 5.6: Plot of non-dimensionalized EOF-PFC FED as a function of ξ for isotropic deformation. All points have the same value of $\bar{n}'$ (N_A^c held constant), while $\bar{n}$ varies. The values calculated using FM (blue dots) are fitted with a third-order polynomial function (red dashed curve): $-910.6\xi^3 + 360.8\xi^2 + 3.480\xi - 0.0263$. The value of ξ corresponding to the zero-pressure state is denoted by the dashed vertical black line ($\xi = -0.00474$), where $\bar{n} = 9.30 \times 10^{-3}$. The green square marks the state with $\xi = 0$, where $\bar{n} = \bar{n}_s = 9.17 \times 10^{-3}$.

The values of C_{11}, C_{12}, C_{44}, and $\mathcal{K}^c$ at $\xi = -0.00474$ (zero-pressure state) are listed in Table 5.2. These values correspond to $\bar{n} = 9.30 \times 10^{-3}$ and $a = 2.978\mathring{A}$. The elastic constants and solid bulk modulus for $\xi = 0$ and those calculated from MD simulations are also listed for comparison. As seen in table 5.2, C_{11}, C_{12}, and $\mathcal{K}^c$ increase by less than 3%, while C_{44} decreases by more than 45% when P^c changes from -2.27 to 0 GPa. Surprisingly, matching the pressure state of the EOF-PFC model and that of the MD calculations widens the discrepancy between their results. This result suggests that an alternative parameterization is necessary to match the elastic constant values of the PFC model to those of MD simulations.

	EOF ($\xi = -0.00474$)	EOF ($\xi = 0$)	MD [62]
$\mathcal{H}_{\text{iso}}$	747.5	721.7	-
$\mathcal{H}_{\text{bi}}$	45.90	45.92	-
$\mathcal{H}_{\text{sh}}$	12.76	25.61	-
P^c (GPa)	0.00	-2.27	0.00
C_{11} (GPa)	290.7	282.8	128.0
C_{12} (GPa)	245.7	240.1	103.4
C_{44} (GPa)	25.0	45.7	63.9
$\mathcal{K}^c$ (GPa)	260.7	253.6	111.6

Table 5.2: Elastic constants and solid bulk modulus calculated from EOF-PFC model for parameters listed in table 2.1 (second and third column) and MD simulations [62] for EAM-MD potential of Ref. [20] (fourth column) are listed. The elastic constants and solid bulk modulus, $\mathcal{K}^c$ from the EOF-PFC model are calculated for $\bar{n} = 9.30 \times 10^{-3}$ ($P^c = 0$) and $\bar{n} = \bar{n}_s = 9.17 \times 10^{-3}$ ($P^c = -2.27$ GPa).

5.7 Chapter Summary

We have presented three numerical methods for implementing deformation in the PFC model, which differ in how the FED of the deformed system is evaluated. We illustrated the requirement of an interpolation step when applying shear-type deformations with the conventional method, CM, used in the PFC model. An alternative method, LM, that eliminates the requirement of interpolation when applying shear-type deformation is derived by transforming the Laplacian operator of the PFC free energy. Additionally, a third method, FM, is formulated in Fourier space, where deformation is applied via a scaling of the wave vectors.

The accuracy and efficiency of all three methods were compared for isotropic, biaxial, and simple-shear deformations for an order parameter based on a one-mode approximation. FM was found to be more accurate and efficient than either CM or LM when the PFC free energy is expressed in Fourier space. In the case where a real space method is necessary, LM is more accurate and efficient than CM.

FM was employed to implement the relationships developed in Chapter IV to calculate the elastic constants and solid bulk modulus of *bcc* structures stabilized by the EOF-PFC model at two pressure states. In both cases, the values of C_{11}, C_{12}, C_{44}, and solid bulk modulus, $\mathcal{K}^c$, did not match well with those calculated from MD calculations at zero pressure. The values of C_{11}, C_{12}, and $\mathcal{K}^c$ from the EOF-PFC model were higher than those of MD simulations, while C_{44} from the EOF-PFC model was lower than that of MD simulations.

CHAPTER VI

Phase-Field Crystal Model for a Diamond-Cubic Structure

In this chapter, we investigate a diamond-cubic (*dc*) structure based on the structural PFC (XPFC) model. We demonstrate that the XPFC model yields a stable *dc* structure when the two-peak direct correlation function (DCF) is approximated with a combination of two Gaussian functions in Fourier space, with the first and second peak positions centered at $k_1 = 2\pi\sqrt{3}/a$ and $k_2 = 2\pi\sqrt{8}/a$, respectively, where a is the lattice constant of a cubic structure, and k_1 and k_2 are magnitudes of wave vectors. A temperature-density phase diagram that contains a *dc* solid-liquid coexistence region is then calculated for this model. We then focus on the interfacial energies, including the interfacial anisotropy that arises naturally in the PFC model. We examine how the solid-liquid interfacial energy of the *dc* structure depends on the shape of the DCF within the *dc*-PFC model. A relationship for solid-liquid interfacial energy as a function of temperature is developed for the *dc* structure by taking the peak heights of the Gaussian functions in the two-body DCF to change with a temperature parameter according to the functional form of the Debye-Waller Factor [55]. Additionally, since the energy change due to interfaces, defects, and strain is controlled by the peak width of the Gaussian functions [55], relationships for the dependence of interfacial energies on peak widths are also determined. These relationships can be used to parameterize the *dc*-PFC model to match interfacial energies to those measured experimentally or calculated from atomistic simulations.

This chapter is outlined as follows. We first present a procedure based on Chapter III for constructing phase diagrams in the PFC model in Section 6.1, and use it to calculate a phase diagram for the *dc* structure. The phase diagram contains a *dc*-liquid coexistence region, enabling us to numerically examine the solid-liquid interfacial properties of the *dc* structure in Section 6.2. Relationships between the interfacial energy and the peak widths and heights of the Gaussian functions in the DCF are also developed in Section 6.2.

6.1 Phase Stability of a Diamond-Cubic Structure

In this section, we demonstrate that the XPFC model can be used to stabilize the *dc* crystal structure. We also examine the phase stability between *dc* and other phases to construct a temperature-density phase diagram. First, we describe the procedure for constructing a phase diagram with the PFC model [55, 58, 66], which is used in this work. We then introduce a two-body DCF that stabilizes a *dc* structure and construct a temperature-density phase diagram that consists of the *bcc*, *dc*, and liquid phases based on the model.

6.1.1 Procedure for Constructing a Phase Diagram

A phase diagram for the PFC model is constructed by finding the average of the scaled dimensionless number density, $\bar{n}$, that corresponds to the phase boundaries as a function of σ [55, 58, 66]. The procedure for identifying the phase boundaries for each value of σ is divided into two steps. First, free-energy densities as a function of $\bar{n}$ are calculated for each phase by minimizing the free-energy density, $\Delta f^{\alpha}(\bar{n}, a)$, with respect to a, where the superscript α denotes the phase (e.g., $\alpha =$ *bcc*, fcc, *dc*).

The quantity $\Delta f^{\alpha}(\bar{n}, a)$ is calculated via,

$$\Delta f^{\alpha}(\bar{n}, a) \equiv \frac{\Delta \mathcal{F}^{\alpha}[n_a(\mathbf{r})]}{V_a}, \tag{6.1}$$

where $V_a \equiv a^3$ is the unit-cell volume, a is the lattice parameter of a cubic unit cell, and $n_a(\mathbf{r})$ is the relaxed density profile. The relaxed density profile is obtained by evolving a (non-relaxed) density profile that is approximated with the one-mode approximation with an average of $\bar{n}$ using conserved dissipative dynamics [23, 24, 45],

$$\frac{\partial n(\mathbf{r})}{\partial t} = \nabla^2 \frac{\delta \Delta \mathcal{F}^{\alpha}[n(\mathbf{r})]}{\delta n(\mathbf{r})}, \tag{6.2}$$

until a steady state is reached. The quantity $\Delta f^{\alpha}(\bar{n}, a)$ is a function of only $\bar{n}$ and a because $\Delta f^{\alpha}(\bar{n}, a)$ is the free-energy density of a system with $n_a(\mathbf{r})$, which is periodic with a uniform amplitude. For convenience, we denote the value of $\Delta f^{\alpha}(\bar{n}, a)$ that is minimized with respect to a as $\Delta f^{\alpha}_{a^*}(\bar{n})$ and the corresponding lattice spacing as a^*. This process is schematically illustrated in Fig. 6.1(a) where the point $(a^*, \Delta f^{\alpha}_{a^*}(\bar{n}))$ is marked with “×”.

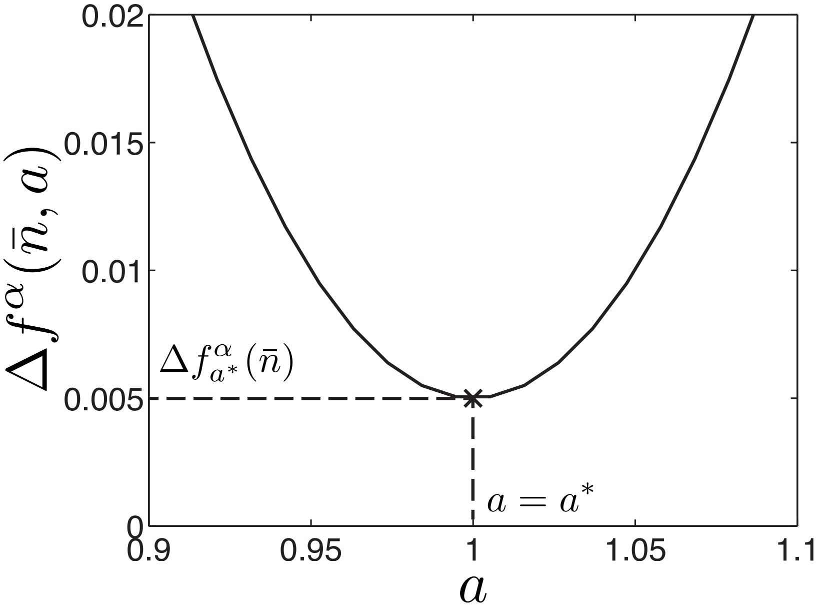

(a)

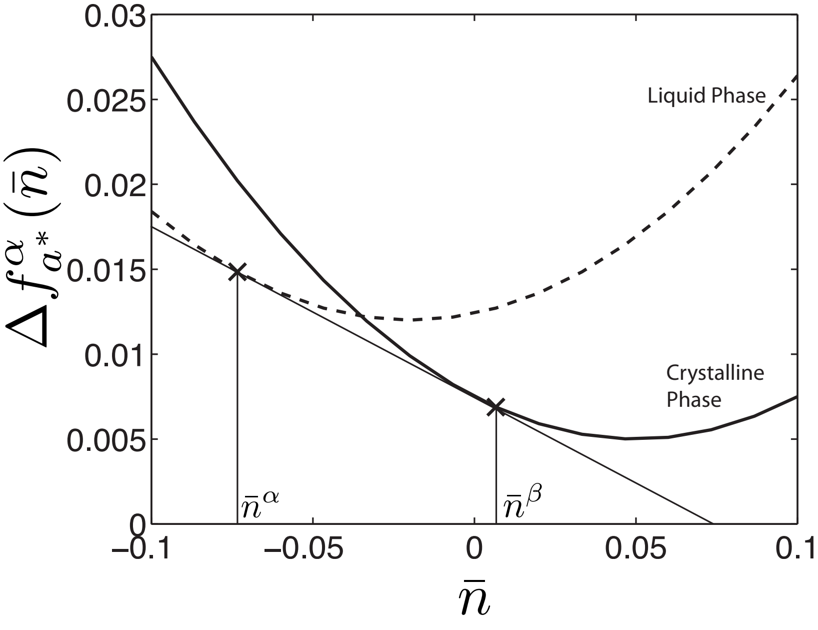

(b)

Figure 6.1: (a) Schematic plot of free-energy density of a relaxed system as a function of the lattice spacing for a given $\bar{n}$. The point at which $\Delta f^{\alpha}(\bar{n}, a)$ is minimized with respect to a is marked with "×". (b) Schematic of the free-energy densities that satisfy $\partial \Delta f^{\alpha}(\bar{n}, a)/\partial a = 0$ at each $\bar{n}$ (as illustrated in (a)). The solid curve shows the free-energy density for the crystalline phase, and the dashed curve shows the corresponding values for the liquid phase. The "×" denotes the comment-tangent points of the free-energy density curves, which satisfy Eqs. (6.3) and (6.4).

Second, phase boundaries are determined with a common-tangent construction on the convex hull [90] of $\Delta f^{\alpha}_{a^*}(\bar{n})$ for all phases. The common-tangent construction is mathematically stated as a set of conditions:

$$\left.\frac{\partial \Delta f^{\alpha}_{a^*}(\bar{n})}{\partial \bar{n}}\right|_{\bar{n}=\bar{n}^{\alpha}} = \left.\frac{\partial \Delta f^{\beta}_{a^*}(\bar{n})}{\partial \bar{n}}\right|_{\bar{n}=\bar{n}^{\beta}} \tag{6.3}$$

and

$$\Delta f^{\beta}_{a^*}(\bar{n}) - \Delta f^{\alpha}_{a^*}(\bar{n}) = \left.\frac{\partial \Delta f^{\alpha}_{a^*}(\bar{n})}{\partial \bar{n}}\right|_{\bar{n}=\bar{n}^{\alpha}} (\bar{n}^{\beta} - \bar{n}^{\alpha}). \tag{6.4}$$

The additional superscript, β, denotes a phase different from that indicated by α (e.g., $\alpha = bcc$ and $\beta = fcc$) and the partial derivatives are evaluated at the specified value of $\bar{n}$, as indicated by the subscripts on the vertical line. Equations (6.3) and (6.4) ensure that the chemical potentials and pressures of the coexisting phases, respectively, are equal [66]. The conditions of Eqs. (6.3) and (6.4) are illustrated in Fig. 6.1(b), where "×" marks the common-tangent points. The procedure described above is repeated for different values of σ to construct a phase diagram.

6.1.2 A Diamond-Cubic Structure

A *dc* structure is an *fcc* derivative structure that consists of the lattice-sites of two *fcc* structures that are shifted from one another by $a_{fcc}/4$ in each direction [91]. The lattice-site positions of the two *fcc* structures are specified by two basis vectors. The two *fcc* structures within a single *dc* unit cell are illustrated in Fig. 6.2(a).

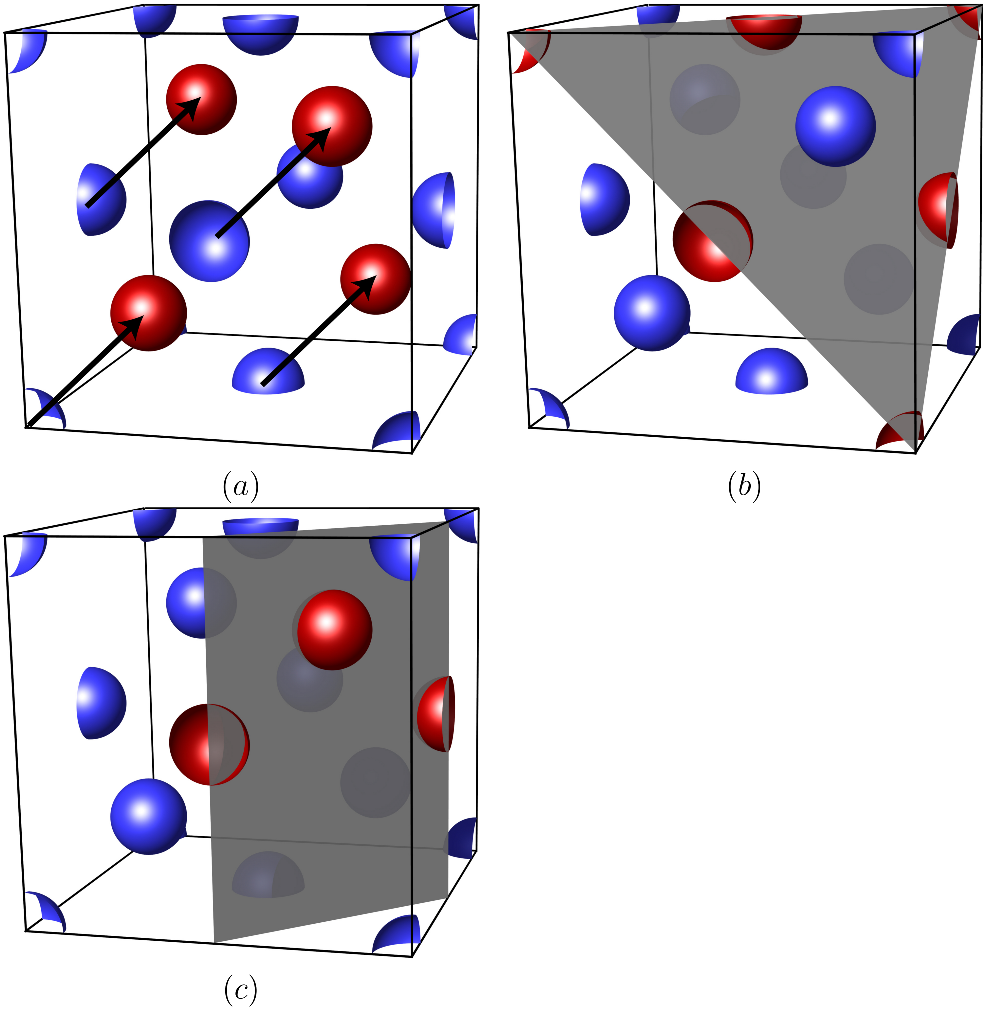

(a)

(b)

(c)

Figure 6.2: (a) Schematic of a unit cell of the dc structure where the shift of $a_{fcc}/4$ in each direction between the lattice-site positions of two fcc structures (one represented by blue and the other by red) is denoted by arrows. Schematics of the (b) (111) and (c) (220) crystallographic planes, where the lattice points that are intersected by the atomic planes are highlighted in red. Each plane of the {111} and {220} families of planes intersect 2 atoms for the dc structure.

We find that a two-body DCF approximated with the combination of two Gaussian functions centered at $k_1 = 2\pi\sqrt{3}/a_{dc}$ and $k_2 = 2\pi\sqrt{8}/a_{dc}$ will stabilize a *dc* structure. The values of $k_1 = 2\pi\sqrt{3}/a_{dc}$ and $k_2 = 2\pi\sqrt{8}/a_{dc}$ correspond to the $\{111\}$ and $\{220\}$ families of crystallographic planes, which are associated with the first two peaks of the *dc* structure factor [91]. As in the fcc structure, the ratio of peak positions of the *dc* structure, $k_2/k_1 = \sqrt{8/3}$, is independent of a_{dc}. An fcc structure is not stable for this DCF because it does not contain a peak corresponding to the $\{200\}$ family of crystallographic planes, which is required for the stabilization of an fcc structure [58].

To construct a phase diagram for the *dc* structure, we choose $a_{dc} = 1\mathring{A}$ and $\alpha_1 = \alpha_2 = 1.0$. The $\{111\}$ and $\{220\}$ families of crystallographic planes of the *dc* structure contain 8 and 12 equivalent planes, respectively. Therefore, the parameters β_1 and β_2, which are the number of planar symmetries of the $\{111\}$ and $\{220\}$ families of crystallographic planes, are 8 and 12, respectively. Each plane of the $\{111\}$ and $\{220\}$ families of planes have an area of $\sqrt{3}/2 \times a_{dc}^2$ and $\sqrt{2}/2 \times a_{dc}^2$, respectively, and intersects 2 atoms in the *dc* structure, as shown in Figs. 6.2(b) and (c). Therefore, the parameters λ_1 and λ_2 are $2/(\sqrt{3}/2) = 4/\sqrt{3}\mathring{A}^{-2}$ and $2/(\sqrt{2}/2) = 2\sqrt{2}\mathring{A}^{-2}$, respectively.

The *dc* DCF in Fourier space is plotted for $\sigma = 0.0$, 0.2, and 0.4 in Fig. 6.3(a) for the values of k_i, λ_i, β_i, and α_i mentioned above. The stability of the *dc* structure was verified by comparing the unit-cell free-energy density of the *dc* structure to those of the *bcc*, fcc, *sc*, *hcp*, rod, and stripe phases [66]. Additionally, the stability of the *dc* structure for calculations beyond a unit cell was demonstrated by the growth of an 18 ($2 \times 3 \times 3$) unit-cell *dc* seed into a 64 unit-cell system for $\sigma = 0.01$ and $\bar{n} = 0.02$ via Eq. (6.2); the initial seed was generated by appending relaxed unit cells of the *dc* structure. The isosurface of the relaxed 64 unit cell system is shown in Fig. 6.3(b) and a small portion of the system is extracted in Fig. 6.3(c) to illustrate two overlapping fcc lattices in the *dc* structure. It is important to note that a metastable *bcc* structure forms when the initial seed size is smaller than 18 unit cells for the 64 unit-cell system considered in Fig. 6.3(b). This suggests that the density profile can converge to a metastable structure (*bcc*) instead of the stable structure (*dc*) when the dynamics described by Eq. (6.2) is used to evolve the density field. The formation of a metastable *bcc* phase prior to forming a stable *dc* phase was also observed in a recently proposed self-assembly model [92]. An investigation of different dynamics for the PFC model is outside the scope of this chapter. We refer the readers to Ref. [68] for an overview of various PFC dynamics.

A density-temperature phase diagram, shown in Fig. 6.3(d), is constructed according to the procedure presented in Section 6.1.1. The phase diagram shows a stable liquid phase at low densities and solid phases at higher densities. The coexistence between liquid and *dc*, liquid and *bcc*, and *bcc* and *dc* phases are also shown in Fig. 6.3(d). Since k_1 corresponds to the $\{111\}$ family of planes in the *dc* structure and the $\{110\}$ family of planes in the *bcc* structure, the lattice constant of the *dc* and *bcc* structures are different and related to one another by $a_{bcc}/a_{dc} = \sqrt{2/3}$.

The small gap between the *bcc* and *dc* coexisting densities is due to the similarity between the free-energy densities of the two solid phases. The similarity in the coexisting densities is undesirable, for example, when studying solid defects in a two-phase system. To alter the energy of each phase and thus potentially increase the gap of the solid-coexistence densities, one can modify, in addition to the two-body DCF, the values of a_t and b_t ideal-gas contribution of the PFC free energy, Eq. (2.13) [54]. This will be investigated in the future.

An important feature of the phase diagram in Fig. 6.3(d) is the *dc*-liquid coexistence at lower temperatures and the *bcc*-liquid coexistence at higher temperatures. A *bcc* phase becomes stable for a two-peak DCF when the the first peak is significantly taller than the second peak, as described in Ref. [58]. When the parameters in Eq.

(2.27) are chosen to be

$$\frac{\lambda_1\beta_1}{\lambda_2\beta_2} > \left(\frac{k_1}{k_2}\right)^2, \tag{6.5}$$

the first peak of the DCF becomes taller than the second peak as σ increases (e.g., see Fig. 6.3(a)). The parameters used to construct the phase diagram of Fig. 6.3(d) has $(\lambda_1\beta_1)/(\lambda_2\beta_2) = 1.45(k_1/k_2)^2$, and thus a transition from the *dc* phase at lower temperatures to the *bcc* phase at higher temperatures is observed.

On the other hand, the *bcc* phase can be suppressed at all temperatures if the height of the first and second peaks of a two-peak DCF are constrained to be equal for all values of σ. This occurs when

$$\frac{\lambda_1\beta_1}{\lambda_2\beta_2} = \left(\frac{k_1}{k_2}\right)^2. \tag{6.6}$$

A phase diagram where Eq. (6.6) is satisfied is plotted in Fig. 6.4; as expected, the *bcc* phase has been suppressed.

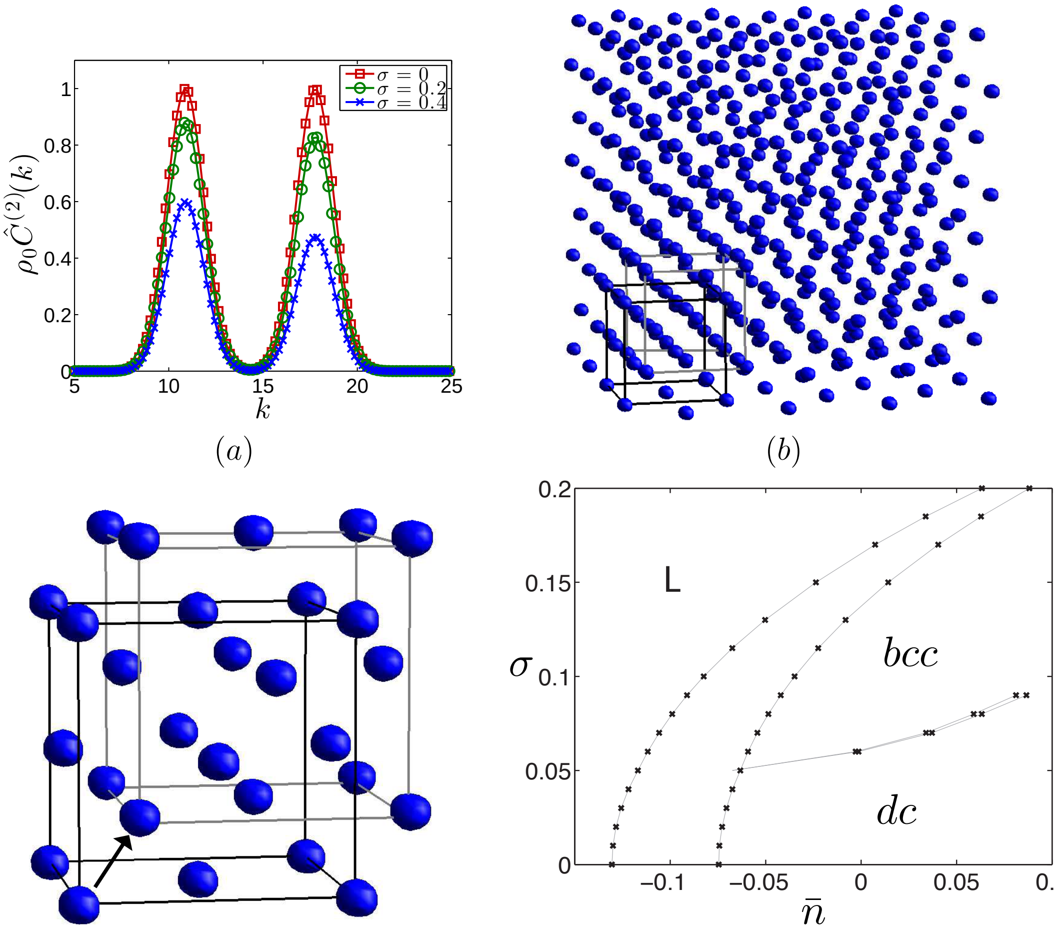

(a) (b) (c) (d)

Figure 6.3: (a) The two-body DCF for a *dc* structure for $\sigma = 0.0$, 0.2, and 0.4. The parameters used are $\alpha_1 = \alpha_2 = 1.0$, $\lambda_1 = 4/\sqrt{3}\mathring{A}^{-2}$, $\lambda_2 = 4/\sqrt{2}\mathring{A}^{-2}$, $\beta_1 = 8$, $\beta_2 = 12$, $k_1 = 2\pi\sqrt{3}\mathring{A}^{-1}$, and $k_2 = 2\pi\sqrt{8}\mathring{A}^{-1}$. (b) The isosurface of a 64 unit-cell *dc* structure calculated for $\bar{n} = 0.02$ and $\sigma = 0.01$. (c) Small portion of Fig. (b) showing two overlapping fcc lattices in a *dc* structure. The black arrow denotes the shift of a lattice site from one fcc lattice to the other. (d) Phase diagram containing body-centered-cubic (*bcc*), diamond-cubic (*dc*), and liquid (L) phases.

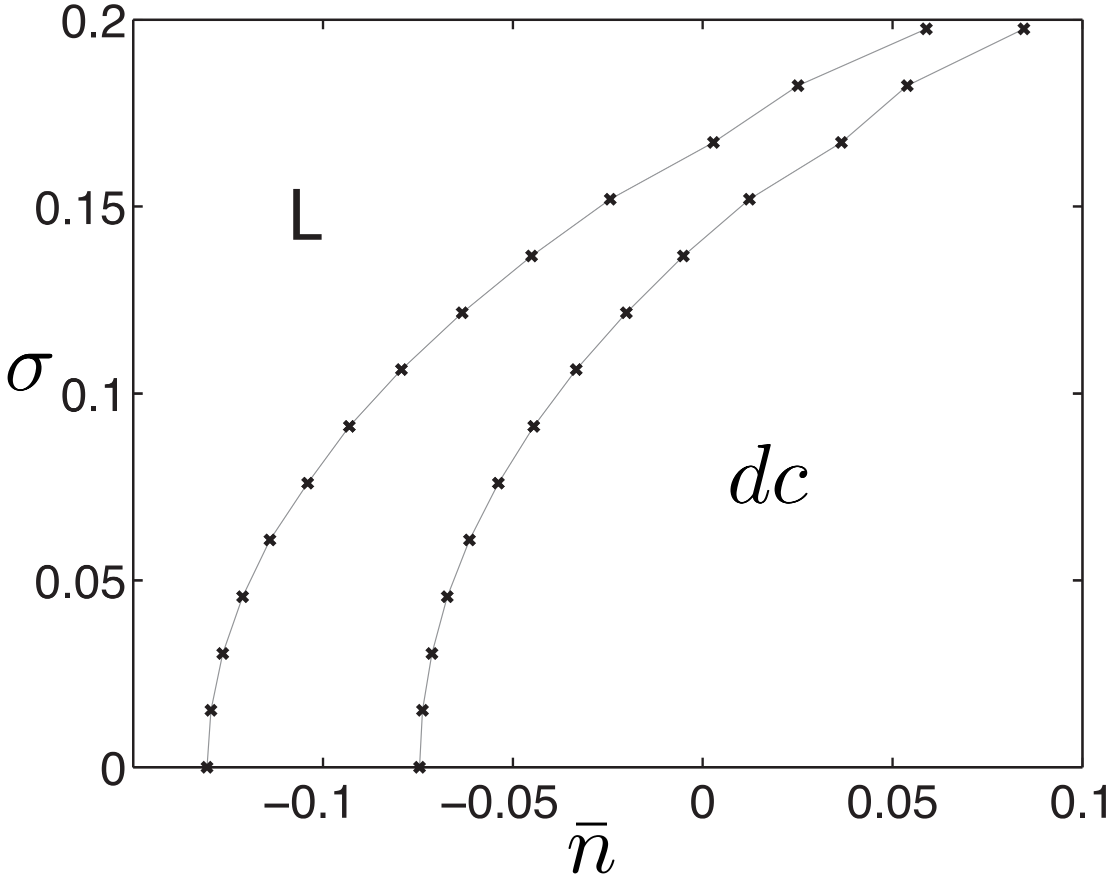

Figure 6.4: Phase diagram containing diamond-cubic (dc) and liquid (L) phases. The parameters of the two-body DCF used to construct this phase diagram are $\alpha_1 = \alpha_2 = 1.0$, $\lambda_1 = 4/\sqrt{3}\mathring{A}^{-2}$, $\beta_1 = 8$, $k_1 = 2\pi\sqrt{3}\mathring{A}^{-1}$, $k_2 = 2\pi\sqrt{8}\mathring{A}^{-1}$, and $\lambda_2\beta_2 = 8/3\lambda_1\beta_1$.

6.2 Solid-Liquid Interfacial Energy

We examine the solid-liquid interfacial energies of the *dc* structure described in the previous section. First, we describe a numerical procedure for calculating interfacial energy between two phases. Second, we determine a relationship for interfacial energy as a function of Gaussian peak width because the peak widths of the Gaussian functions in the DCF were shown to account for excess energy associated with interfaces [55]. Third, we develop a relationship for interfacial energy as a function of temperature by adjusting peak heights. Finally, we consider a more general case of two-body DCFs where the first and second peaks of the Gaussian functions have different widths. This analysis provides an approximate relationship between interfacial energy and peak width of the Gaussian functions when the peak widths are not equal. For the analysis below, k_i, λ_i, and β_i are set to the values that were used to construct the phase diagram in Fig. 6.3(d).

6.2.1 Procedure for Numerical Calculation of Solid-Liquid Interfacial Energy

The interfacial energy of a system that is in solid-liquid coexistence can be calculated from the energy of the two-phase system minus the bulk energy of each phase [54]. In this section, the solid-liquid interfacial energy of an interface having a normal pointing in the direction p, γ_p, is evaluated by constructing a long slab of one unit-cell in the plane of the interface and 128 unit-cells in the direction of the interface normal. The slab is initialized with 64 unit cells of solid and 64 unit cells of liquid, with the interface at the midpoint of the computational domain. Periodic boundary conditions are applied to all boundaries, which places another interface at the ends of the length of the computational domain. The slab is then numerically relaxed via Eq. (6.2). The value of γ_p is determined from the numerically relaxed slab by subtracting the free energy of the bulk phases from the total free energy of the slab and dividing by the cross-sectional area of the solid-liquid interface.

The bulk free energy, $\Delta\mathcal{F}^{bulk}$, is calculated from the free energies of solid with the same volume as the computational domain, $\Delta\mathcal{F}_s$, and liquid with the same volume as the computational domain, $\Delta\mathcal{F}_l$. These free energies are weighted by the volume fraction before they are summed. Therefore, with the average of the scaled number densities of the solid and liquid at the coexistence density, $\bar{n}_s$ and $\bar{n}_l$, respectively, $\Delta\mathcal{F}^{bulk}$ is given by

$$\Delta\mathcal{F}^{bulk} = \frac{\Delta\mathcal{F}_s(\bar{n} - \bar{n}_l) + \Delta\mathcal{F}_l(\bar{n}_s - \bar{n})}{\bar{n}_s - \bar{n}_l}, \tag{6.7}$$

where the weighing of $\Delta\mathcal{F}_s$ and $\Delta\mathcal{F}_l$ is determined according to volume fractions of solid and liquid in the system in terms of the respective densities. The value of γ_p is then calculated by subtracting $\Delta\mathcal{F}^{bulk}$ from the total free energy of the slab containing the solid-liquid interfaces, $\Delta\mathcal{F}_p^{slab}$, and dividing by the cross-sectional area, A_p,

$$\gamma_p = \frac{1}{\rho_0 k_B T}\left(\frac{\Delta\mathcal{F}_p^{slab} - \Delta\mathcal{F}^{bulk}}{2A_p}\right), \tag{6.8}$$

where the factor, $1/(\rho_0 k_B T)$, nondimensionalizes the value of γ_p and the factor of 2 accounts for the additional interface at the edge of the computational domain due to the periodic boundary conditions. The length of the slab in the direction of the interface normal is chosen such that the two solid-liquid interfaces that form as a result of periodic boundary conditions do not interact. In this work, we examine the γ_p of interfaces with normals pointing in the [100], [110], and [111] directions, where $p = 100, 110$, and 111, respectively. This analysis is performed on an XSEDE computing cluster [93].

6.2.2 Peak-Width Dependence of Solid-Liquid Interfacial Energy

We use the procedure described in Section 6.2.1 to compare the solid-liquid interfacial energies, $\gamma_p(\sigma, \alpha_1, \alpha_2)$, for different peak widths, α_i, of the Gaussian functions in the two-body DCF. The calculations presented here are for the *dc* DCF used to construct Fig. 6.3(d) with $\sigma = 0$, which leads to both peak heights to be 1, and $\alpha_1 = \alpha_2 \equiv \alpha_0$, which sets the peak widths equal. The value of $\gamma_p(0, \alpha_0, \alpha_0)$ for the (100), (110), and (111) interfaces for values of α_0 ranging from 0.25 to 1.0 are plotted in Fig. 6.5. These interfacial energies decrease with increasing values of α_0. For the range of α_0, the (111) interface has the lowest energy, while the (100) interface has the highest energy. This is in qualitative agreement with the solid-liquid interfacial energies calculated for *dc* Si using atomistic simulations [94].

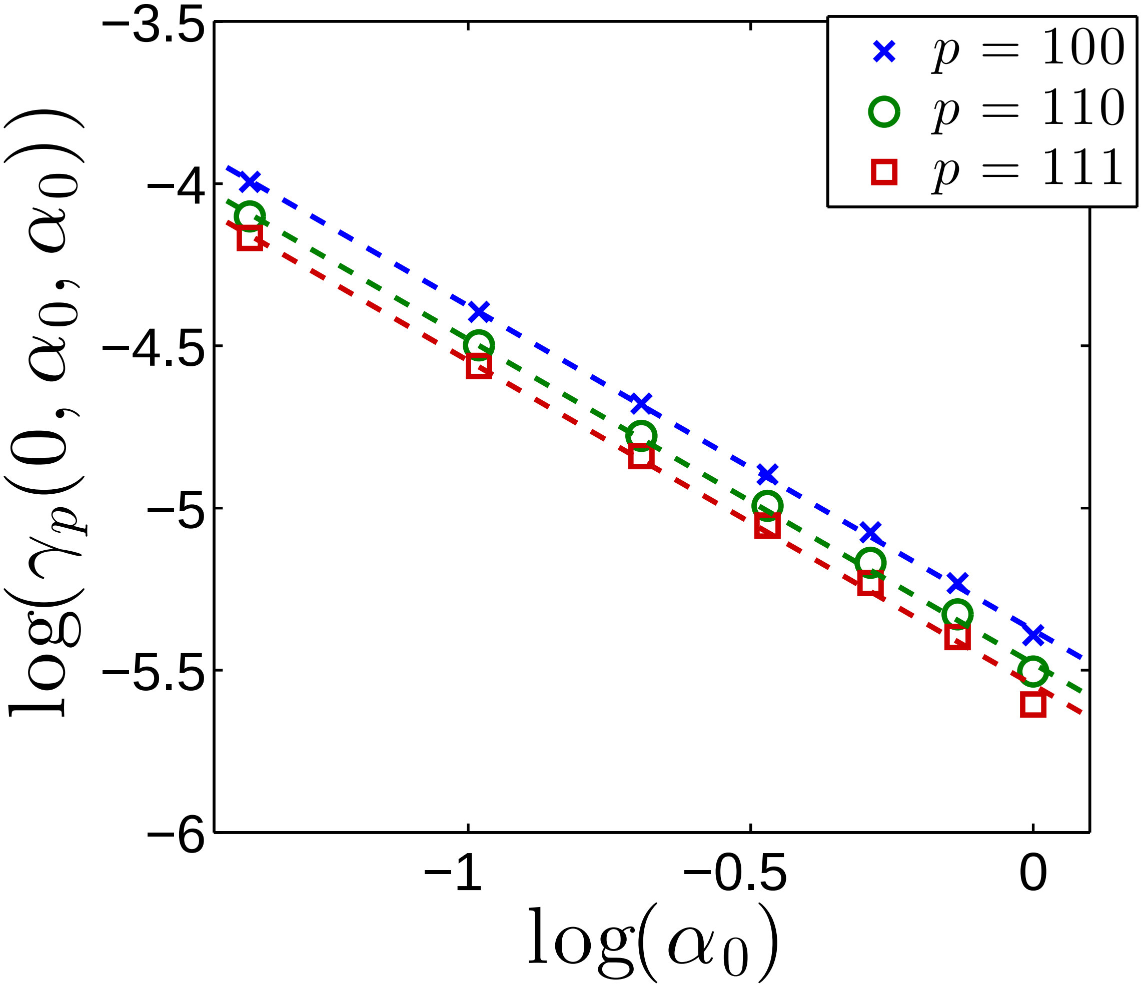

Figure 6.5: Plots of the logarithms of $\gamma_{100}(0, \alpha_0, \alpha_0)$ (blue "×"), $\gamma_{110}(0, \alpha_0, \alpha_0)$ (green circle), and $\gamma_{111}(0, \alpha_0, \alpha_0)$ (red square) for the *dc* free energy used to construct the phase diagram of Fig. 6.3(d) as a function of the logarithm of α_0. Here, $\alpha_1 = \alpha_2 = \alpha_0$ and $\sigma = 0$. The dashed lines are the best fits to the data in the form of Eq. (6.9).

The dashed lines in Fig. 6.5 are plots of an inverse power law given by

$$\gamma_p(0, \alpha_0, \alpha_0) = \frac{D_p}{\alpha_0}, \tag{6.9}$$

where $D_{100} = 4.62 \times 10^{-2}$, $D_{110} = 4.17 \times 10^{-2}$, and $D_{111} = 3.90 \times 10^{-2}$. Figure 6.5 demonstrates that the simulation results fit well to Eq. (6.9) with R^2 values of 1.00, 0.999, and 0.999 for D_{100}, D_{110}, and D_{111}, respectively.

6.2.3 Temperature Parameter Dependence of Solid-Liquid Interfacial Energy

In this section, we investigate the dependence of $\gamma_p(\sigma, \alpha_0, \alpha_0)$ on the peak height of the Gaussian functions in the two-body DCF by adjusting σ. Again, we consider the (100), (110), and (111) interfaces. First, we examine the effect of changing σ, while keeping α_0 fixed to 1. The results for these simulations are plotted in Fig. 6.6. The results show that $\gamma_p(\sigma, 1.0, 1.0)$, decreases with increasing σ.

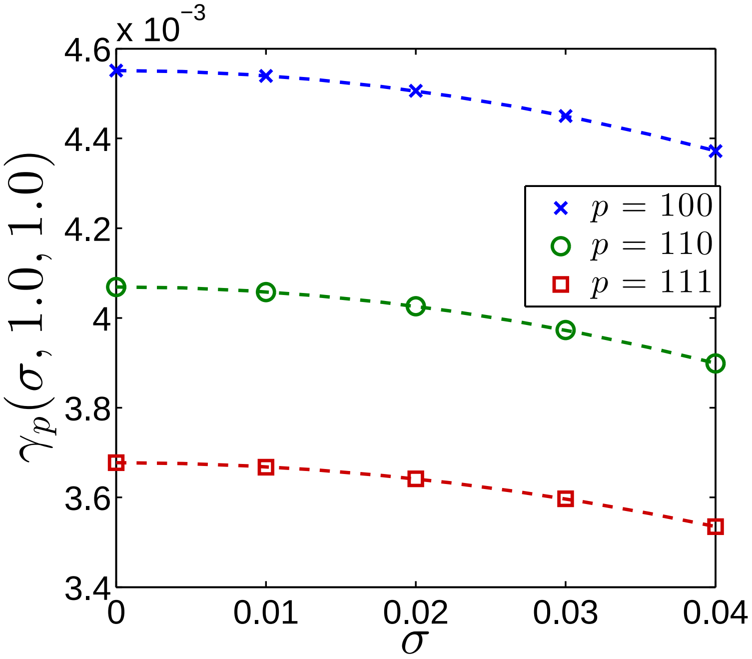

(a)

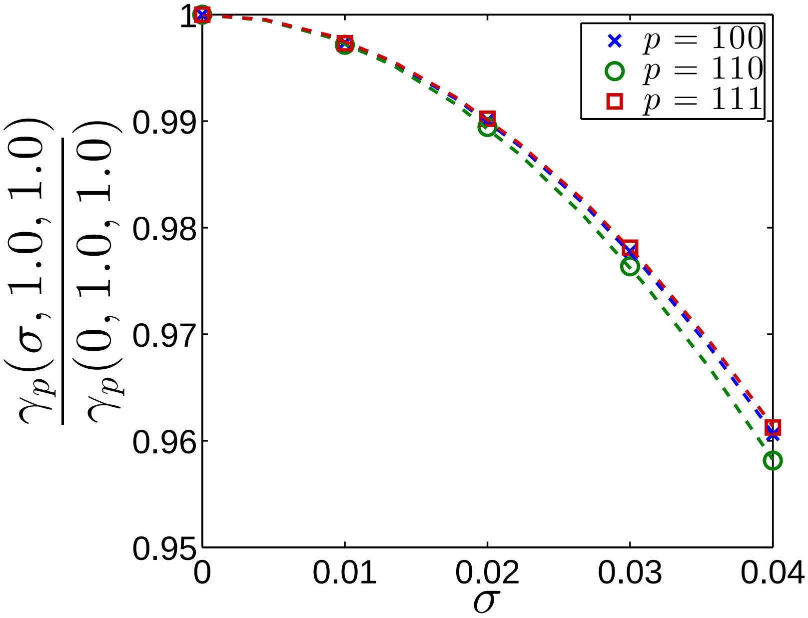

(b)

Figure 6.6: (a) $\gamma_p(\sigma, 1.0, 1.0)$ and (b) $\gamma_p(\sigma, 1.0, 1.0)/\gamma_p(0, 1.0, 1.0)$ as a function of σ for the (100) (blue "×"), (110) (green circle), and (111) (red square) interfaces. The calculations are for $\alpha_0 = 1.0$ and dashed curves show best fits to the data in the form of Eq. (6.10).

The dashed curves in Fig. 6.6 are the best fit curves to the data with a Gaussian function given by

$$\gamma_p(\sigma, \alpha_0, \alpha_0) = \gamma_p(0, \alpha_0, \alpha_0) \exp\left(-b_p(\alpha_0)\sigma^2\right), \tag{6.10}$$

where $\gamma_p(0, \alpha_0, \alpha_0)$ can be determined from Eq. (6.9) and $b_p(\alpha_0)$ is a fitting parameter, which depends on the peak width of the Gaussian function, α_0. Note that since the magnitudes of the σ values considered in this analysis are small, a quadratic equation will provide an equally good fit to the data. The plot in Fig. 6.6(a) shows that the simulation results fit well to Eq. (6.10), where the fitting constants are determined to be $b_{100}(1.0) = 25.06$, $b_{110}(1.0) = 26.66$, and $b_{111}(1.0) = 24.62$ with R^2 values of 1.00. These values of $b_p(1.0)$ show that the dependence of $\gamma_p(\sigma, 1.0, 1.0)$ on σ is weakest for the (111) interface and strongest for the (110) interface.

In Fig. 6.6(b), we also plot the scaled values of the interfacial energy, $\gamma_p(\sigma, 1.0, 1.0)/\gamma_p(0, 1.0, 1.0)$, for the same set of data. When scaled in this manner, all interfacial energies have a similar dependence on σ, which is expected from the similar values of $b_p(1.0)$. While the decrease in $\gamma_p(\sigma, 1.0, 1.0)/\gamma_p(0, 1.0, 1.0)$ with respect to σ is greatest for the (110) interface and least for the (111) interface, the differences are very small. This demonstrates that the orientation of the interface normal alters primarily the magnitude of the interfacial energies, but not its dependence on σ.

Next, we examine the dependence of $\gamma_{100}(\sigma, \alpha_0, \alpha_0)$ on σ and α_0. The results for these simulations are plotted in Fig. 6.7(a). It is evident that the interfacial energies decrease with increasing α_0, which is consistent with our previous results in Section 6.2.2. The energies for the (100) interface for $\alpha_0 = 0.25, 0.5$, and 1.0 all decrease with increasing σ, although the changes with respect to σ over the range examined are much smaller than the change due to the different values of α_0.

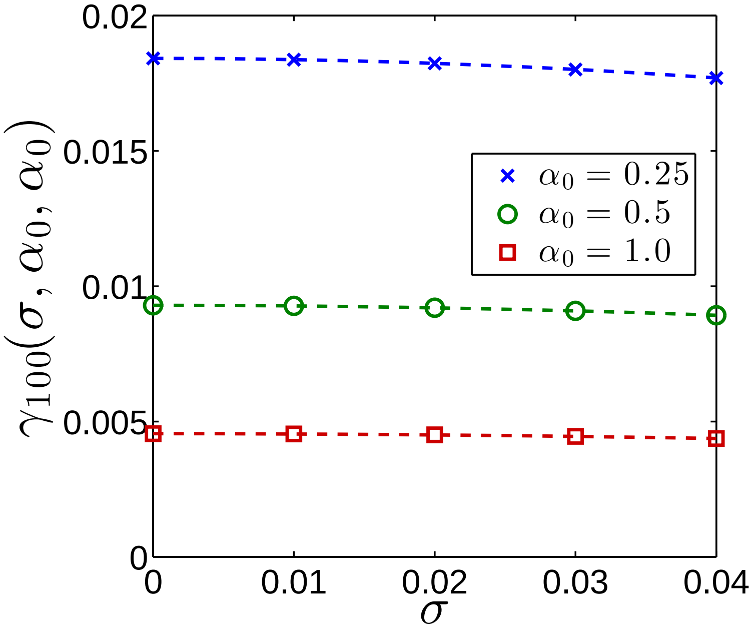

(a)

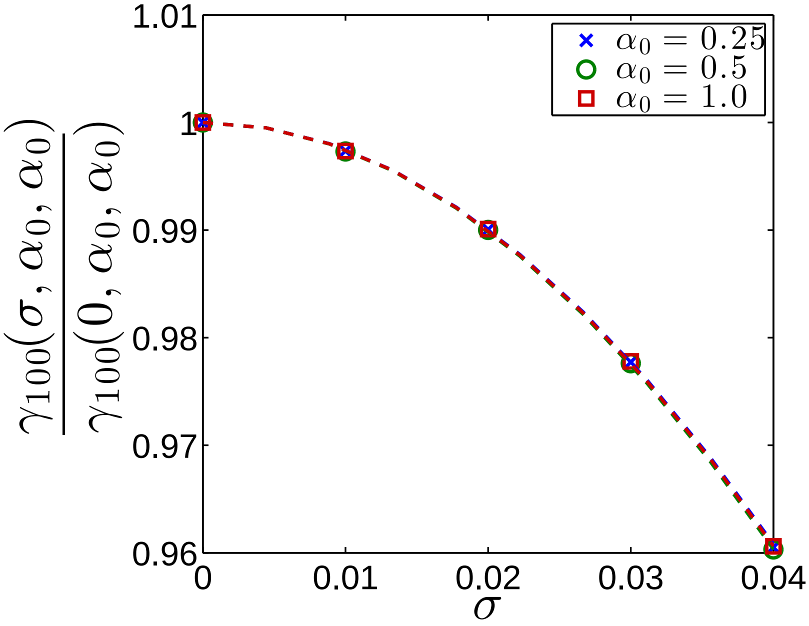

(b)

Figure 6.7: (a) $\gamma_{100}(\sigma, \alpha_0, \alpha_0)$ and (b) $\gamma_{100}(\sigma, \alpha_0, \alpha_0)/\gamma_{100}(0, \alpha_0, \alpha_0)$ as a function of σ for $\alpha_0 = 0.25$ (blue "×"), $\alpha_0 = 0.5$ (green circle), and $\alpha_0 = 1.0$ (red square). The dashed curves show best fits to the data in the form of Eq. (6.10).

The dashed curves in Fig. 6.7 are the best fits to the data with the Gaussian function, Eq. (6.10). As seen in Fig. 6.7(a), the simulation results fit well to Eq. (6.10), with $b_{100}(\alpha_0)$ being approximately 25.13 (specifically 25.13, 25.24, and 25.11 with R^2 values of 1.00 for $\alpha_0 = 0.25$, 0.5, and 1.0, respectively). The decrease in the values of $b_{100}(\alpha_0)$ with increasing α_0 indicates that the dependence of $\gamma_{100}(\sigma, \alpha_0, \alpha_0)$ on σ becomes weaker as α_0 increases.

In Fig. 6.7(b) we also plot the scaled values of the interfacial energy, $\gamma_{100}(\sigma, \alpha_0, \alpha_0)/\gamma_{100}(0, \alpha_0, \alpha_0)$, for the same set of data. As expected, the values of $\gamma_{100}(\sigma, \alpha_0, \alpha_0)/\gamma_{100}(0, \alpha_0, \alpha_0)$ are essentially identical for all values of α_0; the largest difference between the values of $b_{100}(\alpha_0)$ for $\alpha_0 = 0.25, 0.5$, and 1.0 is less than 1%. Although the analysis in Fig. 6.7 is for the (100) interface, the negligible dependence of $\gamma_{100}(\sigma, \alpha_0, \alpha_0)/\gamma_{100}(0, \alpha_0, \alpha_0)$ on α_0 is expected to hold for other interface orientations (other values of p) because $\gamma_p(0, \alpha_0, \alpha_0)$ depends on α_0 by the same relationship (Eq. (6.9)) for all orientations of the interface normal considered.

The negligible dependence of $\gamma_{100}(\sigma, \alpha_0, \alpha_0)/\gamma_{100}(0, \alpha_0, \alpha_0)$ on α_0 suggests that the expression in Eq. (6.10) can be simplified to

$$\gamma_p(\sigma, \alpha_0, \alpha_0) = \gamma_p(0, \alpha_0, \alpha_0) \exp\left(-\mathcal{R}_p \sigma^2\right), \tag{6.11}$$

where $\mathcal{R}_p$ is independent of α_0 for each value of p. For the *dc* DCF used in this analysis, $R_{100} = 25.06$, $R_{110} = 26.66$, and $R_{111} = 24.62$. Note that the heights of the Gaussian peaks in the two-body DCF also depend on σ by a Gaussian function, as seen in Eq. (2.27). The fact that the dependence of $\gamma_p(\sigma, \alpha_0, \alpha_0)$ on σ is also descibed by a Gaussian function suggests that the value of $\gamma_p(\sigma, \alpha_0, \alpha_0)$ is strongly influenced by the heights of the peaks in the two-body DCF.

In the analysis of Figs. 6.6 and 6.7, the values of $\gamma_p(\sigma, \alpha_0, \alpha_0)$ are calculated within the solid-liquid coexistence region, where $\bar{n}_s$ increases with σ, as seen in Fig. 6.3. An increase in $\bar{n}_s$ can only arise by adding atoms into the system (by filling vacant sites) because the position of the primary peak of the two-body DCF, k_1, is assumed to be constant, resulting in a fixed lattice spacing for all values of $\bar{n}$ and σ. As a result, $\gamma_p(\sigma, \alpha_0, \alpha_0)$ calculated for each value of σ in Figs. 6.6 and 6.7 is for a system containing a different number of atoms. Therefore, the dependence of $\gamma_p(\sigma, \alpha_0, \alpha_0)$ on σ obtained above can be interpreted as that of an open system. We believe the addition of atoms into the system as σ increases is the cause for a decreasing solid-liquid interfacial energy, which is in disagreement with the trend measured experimentally [95, 96] and calculated using atomistic simulations [97, 98, 99] for closed systems. Therefore, in order to directly compare the dependence of $\gamma_p(\sigma, \alpha_0, \alpha_0)$ on σ from the PFC model to the dependence of $\gamma_p(\sigma, \alpha_0, \alpha_0)$ on melting temperature from experiments and atomistic simulations, it is required to keep the number of particles constant as σ is varied, which is similar to what has been implemented for calculating elastic constants [53].

6.2.4 Solid-Liquid Interfacial Energy for Unequal Peak Widths

In this section, we investigate how the solid-liquid interfacial energy changes with respect to α_2, when $\alpha_1 \neq \alpha_2$. For our calculations, we set $\alpha_1 = 0.625$ and $\sigma = 0$, while adjusting the values of α_2. These results are plotted in Fig. 6.8, which shows that $\gamma_p(0, \alpha_1, \alpha_2)$ decreases as the ratio of α_2/α_1 increases for all directions.

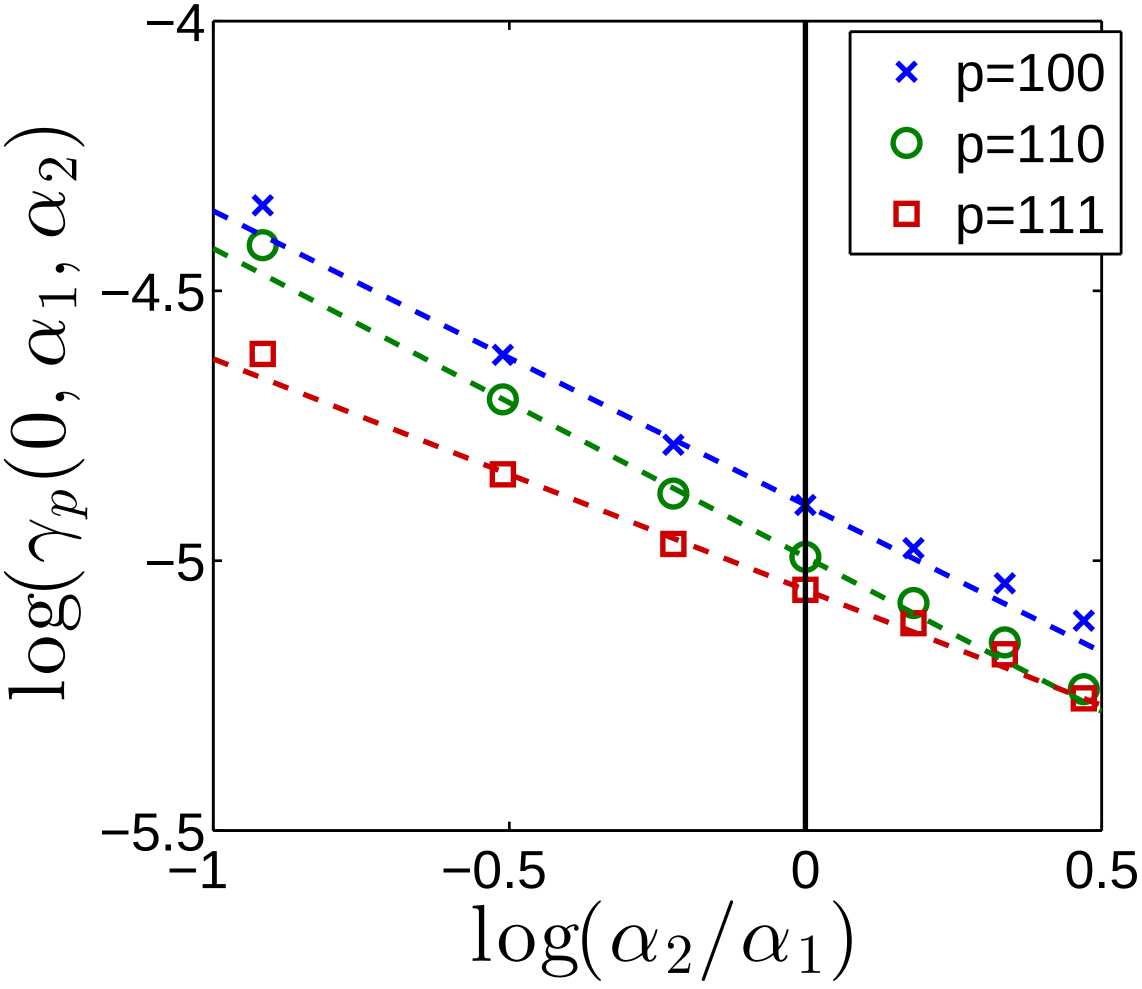

Figure 6.8: The logarithms of $\gamma_{100}(0,\alpha_1,\alpha_2)$ (blue "×"), $\gamma_{110}(0,\alpha_1,\alpha_2)$ (green circle), and $\gamma_{111}(0,\alpha_1,\alpha_2)$ (red square) plotted as a function of the logarithms of the ratio α_2/α_1. In these calculations $\alpha_1 = 0.625$ and $\sigma = 0$. The dashed lines show fits to Eq. (6.12) and the solid vertical line marks the position where $\alpha_2/\alpha_1 = 1$.

The dashed lines in Fig. 6.8 are the best fits for the interfacial energies in the form of an inverse power law given by

$$\gamma_p(0, \alpha_1, \alpha_2) = \gamma_p(0, \alpha_0, \alpha_0) \left(\frac{\alpha_2}{\alpha_1} \right)^{-C_p}, \tag{6.12}$$

where C_p has values of 0.583, 0.611, and 0.463 with R^2 values of 0.982, 0.986, and 0.985 for p = 100, 110, and 111, respectively, and $\gamma_p(0, \alpha_0, \alpha_0)$ can be calculated with Eq. (6.9). Figure 6.8 demonstrates that Eq. (6.12) captures the trend of the simulation results; however, the simulation data deviates significantly from the best fit line when α_2/α_1 is far from unity.

These results suggest that Eq. (6.12) is too simple to fully describe the relationship for the solid-liquid interfacial energy when $\alpha_1 \neq \alpha_2$. Nonetheless, Eq. (6.12) provides an approximation for $\gamma_p(0, \alpha_1, \alpha_2)$ when $\alpha_1 \neq \alpha_2$ and reduces to Eq. (6.9) when $\alpha_1 = \alpha_2$. As seen in Fig. 6.8, $\gamma_p(0, \alpha_1, \alpha_2) < \gamma_p(0, \alpha_0, \alpha_0)$ when $\alpha_2 > \alpha_1$, and $\gamma_p(0, \alpha_1, \alpha_2) > \gamma_p(0, \alpha_0, \alpha_0)$ when $\alpha_2 < \alpha_1$, for all orientations. However, the degree by which $\gamma_p(0, \alpha_1, \alpha_2)$ changes with α_2/α_1 depends on the interfacial orientation. As a result, the relative energies of interfaces will change when the value of α_2/α_1 is far from unity.

6.3 Chapter Summary

We have developed a PFC model with a stable *dc* structure, which is based on the XPFC approach. In this model, we approximate a two-body DCF with a combination of two Gaussian functions in Fourier space, where the first and second peak positions are centered at $k_1 = 2\pi\sqrt{8}/a$ and $k_2 = 2\pi\sqrt{3}/a$, respectively, and a is the lattice constant of a cubic structure. A temperature-density phase diagram, which contains *dc*-liquid, *bcc*-liquid, and *dc*-*bcc* phase coexistence regions, was calculated for the model.

We found that the interfacial energies, $\gamma_p(\sigma, \alpha_1, \alpha_2)$, for the (100), (110), and (111) interfaces depend on α_0 according to an inverse power law when the temperature parameter, σ, is set to zero and the first and second peaks of the DCF are equal, $\alpha_1 = \alpha_2 = \alpha_0$. In the case where $\alpha_1 \neq \alpha_2$, we found that the trend of $\gamma_p(\sigma, \alpha_1, \alpha_2)$ as a function of α_2/α_1 is approximated by an inverse power law. The dependence of $\gamma_p(\sigma, \alpha_1, \alpha_2)$ on σ is well described by a Gaussian function when $\alpha_1 = \alpha_2 = \alpha_0$, via Eq. (6.11). For all peak widths and interface orientations, the fitting parameter for the Gaussian function, R_p, was found to be within 8% of one another. Therefore, it would be worthwhile to examine whether the dependence of $\gamma_p(\sigma, \alpha_1, \alpha_2)$ on σ for other structures will also exhibit a similar value of R_p.

CHAPTER VII

Conclusion and Future Work

7.1 Summary

In this dissertation, we have investigated the bulk equilibrium properties of crystalline structures that are stable within the phase-field crystal (PFC) model. We developed thermodynamic relationships that were used to derive procedures for calculating equilibrium material properties from the PFC model. These relationships were also applied to gain a rigorous understanding of PFC simulation results.

The first set of relationships linked the PFC free energy to thermodynamic state variables and was derived based on the thermodynamic formalism for crystalline systems introduced by Larché and Cahn [56]. These relationships were employed to examine the thermodynamic processes associated with varying the PFC input parameters. Additionally, equilibrium conditions between bulk crystalline solid and liquid phases were imposed on these relationships to obtain a procedure for determining solid-liquid phase coexistence. The resulting procedure was found to be in agreement with the common-tangent construction commonly used in the PFC community, justifying the approach. Using this procedure we found that the EOF-PFC model parameterization [54] does not predict stable *bcc* structures with positive vacancy densities.

The second set of relationships linked PFC free energy change due to deformation to elastic constants. These relationships were built on the recent work of Pisutha-Arnond et al. [53], which is also based on the thermodynamic formalism of Larché and Cahn [56]. We demonstrated that the calculation of elastic constants requires the knowledge of the pressure, P^0, and bulk modulus, $\mathcal{K}^0$, of the liquid reference state. Since the two-body DCF is measured at the liquid reference state, any parameterization that adjusts the shape of the DCF will also effect the resulting elastic constant values. A computationally accurate and efficient Fourier-space method for applying deformation was developed to implement these relationships. Using the Fourier-space method, the elastic constants and solid bulk modulus of *bcc* structures from the EOF-PFC model were determined. Large discrepancies were found between the elastic constants and solid bulk modulus calculated from the EOF-PFC model and those from the MD simulation upon which the EOF-PFC model was parameterized.

Finally, we investigated a diamond-cubic (*dc*) structure based on the structural PFC (XPFC) model and developed relationships between the solid-liquid interfacial energies and the shape of the two-body direct correlation function (DCF). The dependence of interfacial energy on a temperature parameter, which controls the heights of the peaks in the two-body DCF, was found to be described by a Gaussian function. Furthermore, the dependence of interfacial energy on peak widths of the two-body DCF, which controls the excess energy associated with interfaces, defects, and strain, was found to be described by an inverse power law. These relationships can be employed to parameterize the PFC model for the *dc* structure to match solid-liquid interfacial energies to those measured experimentally or calculated from atomistic simulations.

7.2 Impact

A parameterization of the PFC model to produce equilibrium properties that match those obtained from experiments and atomistic calculations is required before the PFC model can be applied to predict non-equlibrium materials phenomena. The ability to directly compare PFC simulation results with experimental measurements and calculations from other theoretical approaches, such as MD and ab-initio density functional theory [73], eliminates the ambiguities that arise when parameterizing the PFC model [53, 54, 62]. Furthermore, the links established in this dissertation between thermodynamics and the PFC model provide the foundation for developing additional thermodynamic relationships to investigate solid-solid and solid-liquid interfaces [100] and creep in crystalline solids [101] with the PFC model.

7.3 Future Work

Although the procedures for calculating several equilibrium properties have been developed and the connections between PFC input parameters and thermodynamic state variables have been established, whether the PFC model can be parameterized to produce equilibrium properties that match those of physical materials remain unanswered. However, the findings of this dissertation point to two areas of immediate future work that may provide solutions or an additional understanding of the model.

First, in order to resolve the issue of stabilizing structures with negative vacancy density, the PFC model must be parameterized such that the primary peak position of the two-body DCF, k_m, is a function of $\bar{n}$ when the change of $\bar{n}$ is due to the addition or removal of an atom while θ^c, $\mathcal{V}^c$, and N_L^c are held constant. This corresponds to changing $\bar{n}$ while holding θ^c and $\mathcal{V}_C^c$ constant in the PFC model. However, it should be noted that a change in k_m reflects a change in the liquid reference state. Therefore, a parameterization that requires k_m to be a function of $\bar{n}$ necessitates P^0 and the liquid reference density, ρ_0, to change with $\bar{n}$. Since $\bar{n}$ depends on ρ_0, a relationship for k_m as a function $\bar{n}$ can only be obtained from the dependence of k_m on ρ_0, which can be determined from atomistic simulations. We point out that the pressure of the system changes as ρ_0 is varied. Therefore, atomistic simulations for different pressure states will be required to determine the dependence of k_m on ρ_0

Second, although several thermodynamic processes associated with changing PFC input parameters were elucidated for bulk phases in this work, a thermodynamic framework for interfaces in the PFC model remains to be developed. An extension of this work that considers interfaces is needed in order to gain a rigorous understanding of results obtained from PFC simulations that contain interfaces and grain boundaries. Furthermore, since we did not consider the equilibrium conditions between different crystal phases, the use of the common-tangent construction to determine solid-solid phase coexistence [24, 58, 66] remains to be verified. Therefore, the extension of this work to systems containing interfaces and different crystal phases are topics of future investigations.

APPENDICES

APPENDIX A

Gibbs-Duhem Relationship for Bulk Crystalline Solid

We derive the Gibbs-Duhem relation for a bulk crystalline solid following Voorhees and Johnson [57]. The internal energy of a one-component crystal is a function of S^c, $\mathcal{V}^c$, N_A^c, and N_L^c,

$$E^c = E^c(S^c, \mathcal{V}^c, N_A^c, N_L^c). \tag{A.1}$$

The differential form of E^c is

$$dE^c = \theta^c dS^c - P^c d\mathcal{V}^c + \mu_A^c dN_A^c + \mu_L^c dN_L^c, \tag{A.2}$$

where

$$\theta^c \equiv -\frac{\partial E^c}{\partial S^c}\bigg|_{\mathcal{V}^c, N_A^c, N_L^c}, \quad P^c \equiv -\frac{\partial E^c}{\partial \mathcal{V}^c}\bigg|_{S^c, N_A^c, N_L^c}, \quad \mu_A^c \equiv \frac{\partial E^c}{\partial N_A^c}\bigg|_{S^c, \mathcal{V}^c, N_L^c}, \quad \mu_L^c \equiv \frac{\partial E^c}{\partial N_L^c}\bigg|_{S^c, \mathcal{V}^c, N_A^c}. \tag{A.3}$$

Since Eq. (A.1) is a homogenous function of degree one, Eq. (A.2) yields

$$E^c(S^c, \mathcal{V}^c, N_A^c, N_L^c) = S^c\theta^c - P^c\mathcal{V}^c + \mu_A^c N_A^c + \mu_L^c N_L^c. \tag{A.4}$$

Differentiating Eq. (A.4) and subtracting from Eq. (A.2) gives us the Gibbs-Duhem relation for a bulk crystalline solid,

$$0 = S^c d\theta^c - \mathcal{V}^c dP^c + N_A^c d\mu_A^c + N_L^c d\mu_L^c. \tag{A.5}$$

APPENDIX B

Description of Deformation in Fourier Space

The the deformed coordinates, $\mathbf{r}$, can be calculated from an affine transformation of the undeformed coordinates, $\mathbf{R}$, by

$$\mathbf{r} = \boldsymbol{\alpha}_t \cdot \mathbf{R} \tag{B.1}$$

and the inverse transformation is

$$\mathbf{R} = \boldsymbol{\alpha}_t^{-1} \cdot \mathbf{r}. \tag{B.2}$$

Using Eq. (B.1), the order parameter of the undeformed state can be written as

$$\phi(\mathbf{R}) = \phi(\boldsymbol{\alpha}_t^{-1} \cdot \mathbf{r}). \tag{B.3}$$

To understand how the affine transformation behaves for coordinates in Fourier space, consider the Fourier transform of $\phi(\boldsymbol{\alpha}_t^{-1} \cdot \mathbf{r})$,

$$\begin{aligned}
\mathscr{F}\left[\phi(\boldsymbol{\alpha}^{-1} \cdot \mathbf{r})\right] &= \int \phi(\boldsymbol{\alpha}_t^{-1} \cdot \mathbf{r}) e^{-i\mathbf{k}' \cdot \mathbf{r}} d\mathbf{r} \\
&= J_t \int \phi(\mathbf{R}) e^{-i\mathbf{k}' \cdot (\boldsymbol{\alpha}_t \cdot \mathbf{R})} d\mathbf{R} \\
&= J_t \int \phi(\mathbf{R}) e^{-i\left(\boldsymbol{\alpha}_t^T \cdot \mathbf{k}'\right) \cdot \mathbf{R}} d\mathbf{R} \\
&= J_t \hat{\phi}(\boldsymbol{\alpha}_t^T \cdot \mathbf{k}'), \qquad \text{(B.4)}
\end{aligned}$$

where we have used the relationship $d\mathbf{R} = d\mathbf{r}/J_t$ and $\mathbf{k}'$ denotes the deformed coordinates in reciprocal space. Equation (B.4) is a restatement of the similarity theorem of the Fourier transform [85] in higher dimensions, where the mapping from deformed coordinates to undeformed coordinates in reciprocal space is given by $\boldsymbol{\alpha}_t^T$ such that

$$\mathbf{k} = \boldsymbol{\alpha}_t^T \cdot \mathbf{k}'. \qquad \text{(B.5)}$$

Inversely, the mapping from undeformed coordinates to deformed coordinates in reciprocal space is given by $\boldsymbol{\alpha}_t^{-T}$, i.e.,

$$\mathbf{k}' = \boldsymbol{\alpha}_t^{-T} \cdot \mathbf{k}. \qquad \text{(B.6)}$$

Note that the volume change due to the mapping of coordinates is accounted for by J_t.

REFERENCES

REFERENCES

[1] W D Callister Jr. *Materials Science and Engineering An Introduction.* John Wiley and Sons, Inc, 7th edition, 2007.

[2] E P Degarmo, J T Black, and R A Kosher. *Materials and Processes in Manufacturing.* Wiley, 9th edition, 2003.

[3] D L Douglass and T W Barbee. Spinodal decomposition in al/zn alloys. *Journal of Materials Science*, 4(2):121–129, February 1969.

[4] M A Meyers and K K Chawla. *Mechanical Behavior of Materials.* Cambridge University Press, 2009.

[5] C B Murray, C R Kagan, and M G Bawendi. Self-organization of cdse nanocrystallites into 3-dimensional quantum-dot superlattices. *Science*, 270(5240):1335–1338, 1995.

[6] L Pavesi, L D Negro, C Mazzoleni, and G Franzo. Optical gain in silicon nanocrystals. *Nature*, 408(23):440, 2000.

[7] M Asta, C Beckermann, A Karma, W Kurz, R Napolitano, M Plapp, G Purdy, M Rappaz, and R Trivedi. Solidification microstructures and solid-state parallels: Recent developments, future directions. *Acta Materialia*, 57(4):941–971, 2009.

[8] S L Wang, R F Sekerka, A A Wheeler, B T Murray, S R Coriell, R J Braun, and G B McFadden. Thermodynamically-Consistent Phase-Field Models for Solidification. *Physica D*, 69(1-2):189–200, 1993.

[9] A Karma and W-J Rappel. Phase-field method for computationally efficient modeling of solidification with arbitrary interface kinetics. *Physical Review E*, 53(4):R3017–R3020, April 1996.

[10] A A Wheeler, G B McFadden, and W J Boettinger. Phase-field model for solidification of a eutectic alloy. *Proceedings of the Royal Society of London Series: Mathematical, Physical and Engineering Sciences*, 452(1946):495–525, 1996.

[11] A Karma. Phase-field formulation for quantitative modeling of alloy solidification. *Physical Review Letters*, 87(11), 2001.

[12] L Q Chen and A G Khachaturyan. Computer-Simulation of Structural Transformations During Precipitation of an Ordered Intermetallic Phase. *Acta Metallurgica Et Materialia*, 39(11):2533–2551, November 1991.

[13] L Q Chen and Y Z Wang. The continuum field approach to modeling microstructural evolution. *JOM*, 48(12):13–18, 1996.

[14] L Q Chen, C Wolverton, V Vaithyanathan, and Z K Liu. Modeling solid-state phase transformations and microstructure evolution. *Mrs Bulletin*, 26(3):197–202, March 2001.

[15] L Q Chen and W Yang. Computer simulation of the domain dynamics of a quenched system with a large number of nonconserved order parameters: The grain-growth kinetics. *Physical Review B*, 50(21):15752–15756, December 1994.

[16] V Tikare, E A Holm, D Fan, and L Q Chen. Comparison of phase-field and Potts models for coarsening processes. *Acta Materialia*, 47(1):363–371, 1998.

[17] C E Krill and L Q Chen. Computer simulation of 3-D grain growth using a phase-field model. *Acta Materialia*, 50(12):3057–3073, 2002.

[18] W J Boettinger, J A Warren, C Beckermann, and A Karma. Phase-field simulation of solidification 1. *Annual Review of Materials Research*, 32:163–94, 2002.

[19] H Emmerich. Advances of and by phase-field modelling in condensed-matter physics. *Advances in Physics*, 57(1):1–87, Jan 2008.

[20] M I Mendelev, S Han, D J Srolovitz, G J Ackland, D Y Sun, and M Asta. Development of new interatomic potentials appropriate for crystalline and liquid iron. *Philosophical Magazine*, 83(35):3977–3994, December 2003.

[21] M Parrinello. Crystal structure and pair potentials: A molecular-dynamics study. *Physical Review Letters*, 45(14):1196–1199, Jan 1980.

[22] D Frenkel and B Smit. *Understanding Molecular Simulations.* Elsevier, 2002.

[23] K R Elder, M Katakowski, M Haataja, and M Grant. Modeling elasticity in crystal growth. *Physical Review Letters*, 88(24):245701, Jan 2002.

[24] K R Elder and M Grant. Modeling elastic and plastic deformations in nonequilibrium processing using phase field crystals. *Physical Review E*, 70(5):051605, Jan 2004.

[25] J Berry, M Grant, and K R Elder. Diffusive atomistic dynamics of edge dislocations in two dimensions. *Physical Review E*, 73:031609, Jan 2006.

[26] T Hirouchi, T Takaki, and Y Tomita. Development of numerical scheme for phase field crystal deformation simulation. *Computational Materials Science*, 44(4):1192–1197, Jan 2009.

[27] T Hirouchi, T Takaki, and Y Tomita. Effects of temperature and grain size on phase-field-crystal deformation simulation. *International Journal of Mechanical Sciences*, 52:309–319, Jan 2010.

[28] J Berry, N Provatas, J Rottler, and C W Sinclair. Defect stability in phase-field crystal models: Stacking faults and partial dislocations. *Physical Review B*, 86(22), 2012.

[29] J Berry, N Provatas, J Rottler, and C W Sinclair. Phase field crystal modeling as a unified atomistic approach to defect dynamics. *Physical Review B*, 89(21), 2014.

[30] J Berry, K Elder, and M Grant. Simulation of an atomistic dynamic field theory for monatomic liquids: Freezing and glass formation. *Physical Review E*, 77:061506, 2008.

[31] L Gránásy, G Tegze, G I Tóth, and T Pusztai. Phase-field crystal modelling of crystal nucleation, heteroepitaxy and patterning. *Philosophical Magazine*, 91(1):123–149, 2011.

[32] G Tegze, L Gránásy, G Tóth, F Podmaniczky, A Jaatinen, T Ala-Nissila, and T Pusztai. Diffusion-controlled anisotropic growth of stable and metastable crystal polymorphs in the phase-field crystal model. *Physical Review Letters*, 103:035702, 2009.

[33] G I Tóth, G Tegze, T Pusztai, G Tóth, and L Gránásy. Polymorphism, crystal nucleation and growth in the phase-field crystal model in 2d and 3d. *Journal of Physics: Condensed Matter*, 22(36):364101, Jan 2010.

[34] G Tegze, L Gránásy, G I Tóth, J F Douglas, and T Pusztai. Tuning the structure of non-equilibrium soft materials by varying the thermodynamic driving force for crystal ordering. *Soft Matter*, 7(5):1789, 2011.

[35] G Tegze, G Tóth, and L Gránásy. Faceting and branching in 2d crystal growth. *Physical Review Letters*, 106(19):195502, May 2011.

[36] C Achim, M Karttunen, K R Elder, E Granato, T Ala-Nissila, and S C Ying. Phase diagram and commensurate-incommensurate transitions in the phase field crystal model with an external pinning potential. *Physical Review E*, 74:021104, 2006.

[37] Z-F Huang and K R Elder. Mesoscopic and microscopic modeling of island formation in strained film epitaxy. *Physical Review Letters*, 101(15):158701, October 2008.

[38] C Achim, J A P Ramos, M Karttunen, K R Elder, E Granato, T Ala-Nissila, and S C Ying. Nonlinear driven response of a phase-field crystal in a periodic pinning potential. *Physical Review E*, 79:011606, 2009.

[39] K R Elder and Z-F Huang. A phase field crystal study of epitaxial island formation on nanomembranes. *Journal Of Physics: Condensed Matter*, 22:364103, 2010.

[40] J A P Ramos, E Granato, S C Ying, C V Achim, K R Elder, and T Ala-Nissila. Dynamical transitions and sliding friction of the phase-field-crystal model with pinning. *Physical Review E*, 81(1):011121, January 2010.

[41] S Muralidharan and M Haataja. Phase-field crystal modeling of compositional domain formation in ultrathin films. *Physical Review Letters*, 105(12):126101, 2010.

[42] Y-M Yu, R Backofen, and A Voigt. Morphological instability of heteroepitaxial growth on vicinal substrates: A phase-field crystal study. *Journal Of Crystal Growth*, 318(1):18–22, 2011.

[43] E Granato, J A P Ramos, C V Achim, J Lehikoinen, S C Ying, T Ala-Nissila, and K R Elder. Glassy phases and driven response of the phase-field-crystal model with random pinning. *Physical Review E*, 84(3):031102, 2011.

[44] J Berry and M Grant. Modeling multiple time scales during glass formation with phase-field crystals. *Physical Review Letters*, 106(17):175702, 2011.

[45] K R Elder, N Provatas, J Berry, P Stefanovic, and M Grant. Phase-field crystal modeling and classical density functional theory of freezing. *Physical Review B*, 75(6):064107, Jan 2007.

[46] T V Ramakrishnan and M Yussouff. First-principles order-parameter theory of freezing. *Physical Review B*, 19(5):2775–2794, Mar 1979.

[47] A D J Haymet and D W Oxtoby. A molecular theory for the solid–liquid interface. *The Journal of Chemical Physics*, 74(4):2559, 1981.

[48] J-P Hansen and I R McDonald. *Theory of Simple Liquid.* Academic Press, 2006.

[49] R Evans and D Henderson. *Fundamentals of Inhomogeneous Fluids.* New York: Dekker, 1992.

[50] N Ofori-Opoku, V Fallah, M Greenwood, S Esmaeili, and N Provatas. Multicomponent phase-field crystal model for structural transformations in metal alloys. *Physical Review B*, 87(13):134105, April 2013.

[51] R Prieler, J Hubert, D Li, B Verleye, R Haberkern, and H Emmerich. An anisotropic phase-field crystal model for heterogeneous nucleation of ellipsoidal colloids. *Journal Of Physics: Condensed Matter*, 21(46):464110, 2009.

[52] H Löwen. A phase-field-crystal model for liquid crystals. *Journal Of Physics: Condensed Matter*, 22(36):364105, 2010.

[53] N Pisutha-Arnond, V W L Chan, K R Elder, and K Thornton. Calculations of isothermal elastic constants in the phase-field crystal model. *Physical Review B*, 87(014103), 2013.

[54] A Jaatinen, C V Achim, K R Elder, and T Ala-Nissila. Thermodynamics of bcc metals in phase-field-crystal models. *Physical Review E*, 80:031602, Jan 2009.

[55] M Greenwood, N Provatas, and J Rottler. Free energy functionals for efficient phase field crystal modeling of structural phase transformations. *Physical Review Letters*, 105:045702, 2010.

[56] F Larche and J W Cahn. Linear Theory of Thermochemical Equilibrium of Solids Under Stress. *Acta Metallurgica*, 21(8):1051–1063, 1973.

[57] P W Voorhees and W C Johnson. The Thermodynamics of Elastically Stressed Crystals. *Solid State Physics*, 59:1–201, April 2004.

[58] M Greenwood, J Rottler, and N Provatas. Phase-field-crystal methodology for modeling of structural transformations. *Physical Review E*, 83:031601, 2011.

[59] P Stefanovic, M Haataja, and N Provatas. Phase-field crystals with elastic interactions. *Physical Review Letters*, 96(22):225504, Jan 2006.

[60] P Stefanovic, M Haataja, and N Provatas. Phase field crystal study of deformation and plasticity in nanocrystalline materials. *Physical Review E*, 80(4):046107, Jan 2009.

[61] D C Wallace. Thermoelasticity of stressed materials and comparison of various elastic constants. *Phys. Rev.*, 162:776, 1967.

[62] K-A Wu, A Adland, and A Karma. Phase-field-crystal model for fcc ordering. *Physical Review E*, 81(6):061601, 2010.

[63] J Swift and P C Hohenherg. Hydrodynamic fluctuations at convective instability. *Physical Review A*, 15(1):319–328, Jan 1977.

[64] J-P Hansen, D Levesque, and J Zinn-Justin, editors. *Les Houches Session LI: Liquids, Freezing, and Glass Transition.* Elsevier Science Publishing Company, Inc., 1989.

[65] N Provatas and K R Elder. *Phase-Field Methods in Materials Science and Engineering.* Wiley-VCH, 2010.

[66] A Jaatinen and K R Elder. Extended phase diagram of the three-dimensional phase field crystal model. *Journal Of Physics: Condensed Matter*, 22:205402, 2010.

[67] K-A Wu and P W Voorhees. Stress-induced morphological instabilities at the nanoscale examined using the phase field crystal approach. *Physical Review B*, 80(12):125408, September 2009.

[68] H Emmerich, H Löwen, R Wittkowski, T Gruhn, G I Toth, G Tegze, and L Gránásy. Phase-field-crystal models for condensed matter dynamics on atomic length and diffusive time scales: an overview. *Advances in Physics*, 61(6):665–743, December 2012.

[69] N Pisutha-Arnond, V W L Chan, M Iyer, V Gavini, and K Thornton. Classical density functional theory and the phase-field crystal method using a rational function to describe the two-body direct correlation function. *Physical Review E*, 87(1):013313, January 2013.

[70] A J Archer and R Evans. Dynamical density functional theory and its application to spinodal decomposition. *The Journal of Chemical Physics*, 121(9):4246–4254, Jan 2004.

[71] U M B Marconi and P Tarazona. Dynamic density functional theory of fluids. *Journal of Physics: Condensed Matter*, 12(8A):A413–A418, Jan 2000.

[72] U M B Marconi and P Tarazona. Dynamic density functional theory of fluids. *The Journal of Chemical Physics*, 110(16):8032–8044, Jan 1999.

[73] D S Sholl and J A Steckel. *Density Functional Theory: A Practical Introduction.* Wiley, 2009.

[74] R Evans. Nature of the liquid-vapor interface and other topics in the statistical-mechanics of nonuniform, classical fluids. *Advances in Physics*, 28(2):143–200, Jan 1979.

[75] Y Singh. Density-functional theory of freezing and properties of the ordered phase. *Physics Reports*, 207(6):351–444, Jul 1991.

[76] Z-F Huang, K R Elder, and N Provatas. Phase-field-crystal dynamics for binary systems: Derivation from dynamical density functional theory, amplitude equation formalism, and applications to alloy heterostructures. *Physical Review E*, 82(2, Part 1):021605, 2010.

[77] J Berry, K R Elder, and M Grant. Melting at dislocations and grain boundaries: A phase field crystal study. *Physical Review B*, 77:224114, Jan 2008.

[78] K-A Wu and A Karma. Phase-field crystal modeling of equilibrium bcc-liquid interfaces. *Physical Review B*, 76(18):184107, 2007.

[79] M Greenwood, C Sinclair, and M Militzer. Phase field crystal model of solute drag. *Acta Materialia*, 60(16):5752–5761, September 2012.

[80] V Fallah, J Stolle, N Ofori-Opoku, S Esmaeili, and N Provatas. Phase-field crystal modeling of early stage clustering and precipitation in metal alloys. *Physical Review B*, 86(13):134112, October 2012.

[81] V Fallah, A Korinek, N Ofori-Opoku, N Provatas, and S Esmaeili. Atomistic investigation of clustering phenomenon in the Al-Cu system: Three-dimensional phase-field crystal simulation and HRTEM/HRSTEM characterization. *Acta Materialia*, 61(17):6372–6386, October 2013.

[82] S van Teeffelen, R Backofen, A Voigt, and H Löwen. Derivation of the phase-field-crystal model for colloidal solidification. *Physical Review E*, 79(5):051404, 2009.

[83] A J Archer and M Rauscher. Dynamical density functional theory for interacting brownian particles: stochastic or deterministic? *Journal of Physics A: Mathematical and General*, 37(40):9325–9333, September 2004.

[84] D C Wallace. *Thermodynamics of Crystals.* Dover, 1998.

[85] R N Bracewell. *The Fourier Transform and its Applications.* McGraw-Hill, 3 edition, 2000.

[86] R N Bracewell, K Y Chang, A K Jha, and Y H Wang. Affine Theorem for 2-Dimensional Fourier-Transform. *Electronics Letters*, 29(3):304–304, 1993.

[87] G Shechter. *Respiratory Motion of the Heart: Implications for Magnetic Resonance Coronary Angiography.* PhD thesis, Johns Hopkins University, November 2004.

[88] T M Lehmann, C Gonner, and K Spitzer. Survey: Interpolation methods in medical image processing. *Medical Imaging, IEEE Transactions on*, 18(11):1049–1075, November 1999.

[89] L N Trefethen. *Spectral Methods in MATLAB.* Society for Industrial and Applied Mathematics, 2000.

[90] C B Barber, D P Dobkin, and H Huhdanpaa. The quickhull algorithm for convex hulls. *ACM Transactions on Mathematical Software (TOMS)*, 22(4):469–483, December 1996.

[91] M De Graef and M E McHenry. *Structural of Materials: An Introduction to Crystallography, Diffraction, and Symmetry.* Cambridge University Press, New York, 2007.

[92] M Lavrskyi, H Zapolsky, and A G Khachaturyan. Fraton Theory and Modelling of Self-Assembling of Complex Structures. *arXiv.org*, November 2014.

[93] J Towns, T Cockerill, M Dahan, I Foster, K Gaither, A Grimshaw, V Hazlewood, S Lathrop, D Lifka, G D Peterson, R Roskies, J R Scott, and N Wilkens-Diehr. XSEDE: Accelerating Scientific Discovery. *Computing in Science and Engineering*, 16(5):62–74, 2014.

[94] P A Apte and X C Zeng. Anisotropy of crystal-melt interfacial free energy of silicon by simulation. *Applied Physics Letters*, 92(22), 2008.

[95] D Turnbull. Formation of Crystal Nuclei in Liquid Metals. *Journal of Applied Physics*, 21(10):1022–1028, 1950.

[96] D Turnbull. Kinetics of Solidification of Supercooled Liquid Mercury Droplets. *Journal of Chemical Physics*, 20(3):411–424, March 1952.

[97] B B Laird. The solid-liquid interfacial free energy of close-packed metals: Hard-spheres and the Turnbull coefficient. *Journal of Chemical Physics*, 115(7):2887–2888, 2001.

[98] R L Davidchack and B B Laird. Direct calculation of the crystal–melt interfacial free energies for continuous potentials: Application to the Lennard-Jones system. *Journal of Chemical Physics*, 118(16):7651–7657, April 2003.

[99] B B Laird, R L Davidchack, Y Yang, and M Asta. Determination of the solid-liquid interfacial free energy along a coexistence line by Gibbs-Cahn integration. *Journal of Chemical Physics*, 131(11), 2009.

[100] J W Cahn. *in Interface Segregation.* American Society for Metals, 1979.

[101] Y Mishin, J A Warren, R F Sekerka, and W J Boettinger. Irreversible thermodynamics of creep in crystalline solids. *Physical Review B*, 88(18), 2013.